Fluid Metering Using Active Materials

Sangiah, Dhinesh

Award date:
2011

Awarding institution:
University of Bath

FLUID METERING USING ACTIVE MATERIALS

Submitted by

Dhinesh Kumar Sangiah

A thesis submitted in fulfilment of the degree of

Doctor of Philosophy

at the Department of Mechanical Engineering,

University of Bath,

September 2011.

_____

Dhinesh Sangiah

Abstract

Servovalves are compact, accurate, fast flow modulating valves widely used in aerospace, defence, industrial and marine applications. However, cost reduction pressures exist due to tight tolerances required, particularly in the first stage of the valve. In this research novel servovalve concepts are investigated. In particular, a new first stage actuator assembly is developed to move a servovalve spool using the jet principle.

The conventional torque motor assembly in the first stage was replaced by a multilayered bimorph actuator. A feedback wire was used to facilitate proportional flow control via mechanical feedback. The bimorph was directly coupled to the feedback wire for submerged operation. A steady state analytical model of the bimorph-feedback wire assembly was developed to derive the stiffness constants influencing the deflector and the valve spool. The derived stiffness constants were compared to FEA predictions. The flow forces acting on the deflector were determined using CFD analysis. The flow force was found to be proportional to the pressure drop across the deflector and the deflector displacement.

A high order nonlinear model of the valve was developed and used to simulate valve dynamic characteristics. The high order model was linearised and reduced to a first order lag to identify the system parameters that determined the first break frequency and the steady state gain of the valve. Two 'Mark-1' prototypes were built and tested. The measured frequency responses of the prototypes were in good agreement with the simulation results. At 140bar supply pressure and maximum applied voltage amplitude the -3dB bandwidth of the valve was measured at approximately 41Hz. The frequency response of the valve spool was reasonably consistent for varying applied voltage amplitudes at a fixed supply pressure. The hysteresis of the second stage spool was approximately ±4%. The stroke of the second stage spool was approximately 0.42mm.

The bandwidth and steady state gain of the valve were expressed in terms of ratios between the forward and feedback path variables of the valve system. Performance

plots were developed using these variable ratios. A ‘Mark-2’ prototype valve was developed and tested, intended to possess a higher bandwidth. The -3dB bandwidth of the ‘Mark-2’ valve spool at 140bar supply pressure and maximum applied voltage amplitude was measured at approximately 60Hz. At this voltage amplitude the spool stroke was approximately 0.24mm and the valve hysteresis was approximately ±2%. Bandwidth and stroke were consistent with the predictions.

Acknowledgements

I owe a great deal of gratitude to my principal supervisor Prof. Andrew Plummer, industrial supervisor Dr. Paul Guerrier and co-supervisor Prof. Chris Bowen for believing in my potential and giving me this opportunity. Andrew's guidance and advice throughout the project has been invaluable and inspirational. Paul and Chris have shown determined support and guidance throughout the project. The environment created by my supervisors made this whole journey an enjoyable experience and has helped me fulfil my ambition. I am thankful to Great Western Research and Moog for funding this study.

I am very thankful to Moog Controls Ltd. for their unreserved commitment towards the project and for their invaluable support and guidance. Steve Burks, Ian Brooks, Gary Powers, Murray Yeomens, Steve Johnson and Andrew Cogger have all contributed towards the project. The unprecedented support provided by Moog has most certainly contributed to the timely completion of this study.

I would like to express gratefulness to Alan Jefferis for his friendly and relentless technical support throughout the project. I am also thankful to Vijay Rajput and Stephen Coombes for their instrumentation support and advice. I am thankful to Gillian Elsworth for all the administrative support. I am thankful to all the members of CPTMC for making my time very enjoyable.

I feel an exceptional sense of gratitude towards all my friends for their unreserved support and friendship.

I am deeply obliged to my father and mother for their unconditional love and support in my life. They have taught me the righteous path and the morals that truly matter in life. I owe them a great deal for providing me a truly great platform. I am very grateful to my brother and sister for their exceptional support and unconditional love.

Contents

Appendix A – Published Paper

List of Figures

List of Tables

Abbreviations

CFD	Computational fluid dynamics
EAP	Electroactive polymer
EMA	Electromagnetic actuator
ERF	Electrorheological fluid
FEA	Finite element analysis
ISA	Induced strain actuator
LVDT	Linear variable differential transformer
MRF	Magnetorheological fluid
PHSV	Piezohydraulic servovalve
PI	Physik Instrumente
PVP	Piezoelectric valve prototype
PZT	Lead Zirconate Titanate
SMA	Shape memory alloy

Nomenclature

A_a	Hydraulic actuator annulus area
A_s	Main stage spool cross section area
b	Bimorph actuator width
B_w	Bandwidth
C_b	Damping coefficient of the bimorph
C_d	Damping coefficient at the deflector
C_{df}	Discharge coefficient at control ports
C_s	Damping coefficient at the main stage spool
C_{sf}	Spool flow port discharge coefficient
d	Pilot stage amplifier thickness
d_{31}	Piezoelectric charge constant
d_v	Ratio of displacement to applied voltage
e	Field strength of the bimorph actuator
E	Young's modulus
E_b	Young's modulus of the bimorph actuator
E_f	Young's modulus of the feedback wire
F	Operating frequency
F_d	Force at the deflector
K_{ff}	Flow force stiffness at the deflector

F_{fs}	Flow force at the spool
f_s	Filter cut-off frequency
F_s	Force at the spool
h	Thickness of a bimorph actuator segment
I	Second moment of area
I_b	Second moment of area of the bimorph actuator
I_f	Second moment of area of the feedback wire
J_w	Jet width
$k_1\ k_2\ k_3\ k_4\ k_5\ k_6$	Stiffness constants
K_b	Bimorph stiffness
k_r	Bimorph to feedback wire flexural stiffness ratio
K_{ss}	Steady stage gain
L_b	Length of the bimorph actuator
L_d	Length of the deflector guide
L_{dr}	Deflector guide to feedback wire length ratio
L_f	Length of the feedback wire
L_r	Bimorph to feedback wire length ratio
M	Bending moment
m_b	Effective mass of bimorph
m_d	Effective mass of the deflector

M_{Fd}	Moment due to force F_d
M_{Fs}	Moment due to force F_s
m_s	Main stage spool mass
M_u	Moment in the upper segment of the bimorph actuator
$\dot{n}$	Derivative of the hysteretic nonlinear term
$n_1\ n_2\ n_3\ n_4\ n_5\ n_6$	Stiffness constants
P_{pa}	Pressure in control port a
P_{pae}	Equilibrium pressure in control port a
P_{pb}	Pressure in control port b
P_{pbe}	Equilibrium pressure in control port b
P_r	Return pressure
P_s	Supply pressure
Q	Amplitude of flow through the valve
Q_{p1}	Flow in control port a
Q_{p1e}	Equilibrium flow in control port a
Q_{p2}	Flow out of control port a
Q_{p2e}	Equilibrium flow out of control port a
Q_{p3}	Flow into control port b
Q_{p4}	Flow out of control port b
Q_{pa}	Flow through control port a

Q_{pae}	Equilibrium flow through control port a
Q_{pb}	Flow through control port b
R	Radius of curvature
R_w	Effective reciever width
S_{fw}	Spool flow port width
S_w	Slot width
V	Supply voltage
$\dot{V}$	Derivative of applied voltage
V_{pa}	Control port a volume
V_{pb}	Control port 2b volume
W	Force on a beam
w_1	Q_{p1} flow gain
w_2	Q_{p2} flow gain
w_{br}	Ratio influencing bandwidth
x_0	Initial control port width for flow in
x_d	Deflector displacement
x_{rx}	Initial control port width for flow out
x_s	Spool displacement
$\dot{x_s}$	Spool velocity
Y	Hydraulic actuator displacement

α	Bouc-Wen model tuning parameter
β	Bouc-Wen model tuning parameter
β_f	Fluid bulk modulus
γ	Bouc-Wen model tuning parameter
δ	Bimorph tip deflection
θ	Bimorph slope
ρ	Fluid density
σ	Stress in a bimorph segment
τ	Time constant
τ_s	Filter time constant
φ	Flow angle at the spool
ΔP	Pressure drop across the spool flow ports

Chapter 1

Introduction

1.1 Servovalve background

Hydraulic control systems are widely used in applications where high force levels, fast response and high power to weight ratios are desired. Applications requiring these features include the positioning of aerodynamic control surfaces, precision control of machine tools, marine control equipment and mobile equipment control systems [1]. The primary power modulation elements utilized in high performance hydraulic servo systems are servovalves.

Servovalves are typically two stage devices with the first stage being a hydraulic amplifier and the second stage employing a sliding spool. The hydraulic amplifier generates the pressure drop to drive the second stage spool which in turn modulates valve flow. In electrohydraulic servovalves the hydraulic amplifier is coupled to an electromagnetic actuator. This enables an electrical input to modulate the valve. Servovalves can be used to provide pressure or flow control, with the most common application being a combined direction and flow control [1].

Typically the first stage employs a torque motor coupled to a hydraulic amplifier with mechanical feedback of the second stage spool position. The hydraulic amplifier is generally a nozzle-flapper, a jet pipe or a deflector jet. In a nozzle-flapper valve, the torque motor moves the flapper to differentially restrict flow escaping from the nozzles. The differential pressure in the nozzles is mapped across the second stage spool. This generates a force imbalance at the spool which causes it to move. The movement of the spool flexes an internal mechanical feedback wire which generates the restoring force to re-centre the flapper. Figure 1.1 shows a schematic of a conventional first stage nozzle-flapper hydraulic amplifier.

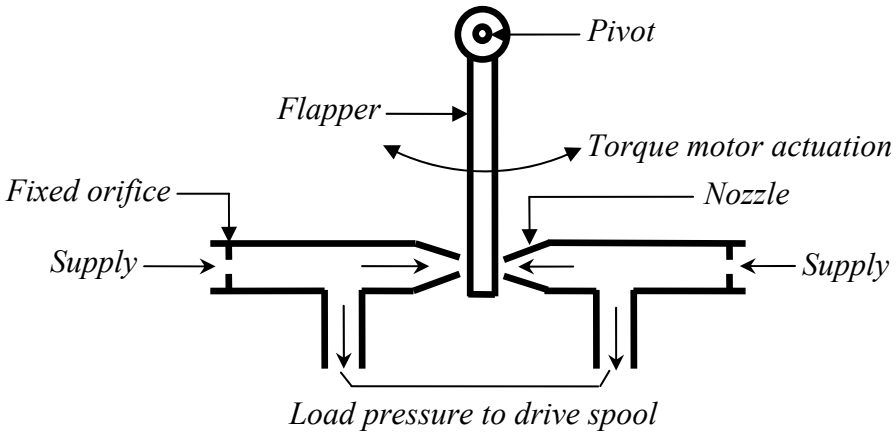

Figure 1.1: Schematic of a conventional first stage nozzle-flapper hydraulic amplifier

In a jet pipe valve the torque motor drives a nozzle (jet pipe) which directs a jet of fluid into two control ports, as shown in Figure 1.2. At the null position, the nozzle is centred and the fluid jet is evenly distributed between the control ports. This generates equal pressures on either end of the spool, which holds the spool in position. Any movement of the torque motor rotates the jet pipe, resulting in more flow into one control port than the other. The greater flow results in a higher pressure recovery in that control port which generates a force imbalance at the main stage spool causing it to move. As with the nozzle flapper, the feedback wire generates the restoring torque centralising the nozzle.

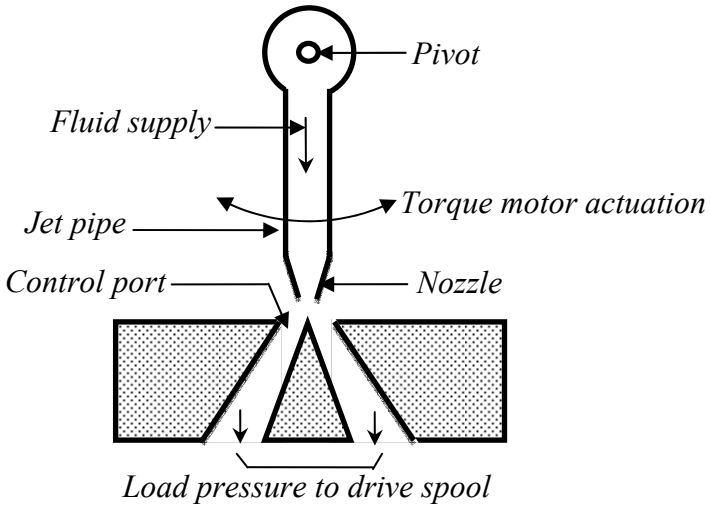

Figure 1.2: Schematic of a conventional first stage jet pipe hydraulic amplifier

As with a jet pipe, a deflector jet valve generates pressure on either end of the main stage spool by directing flow into two first stage control ports. However, it uses a deflector to guide the flows into the control ports instead of a moveable nozzle. The principle of the deflector jet valve will be discussed in detail in chapter 2.

In two stage servovalves the actuating force at the spool can be 10 times higher than the opposing flow forces [2]. Owing to this high force differential, the flow forces at the spool have a negligible influence on the valve dynamics. The dynamics are greatly influenced by the first stage flow. The first stage flow characteristics are dependent on the first stage actuator [3], [4], [5]. The torque motor has remained the predominant actuation mechanism for servovalves. The following section discusses the operating principle and the limitations of the torque motor.

1.2 The torque motor

1.2.1 Operating principle

The torque motor is a small, limited rotation electromagnetic actuator (EMA). Figure 1.3 shows a typical torque motor. The armature is essentially an electromagnet. A flow of current through the coils polarise the armature. The polarity of the armature is dependent on the direction of current flowing through the coils. The pole pieces are permanent magnets. The induced flux in the armature therefore generates a torque which makes the armature rotate.

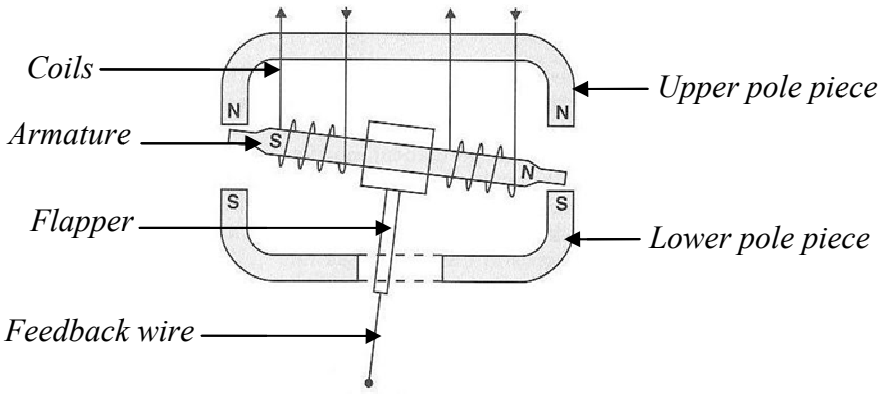

Figure 1.3: Torque motor schematic [1]

1.2.2 Limitations of the torque motor

Torque motors are generally categorised into wet or dry motors. For a wet motor set up the torque motor is immersed in the hydraulic fluid. This introduces reliability issues over time due to the attraction and accumulation of metallic particles suspended in the fluid. In dry motors, the torque motor is isolated from the hydraulic fluid. This removes the inherent reliability problems concerned with wet motors. However, the implementation of a dry torque motor set up introduces the design challenge of effecting a frictionless seal for the transmission.

In dry motors, the function of the frictionless seal is usually performed by a flexure tube. The flexure tube transmits the torque from the armature to the hydraulic amplifier with little resistance. In addition the flexure tube seals the torque motor assembly from the hydraulic fluid and acts as a pivot. The flexure tube needs to be

manufactured to an extremely fine tolerance in ordered to provide the desired mechanical characteristics. The inclusion of the flexure sleeve makes manufacture and assembly of the servovalve first stage expensive and time consuming.

Servovalves need to comply with electromagnetic compatibility standards to ensure they function in the intended environment without causing or experiencing performance degradation due to unintentional electromagnetic interference. The controller and the electromagnetic actuator at the first stage of a servovalve are the two primary systems that are influenced by these emissions.

The peak torque generated by typical first stage torque motor is about 0.5Nm [3]. An exploded view of a typical torque motor assembly is shown in Figure 1.4. The number of components required to produce this torque compromises the energy density of the torque motor. In addition, the parts count increases the cost and weight of the assembly. Set up costs are also incurred with the torque motor. For example, the air gap needs to be precise as it influences the dynamic characteristics of the valve [3], [6].

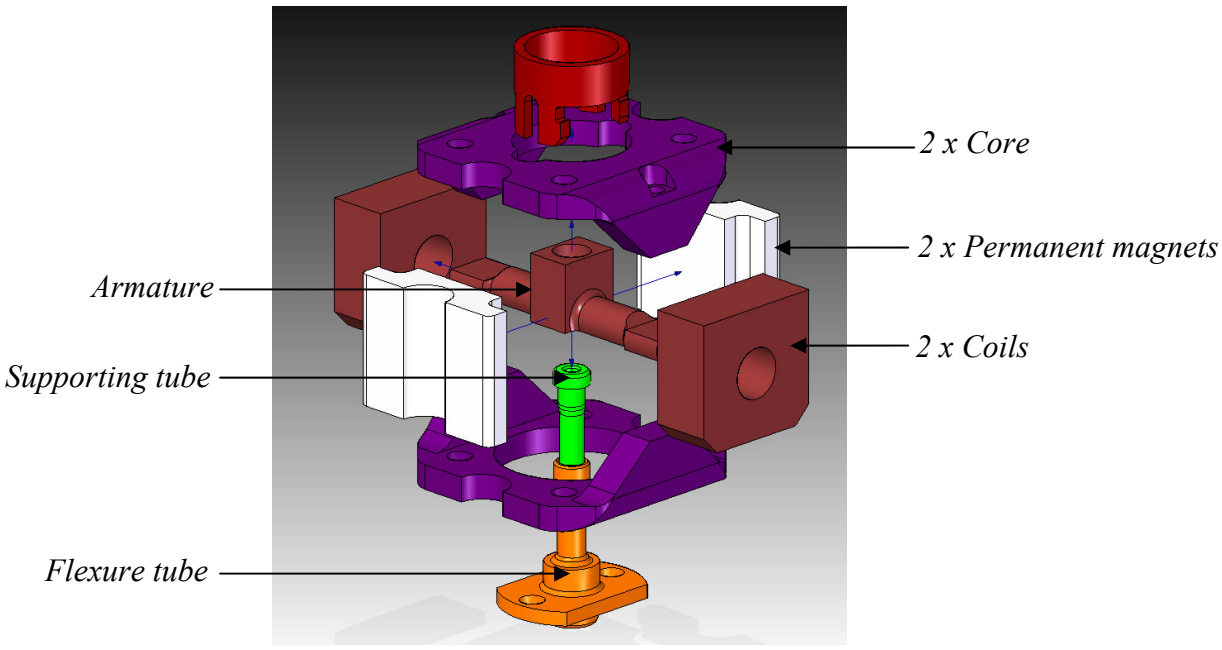

Figure 1.4 : Exploded view of the torque motor assembly

1.2.3 Alternative actuation

Over the years, active materials have been investigated for actuator applications as an alternative to electromagnetic actuators [7]. With recent advancements in this field, high performance actuators have been developed for various applications such as aerospace [8], [9], automotive [10] and biomedical [11]. The dynamic response of a two stage servovalve can be improved by improving the first stage actuator performance. Frequency responses of 1kHz [12], [5] have been reported, made possible by using active material actuators in the first stage of servovalves. The following section is an overview of active materials used in actuation applications.

1.3 Overview of active materials

Active materials are substances that possess the capability to respond to an external stimulus in a controlled manner. Actuators which use the strain of these materials to produce motion are known as induced strain actuators (ISAs) [13]. Materials commonly used for ISA applications are piezoelectric, electrostrictive, magnetostrictive, shape memory alloy (SMA) and electro active polymers (EAPs).

The superior performance of piezoelectric actuators relative to other ISAs make them the main alternative to EMAs[13], [14]. These materials are capable of material deformation in response to an applied electric potential (direct effect), or the development of charge in response to a force (converse effect). The response of the material is approximately linear to the demand. Traditionally, piezoelectric actuators are known for their high bandwidth (≈25kHz) [3], actuation force (>1kN), energy density [7] and limited stroke (≈0.1% strain) [15]. They are also associated with significant hysteresis effects when subjected to large electric fields. Piezoelectric actuators have been investigated and used in various applications [13],[14], [16].

Electrostrictive materials are similar in terms of response to piezoelectric materials. These materials are capable of higher strains relative to piezoelectric materials (≈0.2% [7]) at room temperatures. At these temperatures the hysteresis of electrostrictives is high and is greater than piezoelectrics [17]. At higher

temperatures the hysteresis is improved, however, the strain of the material is substantially compromised [17] [18]. The variation of strain and hysteresis with temperature limits the temperature stability of the material. In addition these materials have a quadratic relationship to the demand and are polarity independent.

Magnetostrictive materials are the magnetic analogy of piezoelectric materials. They generate a strain in response to an external magnetic field. The converse is known as piezomagnetic. These materials have better strain (>0.1% [13]) and hysteresis[19] characteristics compared to piezoelectric actuators. However, the requirement of a coil to generate the magnetostrictive effect compromises the power density and increases the complexity of these actuators [13]. They are also liable to produce electromagnetic emissions.

SMAs are active materials which are characterised by their unique super elastic behaviour which enables them to recover to their original shape after experiencing considerable deformation. This function of SMA is known as the shape memory effect. These materials undergo a solid state phase change from a martensite state (low temperature state) to an austenite state (high temperature state) or the converse in response to an external thermal or mechanical stimulus. Traditionally SMAs are known for their superior strain capability (4%-8%) [13]. However they exhibit very high hysteresis and have a limited bandwidth (≈1Hz) [20]. These two factors have limited their application for ISAs.

EAPs are active materials which exhibit a shape change in response to an electric stimulus. These actuators are classified into electric and ionic polymers. The shape change in electric EAPs is driven by electric field or Coulomb force. Large applied electric fields (≈200MV/m) induce electrostrictive strains of nearly 2% [21]. In ionic polymers the shape change is driven by the migration of ions in the polymer network between the positive and negative electrodes, in response to an electric stimulus. ISA made from EAPs can be fabricated to generate strains in comparison to human muscles (25% of active deformation) [13] at high response speeds. At present these materials are limited by low actuation force (low stiffness), mechanical energy density and robustness [22].

The dominance of piezoelectric materials for ISAs is replicated in servovalve applications. Piezoelectric actuators have been researched in various configurations as an alternative to the electromagnetic actuation in valves. Two types of piezoelectric actuators which have been used are 'stack' and 'bimorph' actuator. Stack actuators are based on the longitudinal piezoelectric effect consisting of several ceramic-metal electrode layers with alternating polarity. A conventional stack actuator is shown in Figure 1.5. These actuators are associated with high forces (>1000N) high drive voltages (150-1000V) and limited stroke (≈100µm).

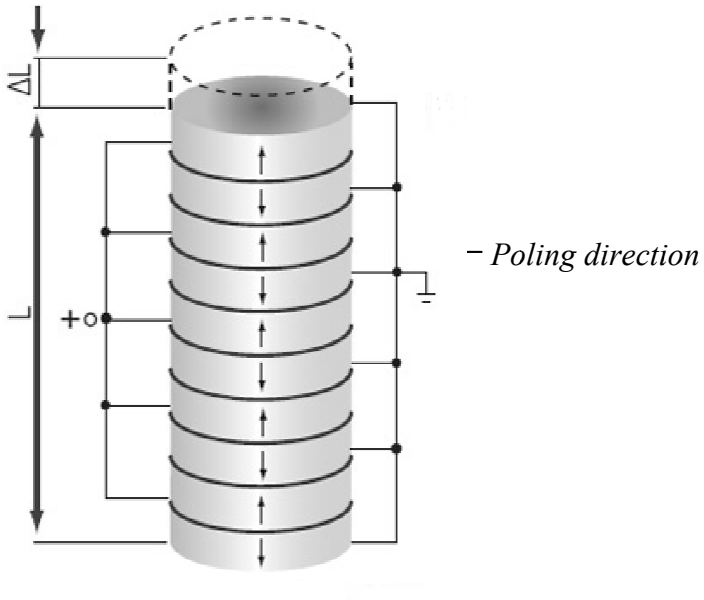

Figure 1.5: Conventional piezoelectric stack actuator [23]

Bimorph actuators are based on the transverse piezoelectric effect which generates an internal piezoelectric moment causing a bending deformation. The bending of a conventional bimorph actuator is similar to a bimetallic strip [24]. These actuators provide greater stroke (up to 1mm) at significantly lower operating voltages (≈100V). However their force capability is greatly compromised (≈2N). Figure 1.6 shows a conventional bimorph actuator poled for series operation. The following section is a review of previous piezohydraulic valve research.

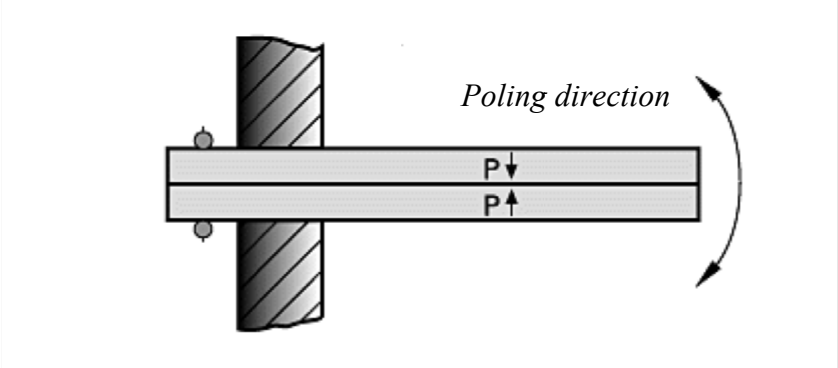

Figure 1.6: Conventional bimorph actuator poled for series operation [23]

1.4 Review of piezohydraulic valve research

Bang et al. [25] developed a two stage electrohydraulic nozzle-flapper servovalve using a high power piezoelectric stack actuator to drive the flapper. The maximum output force of the actuator was 1200N at an applied voltage of 250V. The stroke of the actuator was 42µm. The limited stroke was improved by using flexural stroke amplification. Thermal expansion and hysteresis effects had to be compensated due to the high operating voltages. In addition the actuators had to be preloaded to prevent them from being in tension. Electronic feedback of the main stage spool was used to achieve proportional flow through the valve. The frequency response of the valve was 300Hz (-90 degrees phase frequency) at 210bar supply pressure.

Karunanidhi et al. [3] used a commercially available stroke amplified stack actuator to replace the torque motor of a two stage nozzle-flapper servovalve. The actuator was connected directly to the flexure tube in the first stage as shown in Figure 1.7. The actuator assembly produced a maximum displacement of 135µm at 150V supply voltage. The flow rate results show ≈15% hysteresis at ±35V demand. The bandwidth of the valve was 284Hz at -90 degrees phase frequency.

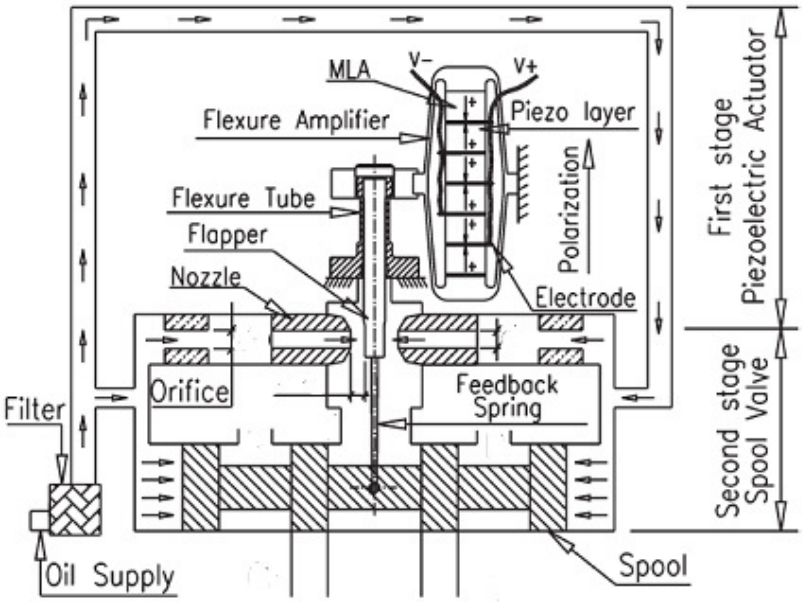

Figure 1.7: Schematic of the servovalve developed by Karunanidhi et al. [3]

Lindler and Anderson [26] developed a direct drive piezoelectric valve. The cross-section of the valve is shown in Figure 1.8. The stroke of the stack actuator was amplified by the vertical lever element. At 60µm nominal actuator stroke the spool stroke was 0.3mm. The maximum drive voltage of the actuator was 800V. The valve demonstrated a flow rate of 9l/min at 100bar supply pressure. The dynamic response was reported to be affected by a low system natural frequency and lack of damping.

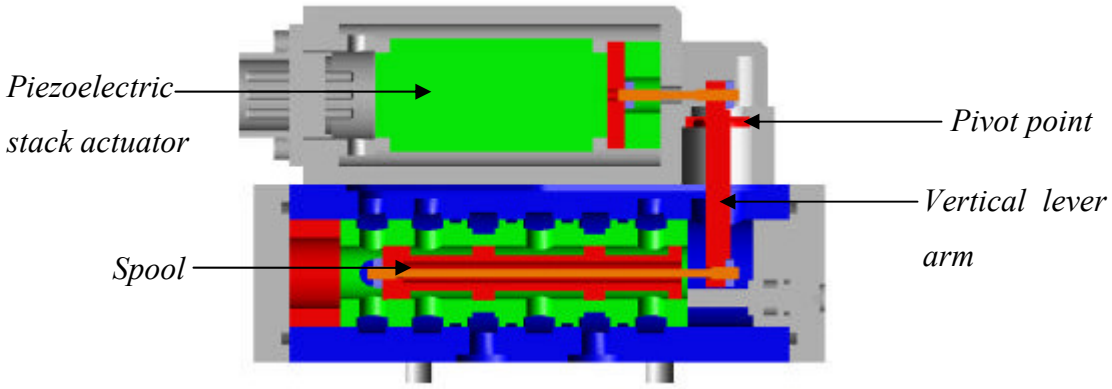

Figure 1.8: Direct drive servovalve developed by Lindler and Anderson [26]

Modern diesel fuel injection systems use piezoelectric stacks to actuate the injector control valve [27], [28], [29]. MacLachlan et al.[30] developed a hydraulic unit injector using stroke amplified piezoelectric stack actuators. A preloaded spring was used to prestress the actuators. The control valve in the injector was directly driven by the actuator assembly. The assembly produced a stroke of 480µm and a driving force of 26N at 250V applied voltage. Dynamic test results of the system show the -3dB bandwidth of the valve to be just over 1kHz with the first natural frequency of the system at 625Hz. The phase response of the system was reported to be greatly compromised due to nonlinearities in the actuator assembly.

Reichert [31] developed a two stage servovalve using piezoelectric stack actuators at the first stage. The valve comprised a conventional second stage and a novel first stage consisting of four pilot valves. Each pilot valve was a poppet valve proportionally driven by a piezoelectric actuator. Figure 1.9 shows a cross section of the developed valve. P_{AV} and P_{BV} are the pilot stage pressures, A and B are the load pressures, and P and T represent supply and tank pressures, respectively. Each piezoelectric actuator produced a stroke of 40µm and a driving force of 2000N at an operating voltage of 160V. Electronic feedback of the second stage spool was used. Hysteresis effects of the actuators were avoided by using a charge amplifier instead of conventional voltage amplifiers. The disadvantage is the need for additional electric circuits and thus the increased complexity and cost of the control hardware. At an input signal of 90% the -3dB frequency of the valve is reported to be at 130Hz and the -90 degrees phase frequency at 250Hz.

Zhou et al. [32] developed a piezoelectric direct drive valve using multilayer stack actuators. The objective of the work was to develop a control strategy to compensate for the nonlinearities such as hysteresis and creep associated with piezoelectric actuators. A self-adjusting fuzzy controller was used to reduce the tracking error of the spool to less than 0.64µm for arbitrary response inputs. The maximum spool stroke was 16µm and the bandwidth of the valve was approximately 1500Hz.

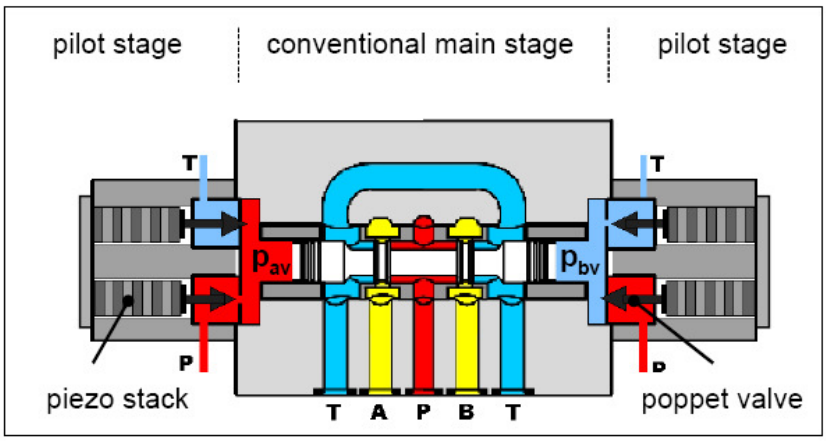

Figure 1.9: Two stage servovalve developed by Reichert [31]

Brader and Rochelean [33] successfully developed and tested a piezoelectrically controlled hydraulic actuator for camless engines. The actuator assembly comprised a pair of multilayer stack actuators, a mechanical stroke amplifier and a hydraulic stroke amplifier. The schematic of the engine valve assembly is shown in Figure 1.10. The actuators were differentially operated with a maximum operating voltage of 200V. Differential operation of a pair of actuators is known to reduce the effect of hysteresis on system performance [25]. The prototype was claimed to improve engine performance by demonstrating variable valve timing, displacement and velocity. Operating frequencies exceeding 500Hz were achieved with the valve.

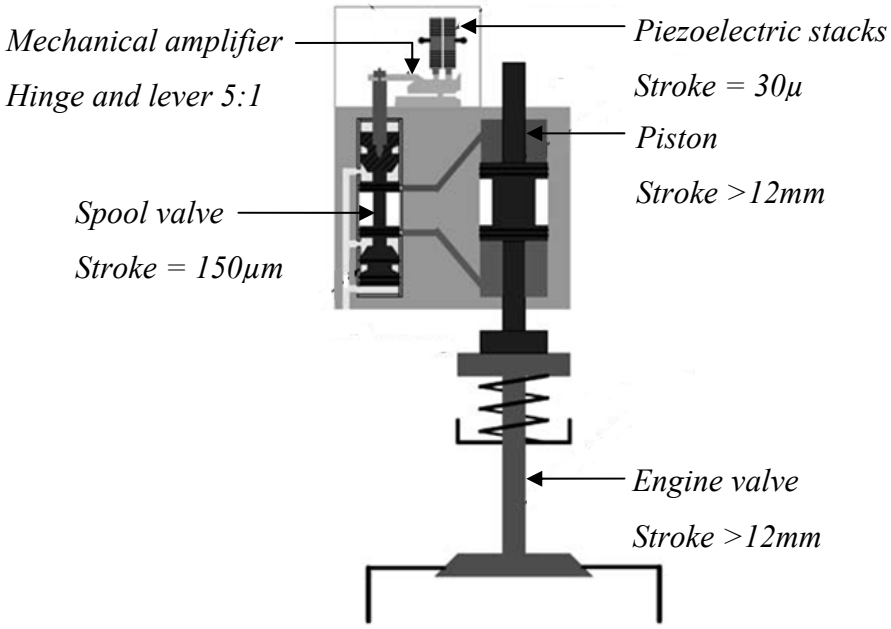

Figure 1.10: Piezoelectric hydraulic actuator for camless engines developed by Brader and Rochelean [33]

Milecki [34] developed a two stage servovalve using a piezoelectric bimorph actuator at the first stage. The bimorph actuator replaced the flapper in a conventional nozzle-flapper servovalve and used electronic feedback of the second stage spool. The actuator was capable of producing a maximum stroke of 160µm and a blocking force of 2N at operating voltages of ±30V. The dynamic response of the valve was reported to be compromised by stability issues. Hysteresis effects were also reported to dominate valve performance.

Similar to Milecki, Sedziak [35] developed a bimorph actuated two stage nozzle-flapper servovalve. The bimorph actuator directly replaced the pilot stage flapper. The second stage spool was spring loaded on either end to produce proportional flow. The schematic of this set up is shown in Figure 1.11. The actuator used by Sedziak had an inherently low hysteresis characteristic due to its operating principle (differential operation of a pair of actuators). However, this was not replicated in the flow measurement of the valve. The hysteresis of the valve was ≈13%. Maximum flow of 24l/min was achieved with a supply pressure of 240bar.

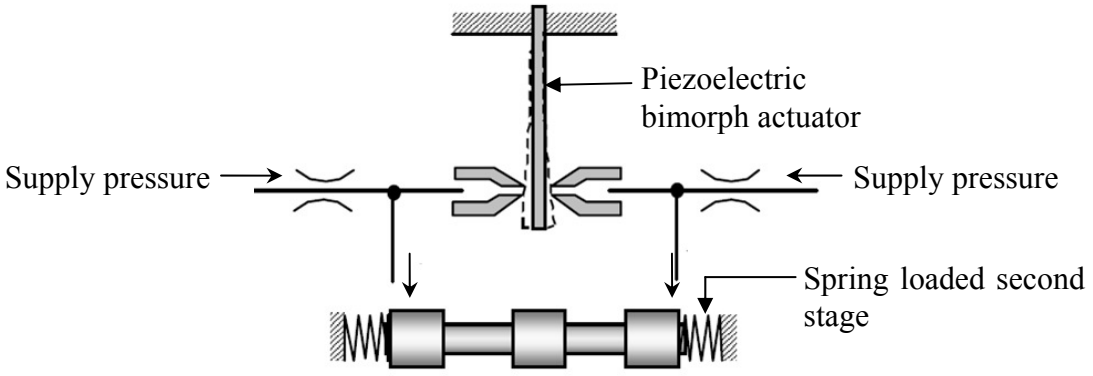

Figure 1.11: Schematic of the valve developed by Sedziak [35]

As an alternative to the conventional nozzle-flapper first stage arrangement, Murrenhoff [36] described a first stage comprising of two flappers, one for each nozzle. This arrangement facilitates differential operation of the nozzles which improves the first stage quiescent leakage during static operating conditions. Piezoelectric bimorph actuators were used as the flapper mechanism. Electronic feedback of the second stage spool was used to facilitate proportional flow. The -90 degrees frequency response of the valve at 150bar supply pressure and 80% demand approached 400Hz.

Murrenhoff [36] also described a direct acting piezoelectric servovalve using stack type actuators. The limited stroke of the actuator was enhanced by a silicone filled hydrostatic transformer. A pair of piezoelectric drive assemblies was used on either end of the spool to compensate for thermal expansion. The rated flow of the valve was 70l/min at 70bar pressure drop. The -90 degrees frequency response of the valve approached 270Hz at 50% demand.

In addition to high flow proportional valves, piezoelectric actuators have been successfully applied in digital hydraulic valves[37], cartridge valves[38] poppet valves [39] and micro valves[40]. They have also been applied in micropump applications [41], [42], [43]. These actuators have also proven to be an attractive solution for active instability control in gas turbines [44] [45]. In this application, fuel is pulsed to generate heat release rate perturbations that damp pressure

fluctuations in the combustor. Similarly, piezoelectric actuators have been used to reduce fluid pulsations in high pressure hydraulic pipeline systems [46].

1.5 Motivation for this research

High performance hydraulic servo systems use servovalves as the primary power modulation unit. The dynamic response of these valves influences the overall system performance. In two stage servovalves the first stage actuator response is known to be the dominant factor influencing the overall valve performance. In recent years the performance envelopes of servovalves have been improved by using active material actuators at the first stage. The superior bandwidth, stability and lower cost of piezoelectric materials compared to other active materials, have made piezoelectric actuators a potential alternative to the first stage torque motor in servovalves.

The stroke of a servovalve first stage ranges between 100µm - 200µm [47], [48]. Flow forces can be up to 5N [49] depending on the hydraulic amplifier and supply pressure. Conventional bimorph actuators are known for their high displacement (≈ 1mm) and limited blocking force (≈0.5N) [50]. The force limitation of bimorph actuators has made the stack actuator the prominent alternative to the electromagnetic torque motor in servovalves.

The driving forces of typical stack actuators are generally in the range of 1kN [50]. This large force capability makes the stack oversized for the servovalve first stage. The stroke amplification required due to their limited stroke reduces the available force. This compromises the efficiency of the actuator due to compliances in the stroke amplification mechanism and contributes to cost and complexity of the design. Hysteresis and thermal expansion effects are also known to compromise performance. These effects need to be compensated for in the actuator assembly. The high operating voltages of these actuators make them susceptible to self heating. This will become a concern at high operating frequencies and cooling needs to be considered. Compensating for these effects make the implementation of these actuators complex and costly. As a result of these disadvantages, no piezoelectric servovalve concept has yet been found to be commercially viable.

1.6 Aims and objectives

The aim of this research is to investigate a novel technique for fluid metering using active materials in order to reduce existing device complexity and cost, with application to servovalves. The objectives of the project are categorised into 4 major groups:

i. Concept design. The objective is to design a servovalve with active material driven first stage to reduce complexity (and potentially manufacturing cost) compared to existing valves.

ii. Simulation of the valve. The objective is to develop and simulate a detailed analytical model of the valve to predict the valve performance. The model would help identify the main parameters that influence the valve performance.

iii. Experimental testing. The objective is to build and test the valve prototype. The experiment results are compared to the simulation results to validate the modelling.

iv. Optimisation of the design. The objective is to develop a methodology to optimise the first stage assembly configurations to improve the valve performance.

1.7 Original contribution

i. Design and construction of first piezoelectric bimorph valve with mechanical feedback, for which patent application has been filed (international patent application number PCT/GB2011/050502)

ii. Understanding of performance characteristics of valve, through validation of simulation model against experimental results.

iii. Understanding of sensitivity of valve performance to changes in design parameters, with validation through testing a ‘Mark-2’ valve.

iv. CFD investigation of a vortex valve concept (see Appendix A)

1.8 Scope and order of the thesis

This thesis has been organised into six chapters. Chapter 1 presented an overview of existing servovalve technology and the current research trends in the field. Subsequently, the motivation for the research was defined and the research objectives were specified. Chapter 2 describes the concept evaluation and actuator choice. The integration of the actuator in the first stage assembly is presented. Details of the operating principle of the prototype valve are discussed.

Chapter 3 discusses the modelling and simulation results of the developed valve. A steady state analytical model and a finite element analysis (FEA) model of the first stage actuator assembly are developed. From these models the stiffness constants of the first stage are derived. Computational fluid dynamics (CFD) is used to analyse the first stage flow dynamics to determine the flow force. Subsequently, a higher order nonlinear analytical model of the valve is developed and simulated. A hysteresis model for the first stage actuator is included and extended to the overall valve performance. The nonlinear model is linearised to establish the most important parameters that influence the valve performance.

Chapter 4 presents the experimental set up and the test results of the developed valve. The responses of the valve at varying operating conditions are analysed and are compared to the simulation results. The performance of the valve is discussed in relation to the donor valve performance.

In chapter 5 the stiffness constants of the first stage assembly are redefined in terms of ratios between the forward and feedback path variables of the valve system. The performance of the valve is evaluated in terms of these ratios to optimise the first stage assembly design.

Chapter 6 concludes the research and considers future work.

Appendix - A: - A vortex valve for flow control in fluid system. This section presents an alternative concept investigated during the PhD for fluid metering using power fluidics.

Chapter 2

Concept evaluation, design, integration and operating principle of the piezohydraulic servovalve

2.1 Introduction

This chapter discusses the concept evaluation, design details and operating principle of the piezohydraulic servovalve (PHSV). The justification for the selection of piezoelectric actuator and first stage hydraulic amplifier is presented. Details of the operating principle of the piezoelectric multilayer bimorph and its advantage over conventional piezoelectric bimorphs are discussed. The principle of piezoelectricity is also briefly reviewed.

2.2 Concepts

2.2.1 Concept generation

Figure 2.1 is a flow chart based on existing literature and common knowledge, categorising possible approaches that could be pursued in order to realise the fluid metering application. The chart was populated using the available power sources for the application (hydraulic or electrical) and subdividing them into various different control methodologies. From this various concepts were developed. The main concepts considered for this research are presented next.

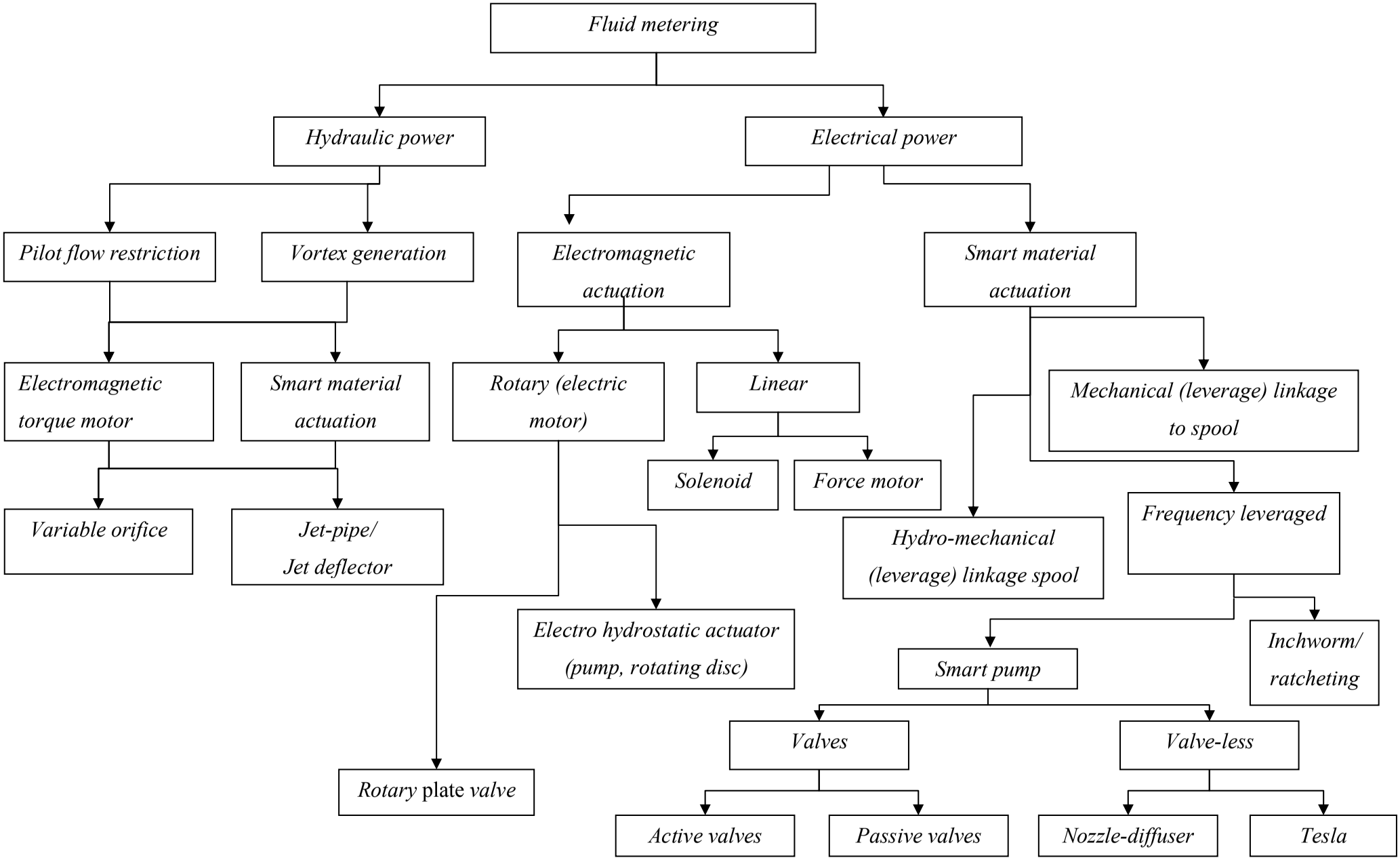

Figure 2.1: Concept flow chart

2.2.2 Two stage variable orifice concept

The two stage variable orifice concept comprises two fixed orifices and two variable orifices moving a conventional main stage spool, as shown in Figure 2.2. The variable orifices are controlled using active materials. Various methods of varying the orifice to create flow restriction are considered below. The potential advantage of this approach to conventional servovalves is the increased bandwidth.

Figure 2.3 shows a bimorph operated nozzle flapper concept using a piezoelectric bimorph to vary the orifices at the first stage. The bimorph replaces the electromagnetic torque motor in conventional servovalves and act as an active flapper. Although the concept is simple and potentially cost effective a disadvantage is the limited force capability of bimorphs (≈2N).

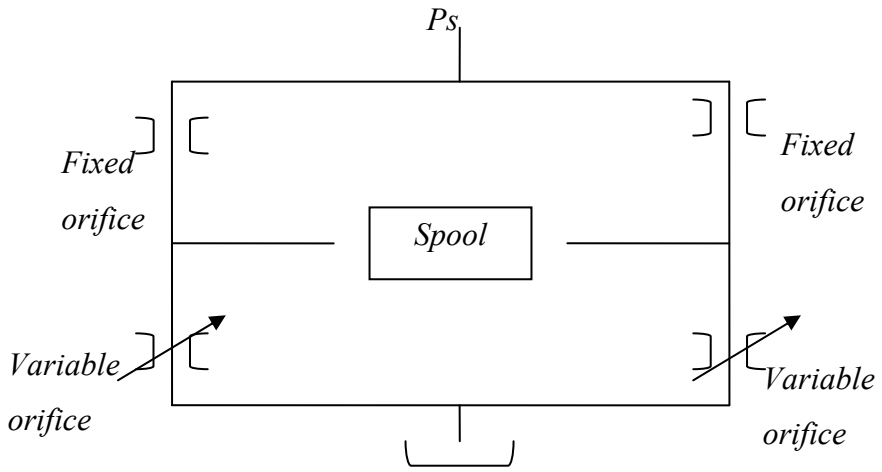

Figure 2.2: Two stage variable orifice concept

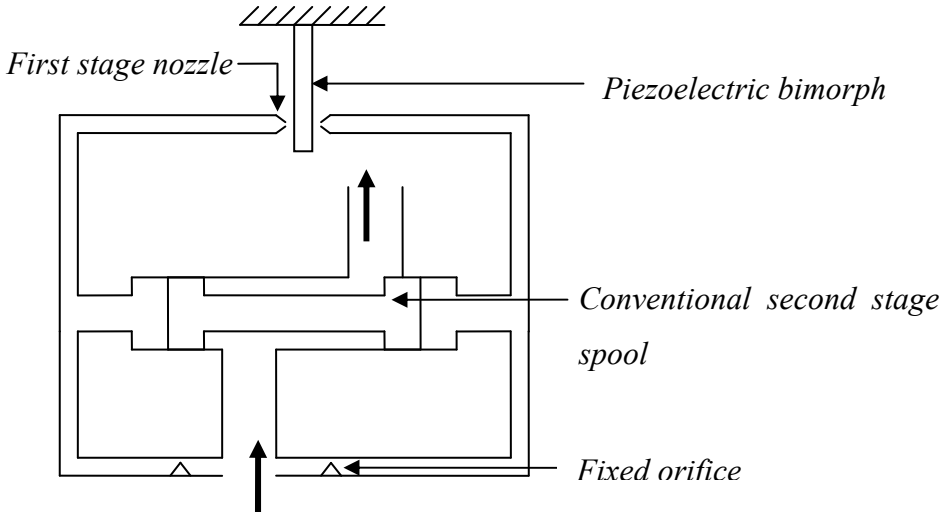

Figure 2.3: Bimorph operated nozzle flapper

Figure 2.4 shows a piezoelectric stack operated nozzle flapper concept. Stacks are capable of producing significantly large forces (in the 1000N range), however much of the force is expected to compensate for displacement amplification. The length of the flapper and distance between the stacks will determine the eventual force capability of the system. The requirement of high drive voltages (150V-1000V) for stacks may have safety concerns. The requirement of a frictionless sleeve to isolate the actuator from the hydraulics increases the cost and complexity of the concept.

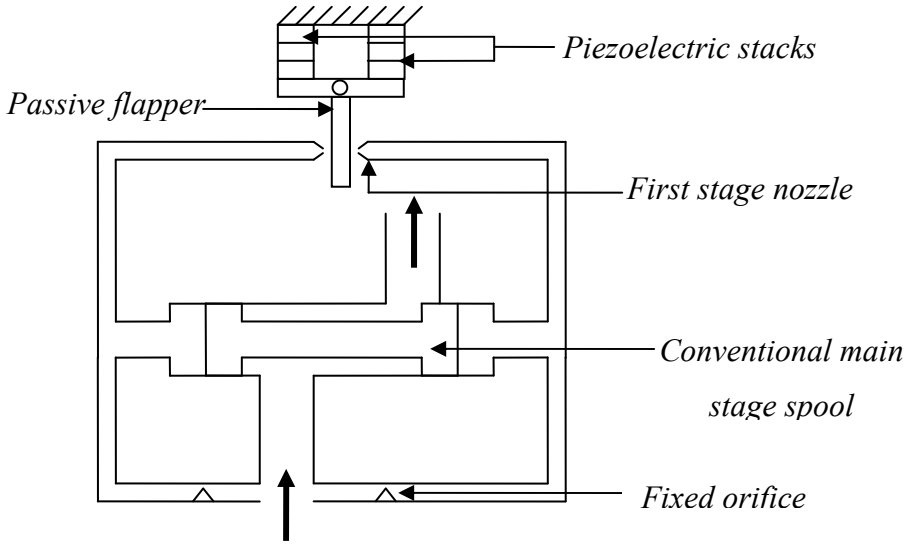

Figure 2.4: Stack operated nozzle flapper

Figure 2.5 shows a needle valve concept comprising a directly driven needle at the first stage and a conventional second stage. If the displacement achieved by the direct driven needle is insufficient to create the necessary flow variations, then some form of amplification mechanism is needed between the stack and the needle. This can increase the complexity of the concept. In addition thermal expansion can influence the valve performance. However, the concept has potential for large force activation and is also less prone to contamination failures compared to other concepts discussed thus far. This is because the needle valve concept has the flexibility of fully opening the needles if the orifices become blocked with contaminants.

Similarly, Figure 2.6 shows a differentially operated orifice concept. The orifices are opened and closed directly by the piezoelectric actuators. Figure 2.6 shows stack actuators however this concept can be applied with bimorphs too. Similar to the needle valve concept this concept is susceptible to thermal expansion issues.

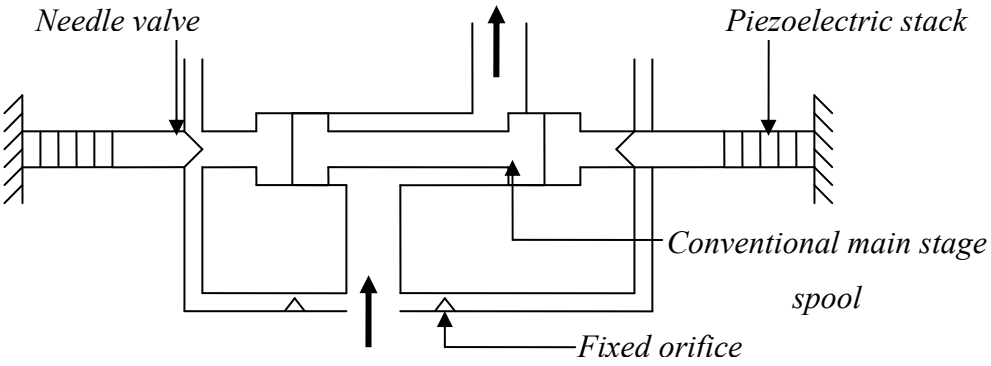

Figure 2.5: Needle valve

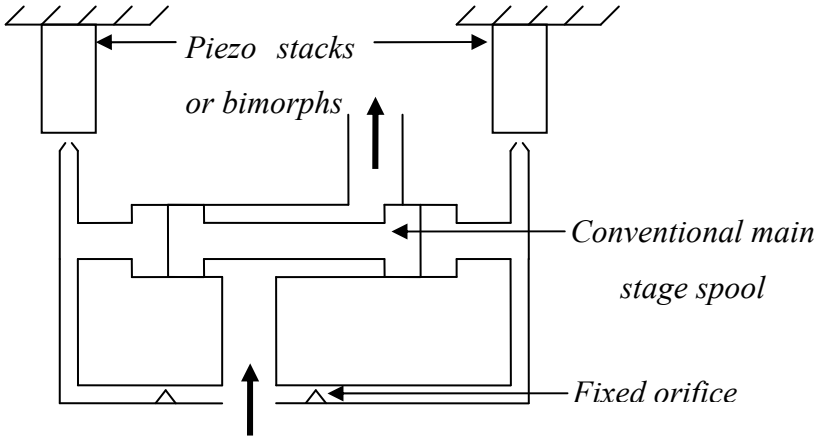

Figure 2.6: Differentially operated orifices

2.2.3 Single stage dual actuation concept

The single stage dual actuation concept uses a conventional direct drive actuation to drive the main stage spool and in addition incorporates a piezoelectric stack for high frequency modulation. Figure 2.7 shows a conventionally driven spool at the main stage and a stack actuated valve sleeve. The control of the valve sleeve will determine the high frequency response and the conventional drive will provide the low frequency response of the spool, such that the end to end movement. Hysteresis and thermal expansion of the stack actuator will have to be compensated.

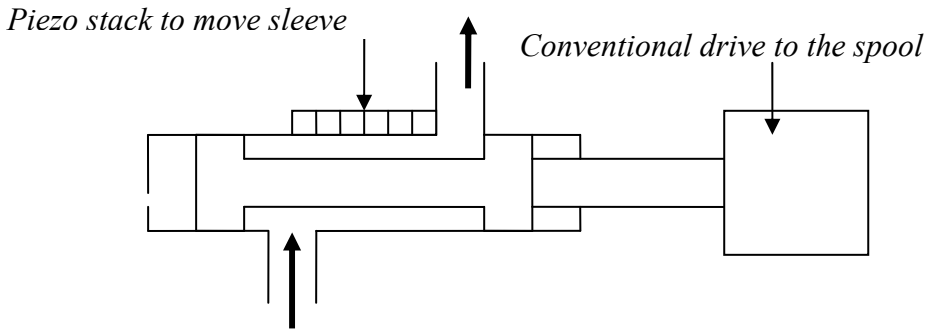

Figure 2.7: Single stage active sleeve concept

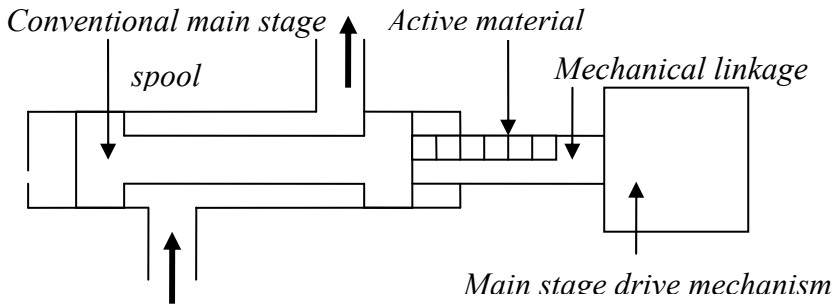

Figure 2.8: Single stage dual actuator

A variation of the concept is shown in Figure 2.8. A conventional spool driving mechanism which uses a mechanical linkage to the spool is used to provide the low frequency response of the spool. The stack actuator will be located in the mechanical linkage which drives the spool, which will provide the high frequency response. The challenge will be to integrate the stack actuator into the linkage and transfer the dynamic performance of the stack to the spool.

2.2.4 Vortex valve concept

The vortex valve concept comprises a vented vortex valve configuration at the second stage and a piezoelectric (bimorph/stack) actuator at the first stage. An attractive feature of the concept is the lack of mechanical moving parts at the second stage, which improves reliability. A rudimentary vortex valve is shown in Figure 2.9.

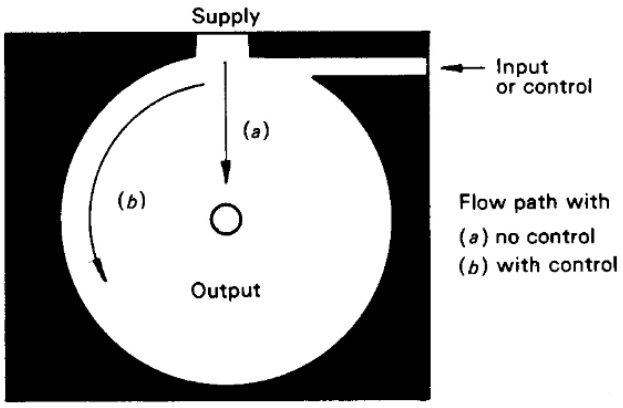

Figure 2.9: Schematic of vortex valve[51]

The supply flow enters a circular chamber and leaves through a hole in the centre of the chamber as shown in Figure 2.9. A control jet, at a higher pressure than the supply, is placed at right angles to the incoming supply flow. With no control flow the valve presents simply an orifice resistance. The outlet pressure is determined by the pressure losses at the inlet and outlet orifice. When there is a control flow, the flow moves in a spiral path inside the chamber. To realise complete flow modulation a flow pickoff is incorporated to the valve design as shown in Figure 2.10.

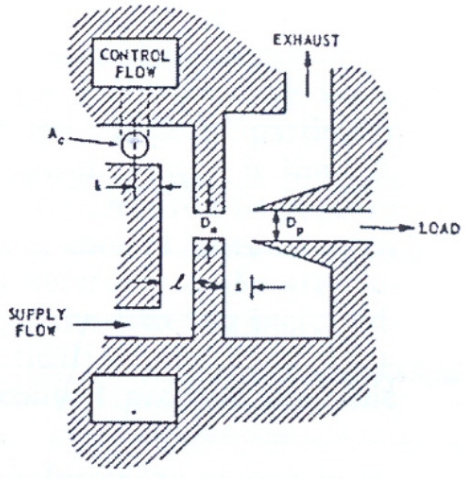

Figure 2.10: Schematic of flow vortex valve incorporated with flow pickoff [52].

The flow pickoff is a tubular flow receiver located concentric to the vortex valve outlet with a clearance. With no control flow the flow exiting the vortex chamber is a well-defined jet. The flow is recovered at the flow pickoff. When a control flow is introduced, it induces a vortex flow field. The flow leaving the vortex chamber spreads out into a hollow conical shape resulting from the tangential flow momentum. This cone of fluid impinges on the flow pickoff and some is diverted. Increasing the control flow will ultimately result in all of the exiting flow missing the pickoff.

2.2.5 Jet pipe concept

Two piezoelectric stacks are used to rotate the jet pipe to meter the jet into the two control ports to create a pressure difference across the spool, as shown in Figure 2.11. This concept is less prone to contamination compared to the variable orifice concept and is fail-safe. This is because the smallest orifice in the valve is that of the supply jet. If blocked, then the valve would fail at its null position. This will allow a redundant system to take over. However, coupling the jet pipe to the actuator and high drive voltages are challenging for the concept. High drive voltages are associated with increased hysteresis which needs to be compensated for.

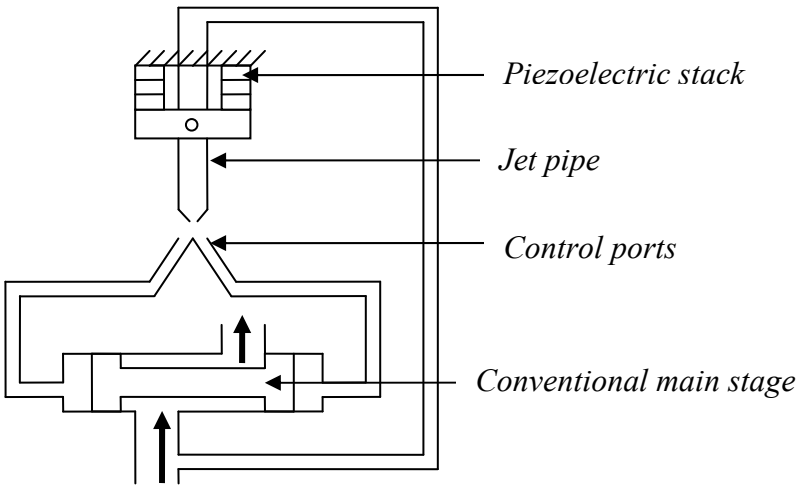

Figure 2.11: Jet pipe concept

2.2.6 Deflector jet concept

The deflector jet concept is similar to the jet pipe in that it has two receiver ports at the first stage into which the fluid is metered. Unlike the jet pipe, the supply nozzle in the deflector jet is fixed and a jet deflector between the supply nozzle and the receiver ports controls the flow into the control ports. The actuation of the jet deflector can be a bimorph actuator which is directly coupled to the deflector. The advantage of this concept over the je pipe is the simplicity of the actuator coupling.

2.2.7 Gear pump concept

A gear pump concept at the first stage is shown in Figure 2.12. The wheel is driven by a bidirectional electromagnetic motor. This will generate the flow in the pilot stage to move the spool in the main stage. Electronic feedback of the main stage spool is required to achieve proportional flow through the valve.

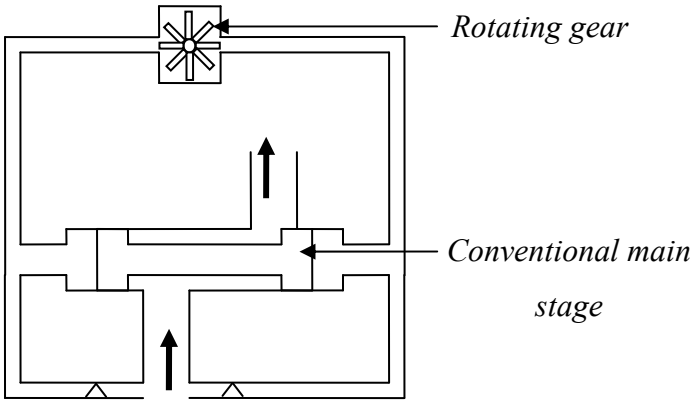

Figure 2.12: Gear pump concept

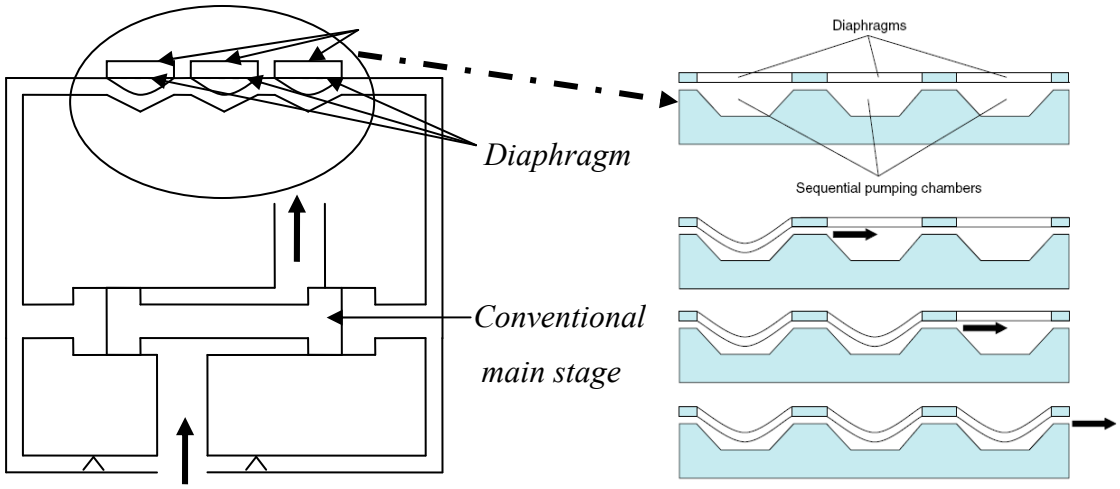

Figure 2.13: Piezo pump concept

2.2.8 Piezo pump concept

Figure 2.13 shows a piezo pump concept comprising a peristaltic piezo pump at the first stage and a conventional second stage. The Figure also incorporates the structure and operation of the piezoelectric bimorphs obtained from [53]. Three independently actuated piezoelectric bimorph elements are used to create a pumping mechanism. Sequential operation of the bimorphs will determine the direction of flow and their operating frequency will determine the flow rates.

2.2.9 Flexible valve concept

Figure 2.14 shows a novel flexible valve concept. This concept comprises a pilot spool which is drilled through to allow flow to the spacing between the pilot spool face and the flexure mechanism. One end of the spool is spring suspended and the other end opens to a flexible mechanism. The flexible mechanism could be a piezoelectric bender or a flexure actuated by a piezo stack. The type of actuator for the flexure mechanism will be determined by the force and displacement requirements.

The restriction to the flow, through the pilot spool, will be determined by the spacing between the spool and the flexing mechanism. The restricting orifices will be the

variable spacing between the flexure mechanism and the pilot spool inlet edge and the spacing between the flexure mechanism and the pilot spool outlet edge, shown in Figure 2.14. The pressure drop between these two orifices will determine the force acting on the face of the pilot spool and thus move the pilot spool. Movement of the pilot spool will variably restrict the pilot flow to the main stage spool and thus create a pressure difference across it, which will result in the main stage spool being displaced.

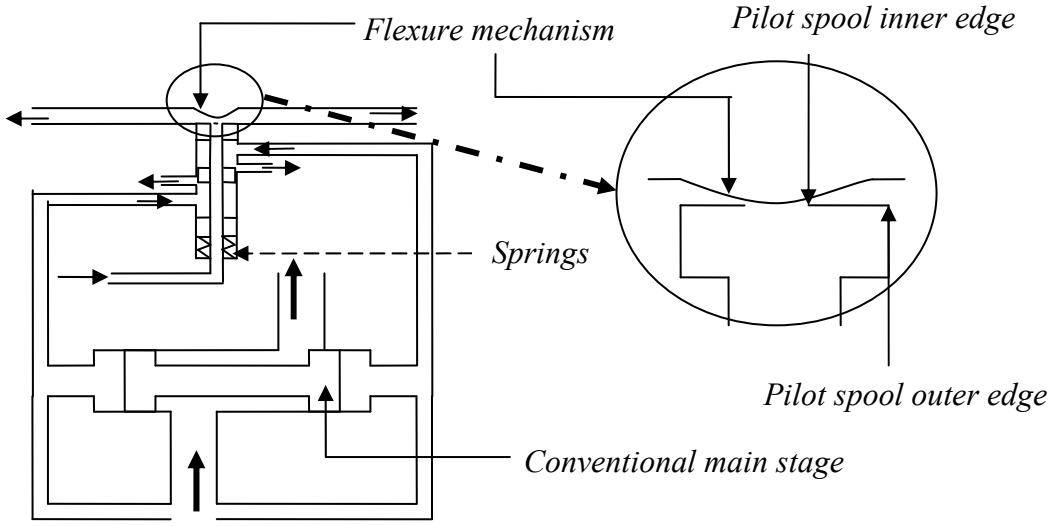

Figure 2.14: Flexible valve concept

2.3 Concept evaluation

The aim of the concept evaluation process is to identify the two most promising concepts and develop them in parallel. Other concepts will be eliminated. The evaluations of the concepts were based on an advanced decision matrix which incorporates robust decision making based on a Bayesian method *Belief* model. The term "robust" is used to refer to decisions that are as insensitive as possible to the uncertainty, incompleteness, and evolution of the information that they are based on [54]. By incorporating the belief model into the decision matrix, the matrix becomes capable of handling uncertain and incomplete information. The belief model states:

$$Belief = P(k) * P(c) + [1 - P(k)] * [1 - P(c)], \quad 0<\text{belief}<1$$

Where *P(k)* is the probability of knowledge and is a measure of the availability of information on the criterion, and *P(c)* is the probability of confidence, which is a measure of the level of confidence on meeting the criterion. These two parameters are shown in Figure 2.15 and Figure 2.16, respectively.

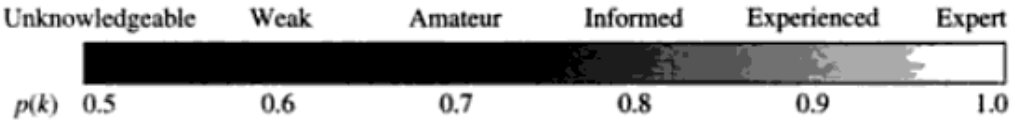

Figure 2.15: Knowledge scale [54]

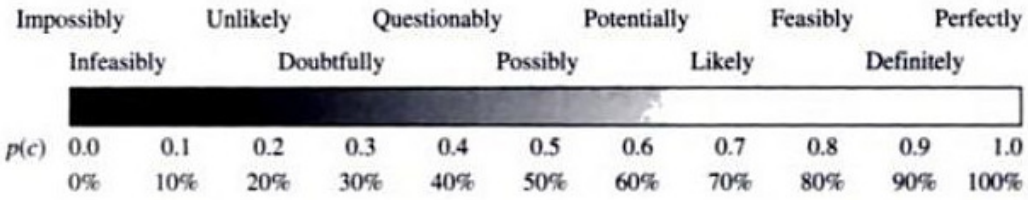

Figure 2.16: Confidence scale [54]

The target market for the valve developed in this research is for aerospace applications and in particular civil aviation. This will determine the main criteria to be used to evaluate the concepts. Safety, reliability, cost, weight, novelty and complexity were chosen.

Safety is paramount in civil aviation. Factors considered within this criterion are drive voltages and redundancies within the concepts. Reliability of the concepts is determined by the number of novel parts and susceptibility to contaminations. Cost is determined by the number of parts, the type of actuators and the number of actuators. Weight is determined by the parts count and the size and density of the materials. Complexity takes into factors such as assembly and compensations required to address thermal and hysteresis effects. The scored decision matrix, based on [54], is shown in Table 2.

Criteria	***Weighting***	***Importance***	***Two stage variable orifice***	***Single stage dual actuation***	***Vortex valve***	***Jet pipe***	***Deflector jet***	***Gear pump***	***Piezo pump***	***Flexible valve***
Safety	*5*	*18*	*0.50*	*0.48*	*0.54*	*0.54*	*0.66*	*0.54*	*0.48*	*0.50*
Reliability	*5*	*18*	*0.54*	*0.44*	*0.68*	*0.62*	*0.66*	*0.58*	*0.44*	*0.50*
Cost	*4*	*15*	*0.62*	*0.34*	*0.80*	*0.46*	*0.70*	*0.62*	*0.32*	*0.56*
Weight	*3*	*11*	*0.62*	*0.20*	*0.62*	*0.56*	*0.80*	*0.32*	*0.44*	*0.44*
Novelty	*5*	*18*	*0.62*	*0.62*	*0.74*	*0.62*	*0.66*	*0.44*	*0.74*	*0.74*
Complexity	*4*	*15*	*0.50*	*0.50*	*0.50*	*0.50*	*0.70*	*0.50*	*0.44*	*0.50*
Satisfaction			***56.3***	***44.6***	***64.7***	***54.9***	***68.9***	***51.3***	***47.9***	***54.7***

Table 2-1: Decision matrix

From the Decision matrix it is evident that the most promising concept is the deflector jet. The vortex valve concept also scores highly. The remaining concepts are all near a satisfaction factor of 55% and thus do not promise an overall significant advantage to the current unit.

The flow forces generated at the first stage of a nozzle-flapper servovalve are generally much higher than a deflector jet or a jet pipe servovalve. This is because the flapper moves in the same plane as the jet. The jet impinges directly onto the flapper. In deflector jet and jet pipe servovalves the deflector or the jet pipe moves in an orthogonal plane to the jet. This substantially reduces the flow forces experienced by the pilot stage actuator. In addition the nozzle-flapper configuration is the most susceptible to contamination failure [12] and has a higher quiescent leakage [47] which compromises the efficiency of the valve.

There has been no previous attempt to incorporate a piezoelectric actuator with a deflector jet amplifier at the first stage of a servovalve. The low flow forces at the first stage reduce the force requirement at the deflector. This gives scope for using a mechanical feedback wire which has additional force requirements. The feedback wire provides position feedback of the second stage spool to the first stage. This avoids the need for a position transducer at the spool and a closed loop electronic controller to achieve proportional flow. This simplifies the valve electronics and reduces cost. The low force demands at the first stage of a deflector jet provide scope for low voltage piezoelectric actuators. This improves the safety factor of the concept. In addition the concept is fail-safe as its smallest orifice is the first stage supply. If the orifice gets blocked, then the valve will fail at its mid position. This will allow a redundant system to take over. The piezoelectric actuation selection for this concept is considered next.

2.4 Piezoelectric actuator selection

Piezoelectric elements for application in discrete actuators can be constructed using various techniques from the basic ceramic material. These include multilayer stacks, bimorphs, C-blocks, Rainbow, Thunder and Tubular [55]. These actuator elements

use different modes of operation, such as normal, shear and torsion, to produce motion. Typically, several actuator elements of the same type are added together to increase the output stroke or force. Commercially available materials offer strains of about 0.1%. In recent years, single crystal ceramics have been developed which can generate strains up to 1%. However, these materials have a reduced modulus of elasticity [56] and their manufacture is costly [57].

Stack and bimorph actuators have been used previously for servovalve prototypes. These actuators provide the best compromise between force and stroke whilst maintaining high frequency response. In addition, the commercial maturity of these actuators has driven the costs low making them relatively inexpensive. However, limitations of these actuators (such as trade-off between force and displacement, high operating voltage and hysteresis) have made the implementation of them complex and costly.

Cedrat have developed amplified actuators for aerospace application using flex-tensional deformation of a shell [58]. This actuator can be observed in Figure 1.7. The motion of the stack in the middle of the actuator is amplified by the surrounding flexure mechanism. The flexure mechanism also provides a pre-stress to the stack. However, the disadvantage of using this set up for deflector jet is the high drive voltage and the lack of thermal compensation. In addition these actuators are not encapsulated therefore the actuator assembly needs to be isolated from the hydraulics. This increases the complexity of the concept.

Other types of commercial piezoelectric actuators that have potential as a deflector jet first stage actuator are plate, stacked and bender actuators and ring, stacked and bender actuators [59]. The stroke and force of these actuators are comparable to conventional stack and bimorph actuators. However they require high operating voltages (200V). High operating voltages is a safety concern in aerospace applications.

Recently, monomorph structures in multilayer technology have been developed to reduce the operating voltage and increase the converted mechanical energy per

volume of piezoelectric materials [60]. These actuators comprise several active piezoelectric layers co-fired together with internal electrodes. The resulting actuators have increased performance relative to conventional types due to their increased field strength. In addition they have an inactive layer of ceramic encapsulating the actuator which improves the humidity resistance. This simplifies the concept as the actuator facilitates submerged operation.

Bimorph actuators are generally composed of two layers in differential operation. The strains generated in the two layers need to be different to generate bending. Therefore no net displacement will be observed due to thermal expansion as both layers expand. Hence there is inherent thermal compensation in the actuator structure. In addition having two layers incorporates redundancy as one layer can perform even if the other layer breaks down, however, with reduced performance. Having redundancy is attractive for aerospace application. Also differential operation of the layers will reduce the hysteresis characteristics [25].

Multilayered bimorph actuators with improved force capability have great potential as servovalve first stage actuators. Multilayer bimorph actuators with effective length of 12mm generate a blocking force of 2N, tip displacement of 160µm and resonant frequency greater than 1000Hz [61]. The active layers of these actuators are made from lead zirconate titanate (PZT) ceramic. The layers are sandwiched between silver palladium electrodes. The following section discusses the operating principle of these actuators. The principle of piezoelectricity is also briefly reviewed.

2.5 The multilayer bimorph actuator

2.5.1 Fundamentals of piezoelectricity

The piezoelectricity of these materials arises from the lattice structure of their individual crystals. Figure 2.17 shows a PZT unit cell above and below the Curie temperature. The structure of the crystals is cubic and symmetrical at temperatures greater than a critical temperature known as the Curie temperature [62]. No piezoelectricity is observable at these temperatures due to the symmetric centre of

the cubic structure. At temperatures below the Curie temperature the lattice structure becomes deformed exhibiting a tetragonal or rhombohedral symmetry and the function of an electric dipole [62] (see Figure 2.17b). The unit cells exhibit spontaneous polarisation.

Groups of unit cells with the same orientations form regions of local alignment called Weiss domains. The alignment gives a net dipole moment to the domain. Due to the random distribution of the domain orientations in the ceramic, no piezoelectric behaviour is observable for the material. As the material is ferroelectric the randomly distributed domains can be permanently aligned using a high electric field ($>1 kVmm^{-1}$). This process is known as polarisation and can be observed in Figure 2.18. Once polarised the material is known to exhibit remnant polarisation as the material can be depoled by exceeding the mechanical, thermal and electrical thresholds.

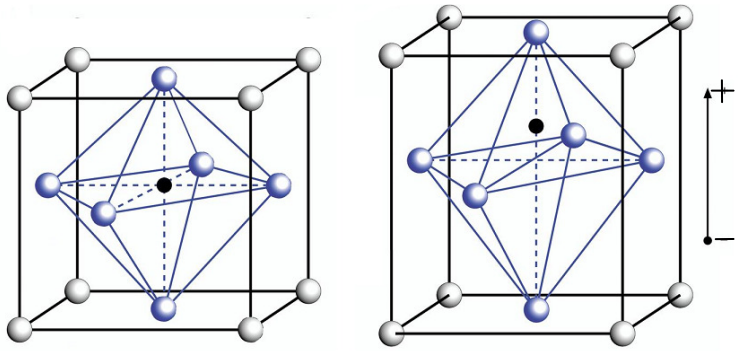

Figure 2.17: PZT unit cell a) Perovskite unit cell in the symmetric cube state above the Curie temperature. b) Tetragonally distorted unit cell below the Curie temperature [23]

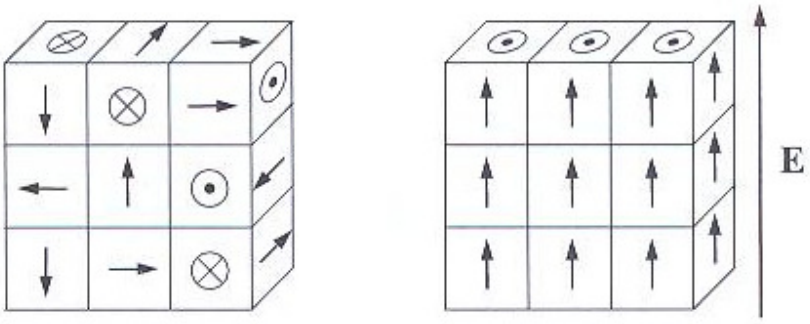

Figure 2.18: Domain orientation with in a ferroelectric single crystal. a) non-polarised crystal. b) polarised crystal [57]

Piezoelectric materials are anisotropic [63]. Therefore the piezoelectric physical constant of a material relates to directions parallel and perpendicular to the applied electric field. Stacks are an example of actuators using the longitudinal piezoelectric effect, parallel to the electric field. Bimorphs are based on the transverse piezoelectric effect, perpendicular to the electric field.

2.5.2 The transverse piezoelectric effect

Applying an electric field to the polarised ceramic will result in spatial alignment of the individual domains. If the field is in the direction of the remnant polarisation, the strain along the electric field direction will result in longitudinal expansion. This expansion is combined with a transverse compression perpendicular to the electric field direction. Reversing the electric field direction will have the opposite effect. This phenomenon is shown in Figure 2.19. In Figure 2.19 ‘P’ indicates polarisation direction and ‘E’ indicates direction of applied electric field.

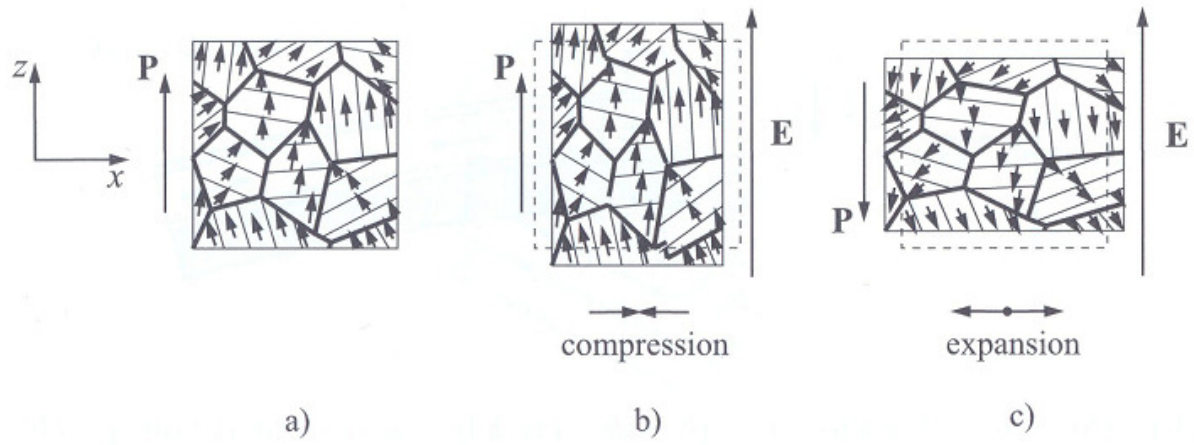

Figure 2.19: Transverse strain behaviour of PZT ceramics – a) polarised state, b) electric field e in the direction of polarization, c) electric field e opposite to the direction of polarisation [57]

The shrinkage of PZT materials is related to d_{31}/d_{33} ratio, which is approximately 0.5 [64]. Considering the longitudinal strain of PZT materials is 0.1%, the transverse strain will be approximately 0.05%. In multilayered bimorph actuators the individual layers are approximately 50µm thick [61]. The length of the layers will be equal to the effective free length of the actuator. For an actuator of effective free length 12mm, the transverse displacement will be approximately 6µm. whereas the longitudinal displacement will be approximately 0.05µm.

The considerably greater transverse displacement of the actuator generates an internal piezoelectric moment when clamped in a cantilever arrangement. The piezoelectric moment bends the actuator. The total bending deflection of the actuator is significantly greater compared to its transverse displacement [57]. Due to the mechanical transformation of small length variations of the ceramic into a bending deformation, it is possible to generate larger tip deflections of the actuator with low operating voltages. The bending deformation can be further increased by adding another layer in antiphase operation.

The stiffness of the actuator can be increased by increasing the number of layers and the layer thickness. This improves the frequency response of the actuator and the blocking force. However, a stiffer actuator compromises the tip displacement.

Increasing the width of the actuator improves the stiffness and the blocking force without compromising tip displacement.

The PL127.10 multilayer bimorph actuator manufactured by Physik Instrumente (PI) was chosen for this project. The generous length of this actuator gave flexibility for choosing various actuator performances by varying the effective free length.

2.5.3 Operating principle of PL127.10 multilayer bimorph actuator

The actuator comprises 27 PZT ceramic layers sandwiched between silver-palladium electrodes in a co-fired process. It also features ceramic encapsulation. Ceramic encapsulation prevents the ingression of water molecules. When water molecules come in contact with the inner electrodes of the multilayer actuator electrolysis occurs. This facilitates the migration of silver ions from the anode to the cathode. As a result silver dendrites grow from the cathode to the anode. This reduces the resistance, eventually leading to breakdown and failure of the actuator [65]. Hydrogen from the electrolysis can lead to semiconductive behaviour due to reductive processes as well as embrittlement and complete destruction of the ceramic compound due to internal stresses [66].

A scanning electron microscopy image of a cut-away section of the bimorph is shown in Figure 2.20. The cracks observed in the middle of the image are a result of the cutting technique used to bisect the actuator. The internal electrode network divides the actuator into two segments of equal capacitance, similar to a conventional bimorph actuator. The ceramic layer arrangement and the internal electrode configuration are shown in Figure 2.21.

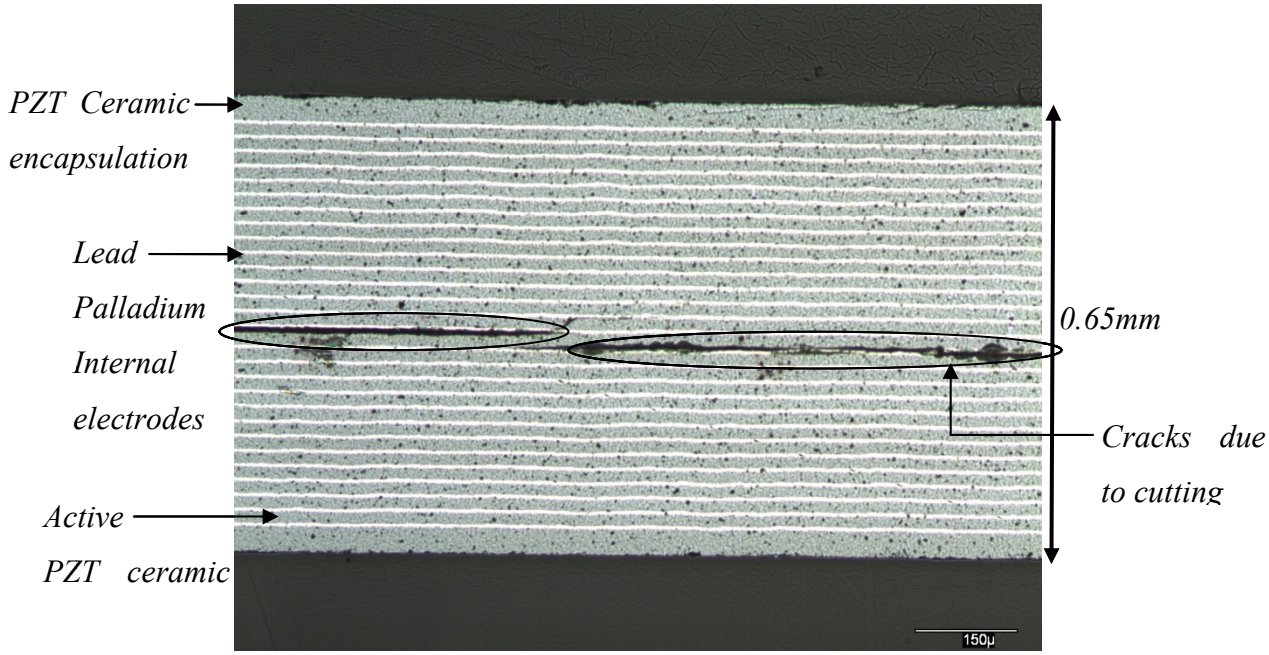

Figure 2.20: Electron microscopy image of the PL127.10 actuator cut-away section

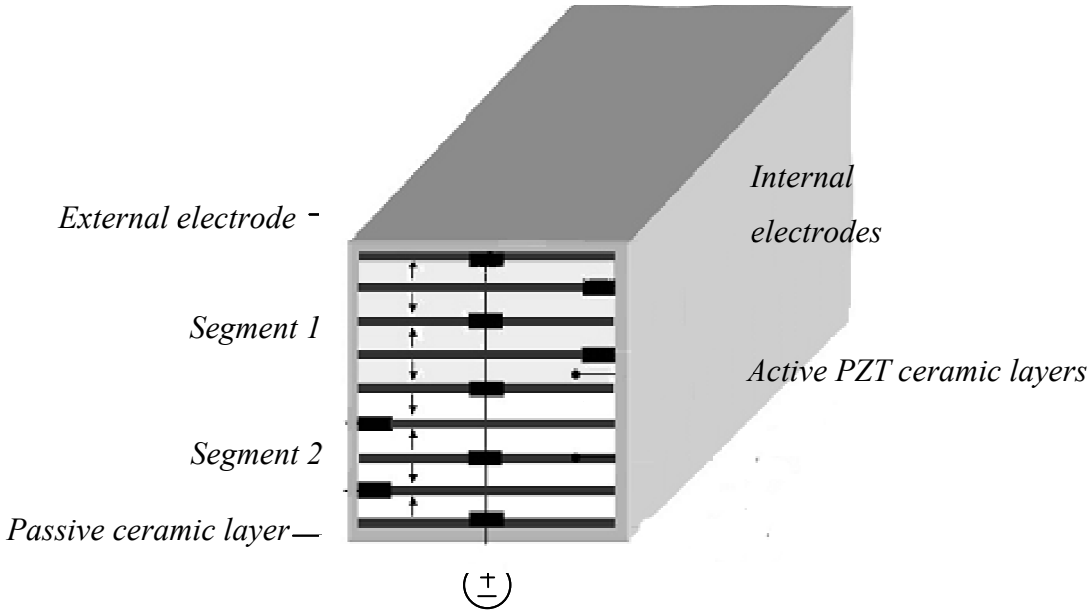

Figure 2.21: Schematic cross section of the multilayer bimorph actuator

The operating voltage of PL127.10 is ±30V. This full differential voltage control is applied to the central electrode, shown in Figure 2.21. The positive and negative electrodes are held at +30V and -30V, respectively. The orientation of the active layers and the polarity of the voltage applied ensure that the direction of the applied voltage is always parallel to the remnant polarisation of the material. This feature enables the material to withstand higher electric field strengths relative to conventional bimorphs. The electrical connections to the external electrodes and the deflection motion of the actuator are shown in Figure 2.22.

When 0V is applied to the central electrode, the potential difference across segments 1 and 2 are equal (30V). Therefore both segments compress by the same amount thus generating no moment. No displacement is observed at the actuator tip. When the voltage to the central electrode is not 0V the potential difference across the two segments are different. The segment with the greater potential difference will compress more. This will generate a resultant moment which will bend the actuator.

For comparison, the cross section of a conventional bimorph actuator is shown in Figure 2.23. The actuator comprises a metal centre shim sandwiched between two active piezoceramic layers. The layers are bonded together using a conductive resin. The ceramic layers have been poled for parallel operation. The central electrode is positive and the two outer electrodes are negative. The drive voltage is varied between ±125V.

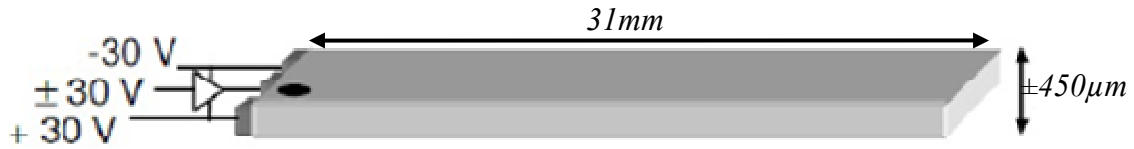

Figure 2.22: External electrical connection to PL127.10 actuator [61]

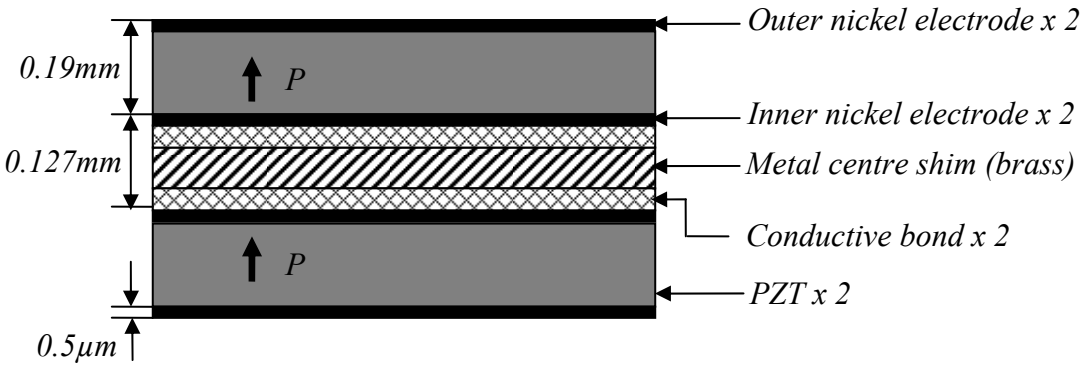

Figure 2.23: Cross section of a conventional bimorph (Piezo Systems)

In conventional bimorphs, bi-directional motion of the actuator tip is achieved by reversing the direction of the applied electric field respective to the remnant polarisation. This significantly reduces the electric field strength that can be applied to the ceramics. The electric field of the ceramics is limited to ≈450V/mm [67] in the direction opposite to polarisation. The limiting field strength is known as the coercive field strength. Exceeding this will depolarise the material. The coercive field strength in the direction of polarisation can be between 1 – 2 kV/mm [39]. This increased field strength improves the strain of the material and thus the deformation [68]. Table 2-2 compares a conventional bimorph actuator to a PL127.10 actuator of similar free length.

	Conventional bimorph	*PL127.10*
Electric field strength (V/mm)	*340*	*1200*
Operating voltage (V)	*±125*	*±30*
Nominal displacement (μm)	*±175*	*±450*
Free length (mm)	*31.8*	*27*
Dimensions (LxWxT)(mm)	*31.8x6.4x0.66*	*31.8x9.6x0.65*
Blocking force(N)	*±0.25*	*±1*
Electrical capacitance (μF)	*5*	*6.8*
Resonant frequency (Hz)	*440*	*380*
Curie temperature (oC)	*350*	*320*
Encapsulated	*No*	*Yes*
Supplier	*Piezo Systems (US)*	*Physik Instrumente (DE)*

Table 2-2: Comparison of PL127.10 actuator to a conventional bimorph actuator

The metal centre shim used in conventional bimorph increases the stiffness of the actuator. This therefore improves the frequency response. However, the tip displacement is substantially smaller compared to PL127.10 actuator. If the PL127.10 actuator free length is reduced to produce the same tip displacement as the conventional bimorph, the blocking force and the frequency response of PL127.10 will be substantially greater. Having defined the deflector jet concept, the next section considers the work done for the vortex valve concept.

2.6 Vortex valve

The detailed information of the development, validation and results of this concept is in Appendix 1.

The vortex valve was designed for optimum performance using published information. In addition CFD was used to determine optimum geometrical configurations. The optimum control port configuration was iteratively obtained for maximum flow gains with minimum increase in control pressure.

The designed valve was capable of delivering the maximum flow of 280l/min of fluid with a 6bar pressure drop at maximum flow. The flow gain of the valve was found to be approximately nine. This flow gain corresponds to a negligible pressure increase in the control port. The flow gain achieved for the valve, for the same control pressure ratio, is very high compared to published literature.

A rotary vortex valve (RVV) was examined which is a novel concept developed to avoid the need for control flows required in conventional vortex valve designs. The valve uses a rotating vortex chamber to generate the vortex. A flow gain of approximately 70 kg/s/^{o} was obtained for the valve. However the characteristic is non-linear. At higher control angles the flow is very sensitive to the angle.

The vortex valve and the rotary vortex valve designs were sensitive to pressure drop between the outlet ports. This characteristic makes the design impractical for the servovalve application. This made the deflector jet the primary concept investigated in this project. The following section considers the development of the proof concept using the deflector jet concept.

2.7 Proof of concept

A Moog 26 series servovalve was chosen as a convenient donor to build the proof of concept valve. Moog 26 series servovalves are 4-way mechanical feedback deflector jet valves used in aero flight controls. Cross-section of a 26series valve is shown in Figure 2.24. Figure 2.25 shows the first stage module of the valve. The rated flow of the valve is 29l/min at 210bar no-load valve pressure drop [69]. At maximum flow the -90 degree phase frequency of the valve is 80Hz [69].

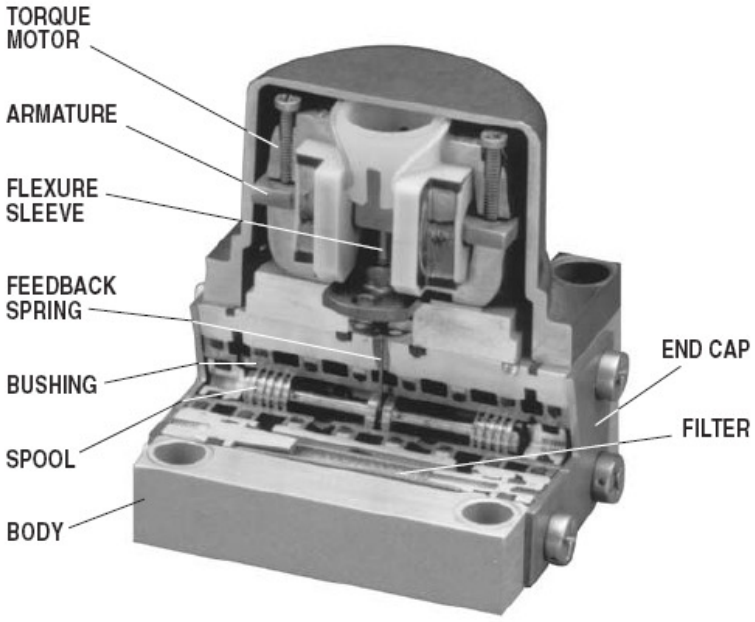

Figure 2.24: Cross-section of Moog 26 series servovalve [69]

Figure 2.25: First stage module of Moog 26 series servovalve [69]

The ceramic encapsulation of PL127.10 actuators facilitate submerged operation of the actuator. This would remove the need for a frictionless seal (flexure tube), present in the torque motor set up. The actuator can be directly coupled to the deflector as shown in Figure 2.26.

The distance between the deflector and the bimorph tip generates a stroke amplification. This stroke amplification compromises the force at the deflector. The deflector displacement of the 26 series valve is approximately ±80µm [70]. The specification of the bimorph actuator is shown in Table 2-3.

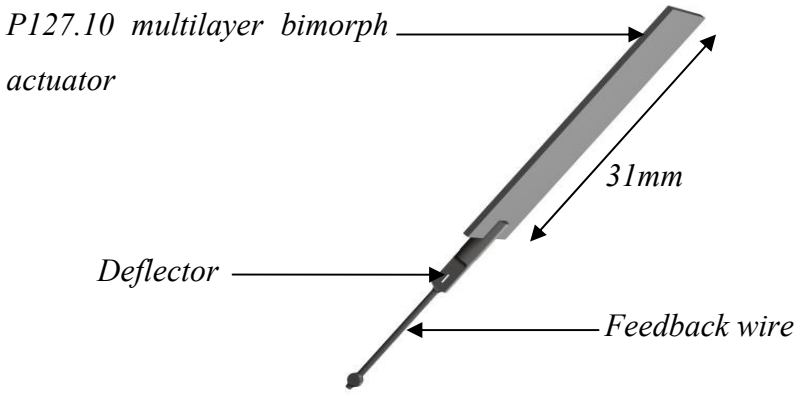

Figure 2.26: Bimorph-feedback wire arrangement.

Operating voltage (V)	*±30*
Nominal free displacement (μm)	*±80*
Free length (mm)	*12*
Dimensions (LxWxT)	*12x9.6x0.65*
Blocking force(N)	*±2*
Electrical capacitance (μF)	*2x3.4*
Resonant frequency (Hz)	*>1000*

Table 2-3: Multilayer bimorph actuator specification

The design constraints of the pilot stage assembly were determined by the existing bolt holes on the first stage amplifier body, bimorph length and the deflector position. Using the existing amplifier bolt holes avoids any modification to the amplifier body. A compact first stage assembly was designed to house the bimorph actuator. A cross section of the valve assembly is shown in Figure 2.27. A second stage valve body with an integrated linear variable differential transformer (LVDT) was chosen to facilitate spool position monitoring. The part description of Figure 2.27 is given in Table 2-4. Figure 2.28 shows a photograph of the assembled piezohydraulic servovalve. A cut-away of the first stage assembly exposing the bimorph-feedback wire assembly is shown in Figure 2.29.

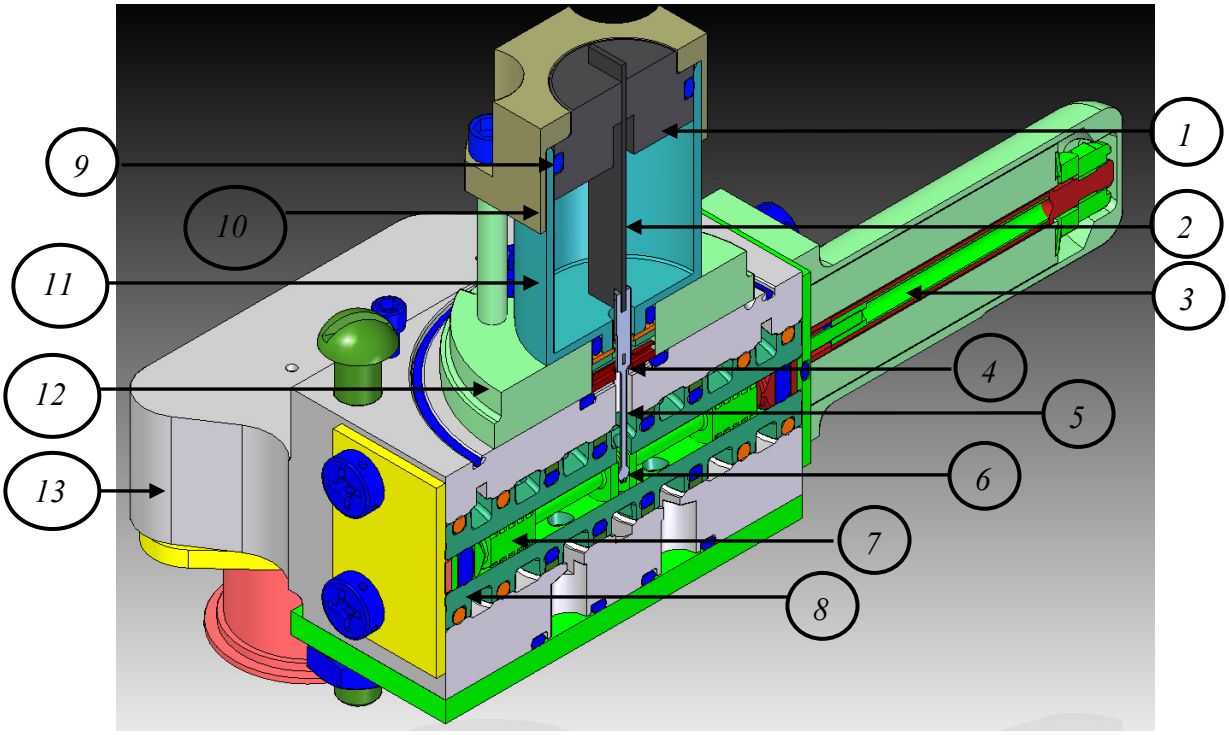

Figure 2.27: Cross section of the PHSV assembly

Part number	***Description***
1	*Actuator clamp*
2	*PL127.10 multilayer bimorph actuator*
3	*Second stage spool LVDT*
4	*Deflector in amplifier assembly*
5	*Feedback wire*
6	*Feedback wire ball*
7	*Second stage spool*
8	*Spool sleeve*
9	*First stage O-ring*
10	*First stage retainer*
11	*First stage enclosure*
12	*First stage amplifier body*
13	*Second stage valve body*

Table 2-4: Part description for Figure 2.27

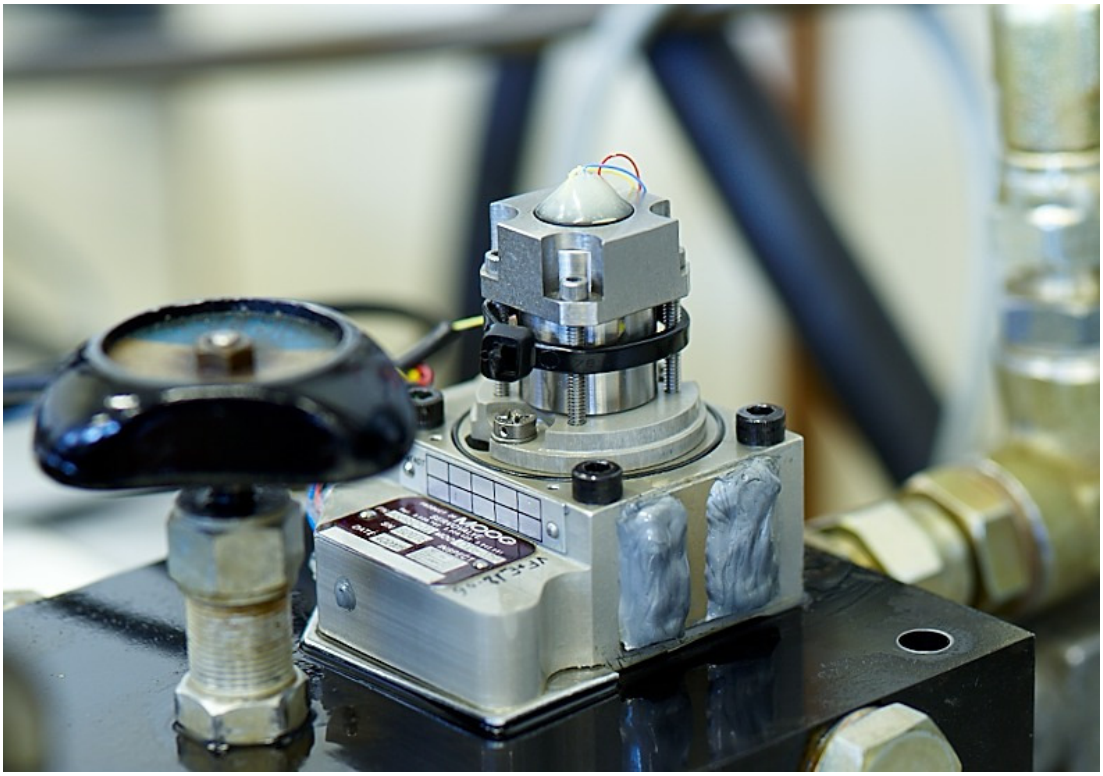

Figure 2.28: Piezohydraulic servovalve prototype

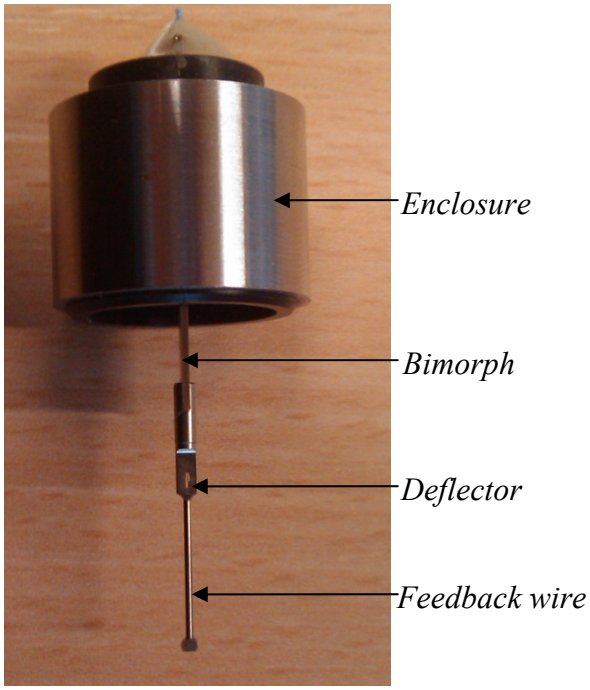

Figure 2.29: Photograph of bimorph-feedback wire assembly

Figure 2.27 shows the simplicity of the first stage design. Potential advantages of using a multilayer bimorph actuator compared to a conventional torque motor are:

i. Improved frequency response, which will improve the overall frequency response of the valve.

ii. Insusceptibility to electromagnetic interference. In addition no generation of electromagnetic radiation.

iii. Reduced number of parts, which can potentially reduce weight and cost of the first stage assembly.

iv. Operation at cryogenic temperatures[71].

2.8 Operating principle of the PHSV

Figure 2.30 shows the schematic cross section of the PHSV. Section A-A of Figure 2.30 is shown in Figure 2.31. Figure 2.31 shows the cross section of the deflector and amplifier arrangement.

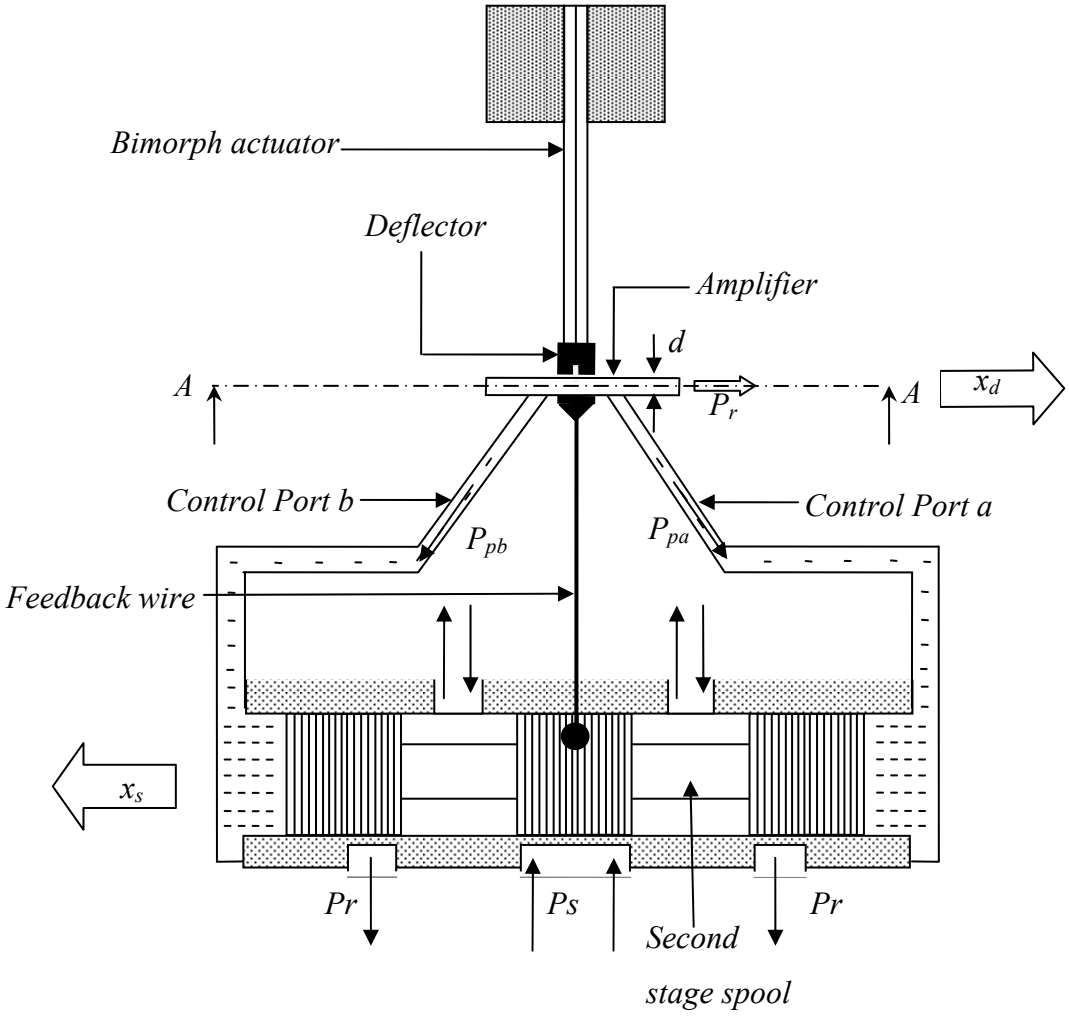

Figure 2.30: Schematic cross section of the PHSV

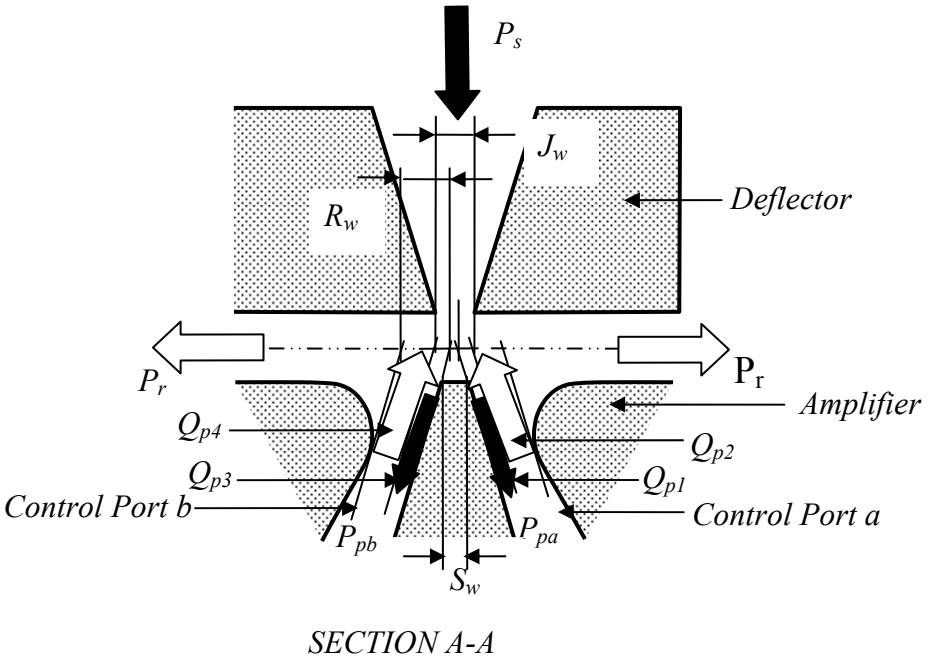

Figure 2.31: Section A-A of Figure 2.30, showing the deflector-amplifier arrangement

The PHSV operation is as follows

1. At the null position (no voltage to the bimorph) the flow from the deflector impinges equally on the control ports, so that the pressure on the main stage spool ends are equal.

2. When a voltage is applied to the piezoelectric actuator, the electric field generates a bending moment along the length of the actuator. The actuator bends and moves the deflector.

3. The displacement of the deflector directs the jet of fluid to one of the two control ports, thus increasing the pressure in that port. This creates a pressure imbalance across the main spool. This differential pressure moves the spool in the opposite direction to the movement of the deflector.

4. As the spool begins to move, it pulls the tip of the feedback wire with it. This generates a restoring force which re-centres the deflector. When the restoring

force due to spool movement is equal to the force at the deflector, the spool stops at that position.

The analytical model of the PHSV will be developed in Chapter 3 based on the above operating principle.

2.9 Conclusion

Piezoelectric elements for application in discrete actuators can be constructed using various techniques from the basic ceramic material. Despite this choice, the stack and bimorph actuators have been the predominant preference for servovalve applications. However, limitations of these actuators have made the implementation of them complex and costly. In recent years, monomorph structures in multilayer technology have been developed to reduce the operating voltage and increase the converted mechanical energy per volume of piezoelectric materials. These actuators have increased performance relative to conventional types.

The PL127.10 multilayer bimorph actuator manufactured by PI was chosen for this project. The multilayer bimorph generates a bending moment in response to an electric potential when operated in a cantilever configuration. These actuators generate larger tip deflections of the actuator at low operating voltages. The fundamental advantage of these actuators compares to conventional bimorphs is their ability to withstand significantly greater electric field strengths. This aids to generate relatively greater strains and displacements.

A deflector jet hydraulic amplifier with mechanical feedback of the second stage spool was chosen for the PHSV design. The bimorph actuator was encapsulated for submerged operation. The limitations of the torque motor in this operating condition do not apply for the bimorph as they are independent of electric and magnetic fields. This novel approach considerably simplified the first stage assembly by reducing the part count and retaining the mechanical feedback of the second stage spool. Based on the operating principle of the valve, the analytical model of the PHSV can be developed and now will be discussed.

Chapter 3

Analytical modelling and simulation of the piezohydraulic valve

3.1 Introduction

This chapter presents the analytical modelling and simulation results of the PHSV. A steady state analytical model and a FEA model of the bimorph-feedback wire assembly is developed. The results of these models are compared to determine the assembly stiffness constants. The first stage flow force at the deflector is determined using CFD. The hysteretic characteristic of the bimorph is modelled and extended to the overall valve performance. A high order nonlinear analytical model for the valve is developed and simulated using Matlab Simulink. The nonlinear model is linearised to establish the most important parameters that influence the valve performance. The linearised model is subsequently reduced to determine the parameters that influence the bandwidth and the steady state gain of the valve.

3.2 Steady state analysis of the bimorph-feedback wire assembly

3.2.1 Analytical model of the bimorph tip deflection and slope

Figure 2.21 shows the multilayer configuration of a bimorph actuator. The two segments are comprised of identical multilayers. Therefore assuming the physical properties of the layers are consistent, the two segments can be simplified to two active layers of equal thickness. The thicknesses of the internal electrodes are assumed to be negligible relative to the layer thicknesses. The electrode configuration is simplified to one central electrode and two outer electrodes. This simplifies the multilayered bimorph to a conventional bimorph. The free deflection of the simplified bimorph is shown in Figure 3.1.

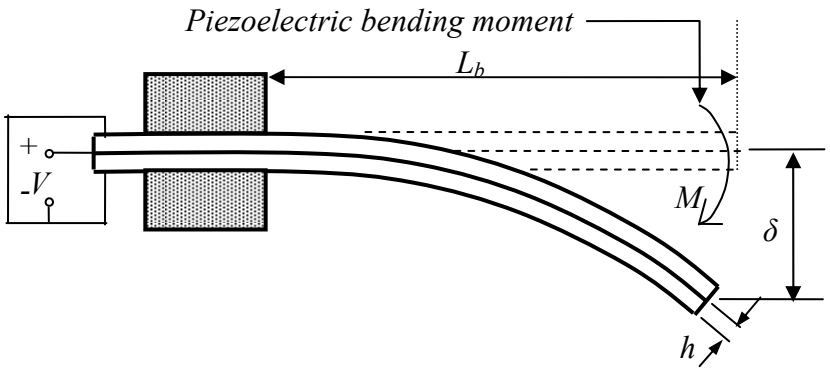

Figure 3.1: Free deflection of the bimorph actuator when subjected to an applied voltage V

The bimorph generates a constant bending moment, M, along its length, L_b, when subjected to constant voltage, V. When mounted in a cantilever arrangement, the actuator bends as shown in Figure 3.1. Assuming the actuator follows the Euler-Bernoulli-beam theory, the bending moment, M, is related to the curvature R by

$$\frac{1}{R} = \frac{M}{E_b I_b} \tag{1}$$

where, I_b is the second moment of area of the bimorph and E_b is the Young's modulus. Considering the bending due to the inverse piezoelectric effect; when subjected to an applied voltage V, the moment, M, when external forces are zero can be expressed as

$$M = Fh$$
$$M = \sigma b h^2 \tag{2}$$

where, F is the tensile blocking force acting on the bottom layer, σ is the stress in the top layer, h is the segment thickness and b is the width. The stress can be expressed in terms of electric field strength e, Young's modulus, E_b, and strain constant, d_{31}, by

$$\sigma = d_{31} e E_b \tag{3}$$

Substituting into Eq.(2) gives

$$M = d_{31} e E_b b h^2$$

(4)

The second moment of area, I_b, for a bimorph of total thickness $2h$ and width b is given by:

$$I_b = \frac{b(2h)^3}{12} = \frac{2bh^3}{3}$$

(5)

Substituting Eq.(4) and Eq.(5) into Eq.(1) and simplifying

$$R = \frac{2h}{3d_{31}e}$$

(6)

Figure 3.2 shows a deflected section of the bimorph actuator.

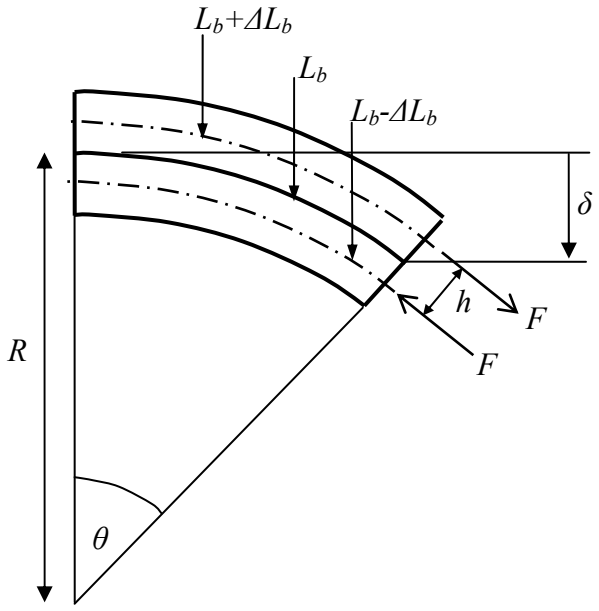

Figure 3.2 Section showing the deflection of the bimorph actuator

The deflection, δ, is related to the radius of curvature, R, and the slope, θ, by

$$\delta = R(1 - cos\theta) \tag{7}$$

Assuming angle θ to be small, the approximation $cos\theta \approx 1 - \frac{\theta^2}{2}$ can be used. Substituting for cosθ in Eq.(7)

$$\delta = \frac{R\theta^2}{2} \tag{8}$$

And

$$\theta = \frac{L_b}{R} \tag{9}$$

Substituting Eq.(9) into Eq. (8)

$$\delta = \frac{{L_b}^2}{2R} \tag{10}$$

Therefore the tip deflection δ can be obtained by substituting Eq. (6) into (10)

$$\delta = \frac{3{L_b}^2 d_{31} e}{4h} \tag{11}$$

The electric field strength, e, of a piezoelectric actuator is related to the applied voltage, V, and segment thickness, h, by:

$$e = \frac{V}{\frac{h}{n_l}} = \frac{n_l V}{h} \tag{12}$$

Where n_l is the number of layers in segment. Substituting to Eq.(11), the tip deflection of the bimorph actuator, δ, is

$$\delta = \frac{3{L_b}^2 d_{31} n_l V}{4h^2} \tag{13}$$

The slope of the bimorph actuator, θ, can be derived by substituting Eq.(6) into Eq. (9).

$$\theta = \frac{3 d_{31} e L_b}{2h} \tag{14}$$

Substituting for e, the slope of the actuator is

$$\theta = \frac{3 d_{31} L_b n_l V}{2h^2} \tag{15}$$

The flow to the first stage control ports is proportional to the deflector displacement. Having derived the free displacement and the slope of the bimorph, the steady state model for the deflector displacement can be developed.

3.2.2 Analytical model for the deflector displacement

Figure 3.3 shows the first stage assembly of the bimorph, deflector and the feedback wire. The force at the deflector is given by F_d and the force at the spool is given by F_s. The deflector and spool displacements are given by x_d and x_s, respectively. The bimorph length, L_b, feedback wire length, L_f and the deflector guide length, L_d are also shown in Figure 3.3.

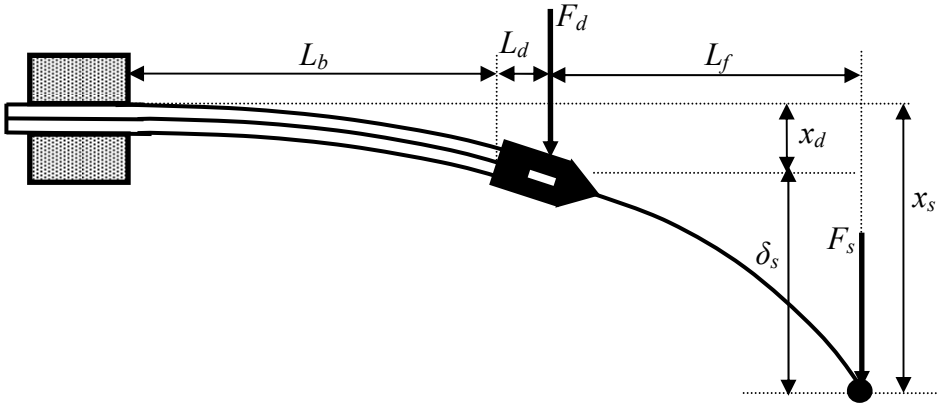

Figure 3.3: Schematic of the bimorph-feedback wire assembly

From Euler-Bernoulli-beam theory the tip deflection, δ, of a beam subjected to an end force, W, and moment, M, is given by

$$\delta = \frac{WL^3}{3EI} + \frac{ML^2}{2EI} \tag{16}$$

And the slope is given by

$$\theta = \frac{WL^2}{2EI} + \frac{ML}{EI} \tag{17}$$

The forces at the deflector and the spool, shown in Figure 3.3, create a moment at the bimorph tip. Therefore the moment at the bimorph tip can be given by

$$M = \left(L_d + L_f\right)F_s + L_d F_d \tag{18}$$

Assuming the bimorph behaves as a cantilever, Eq.(16) can be used to determine the tip deflection due to the forces F_s and F_d

$$\delta = (F_s + F_d)\frac{{L_b}^3}{3E_b I_b} + \left[\left(L_d + L_f\right)F_s + L_d F_d\right]\frac{{L_b}^2}{2E_b I_b} \tag{19}$$

Simplifying

$$\delta = \frac{{L_b}^2}{6E_bI_b}\left[2L_b(F_s + F_d) + 3F_s\left(L_d + L_f\right) + 3L_dF_d\right]$$

(20)

Similarly Eq.(17) can be used to determine the slope of the bimorph due to the forces F_s and F_d.

$$\theta = (F_s + F_d)\frac{{L_b}^2}{2E_bI_b} + \left[\left(L_d + L_f\right)F_s + L_dF_d\right]\frac{L_b}{E_bI_b}$$

(21)

Simplifying

$$\theta = \frac{L_b}{2E_bI_b}\left[L_b(F_s + F_d) + 2F_s\left(L_d + L_f\right) + 2L_dF_d\right]$$

(22)

Superimposing the piezoelectric deflection of the bimorph and the bimorph deflection due to external forces, the overall deflection can be obtained. In the steady state the forces at the deflector and the spool act in opposite direction to that generated by the bimorph. Therefore the overall tip deflection of the bimorph can be determined by superimposing Eq.(13) and Eq.(20)

$$\delta = \frac{3{L_b}^2d_{31}n_lV}{4h^2} - \frac{{L_b}^2}{6E_bI_b}\left[2L_b(F_s + F_d) + 3F_s\left(L_d + L_f\right) + 3L_dF_d\right]$$

(23)

Similarly the overall bimorph slope can be derived by superimposing Eq.(15) and Eq.(22)

$$\theta = \frac{3d_{31}L_bn_lV}{2h^2} - \frac{L_b}{2E_bI_b}\left[L_b(F_s + F_d) + 2F_s\left(L_d + L_f\right) + 2L_dF_d\right]$$

(24)

The bimorph deflector arrangement is shown in Figure 3.4.

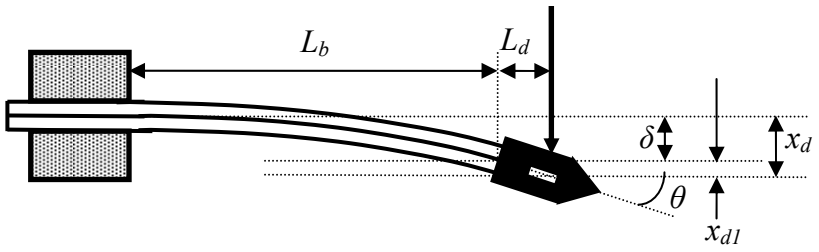

Figure 3.4: Bimorph and deflector arrangement

Assuming the deflector guide section of length L_d is significantly stiffer compared to the feedback wire and the bimorph, the total deflector displacement, x_d, is given by

$$x_d = \delta + x_{d1} \tag{25}$$

Displacement x_{d1} is expressed as

$$sin\theta = \frac{x_{d1}}{L_d} \tag{26}$$

Angle θ will be small. Therefore sinθ ≈ θ. Substituting into Eq.(26), displacement x_{d1} becomes

$$x_{d1} = \theta L_d \tag{27}$$

Substituting Eq.(27) into Eq.(25), the overall deflector displacement, x_d, is

$$x_d = \delta + \theta L_d \tag{28}$$

Substituting for δ and θ gives

$$x_d = \frac{3{L_b}^2 d_{31} n_l V}{4h^2} - \frac{{L_b}^2}{6E_b I_b}\left[2L_b(F_s + F_d) + 3F_s\left(L_d + L_f\right) + 3L_d F_d\right] + \frac{3d_{31} L_b L_d n_l V}{2h^2} - \frac{L_b L_d}{2E_b I_b}\left[L_b(F_s + F_d) + 2F_s\left(L_d + L_f\right) + 2L_d F_d\right]$$

(29)

Rearranging Eq.(29) in terms of V, F_s and F_d

$$x_d = (L_b + 2L_d)\frac{3L_b d_{31} n_l}{4h^2} V - \frac{L_b}{2E_b I_b}\left[\frac{2{L_b}^2}{3} + 2L_d L_b + 2{L_d}^2\right] F_d - \frac{L_b}{2E_b I_b}\left[\frac{2{L_b}^2}{3} + L_b(L_f + L_d) + 2L_d(L_d + L_f) + L_d L_b\right] F_s \tag{30}$$

Equation (30) can be expressed as

$$x_d = k_1 V - k_2 F_d - k_3 F_s \tag{31}$$

where k_1, k_2 and k_3 are constants given by

$$k_1 = (L_b + 2L_d)\frac{3L_b d_{31} n_l}{4h^2} \tag{32}$$

$$k_2 = \frac{L_b}{2E_b I_b}\left[\frac{2{L_b}^2}{3} + 2L_d L_b + 2{L_d}^2\right] \tag{33}$$

$$k_3 = \frac{L_b}{2E_b I_b}\left[\frac{2{L_b}^2}{3} + L_b(L_d + L_f) + 2L_d(L_d + L_f) + L_d L_b\right] \tag{34}$$

Equation (31) gives the steady state displacement of the deflector. Similarly, the displacement of the spool due to the bimorph and the external forces F_d and F_s can be derived.

3.2.3 Analytical model for the spool displacement

The spool displacement when the feedback wire section is subjected to an external force F_s is shown in Figure 3.5.

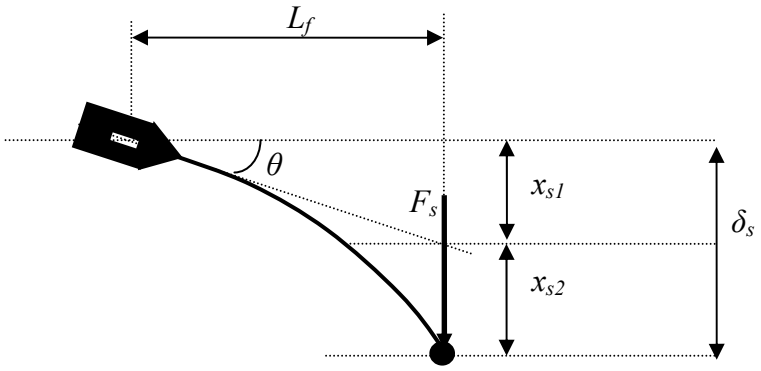

Figure 3.5: Feedback wire displacement when an external force F_s is applied

The deflection δ_s is the sum of displacements due to the bending of the wire and the angle θ. Therefore

$$\delta_s = x_{s1} + x_{s2} \tag{35}$$

where x_{s1} is the displacement due to the angle θ

$$x_{s1} = L_s sin\theta \tag{36}$$

Angle θ will be small. Therefore $\sin\theta \approx \theta$. Substituting to Eq.(36) gives

$$x_{s1} = \theta L_f \tag{37}$$

x_{s2} is the displacement due to the flexibility of the feedback wire. Assuming the feedback wire follows the Euler-Bernoulli-beam theory, the deflection can be expressed by Eq.(16). Therefore x_{s2} is

$$x_{s2} = \frac{F_s {L_f}^3}{3E_f I_f} \tag{38}$$

where E_f is the modulus of elasticity and I_f is the second moment of area of the feedback wire. Equation (35) can be expressed as

$$\delta_s = \theta L_f + \frac{F_s {L_f}^3}{3E_f I_f}$$

(39)

Figure 3.3 shows the overall spool displacement, x_s, in the bimorph-feedback wire assembly. Hence x_s can be expressed as

$$x_s = x_d + \theta L_f + \frac{F_s {L_f}^3}{3E_f I_f}$$

(40)

Substituting for x_d and θ in Eq.(40)

$$x_s = k_1 V - k_2 F_d - k_3 F_s + \left[\frac{3d_{31} L_b n_l V}{2h^2} - \frac{L_b}{2E_b I_b}\left[L_b(F_s + F_d) + 2F_s\left(L_d + L_f\right) + 2L_d F_d\right]\right] L_f + \frac{F_s {L_f}^3}{3E_f I_f}$$

(41)

Rearranging Eq.(41) in terms of V, F_s and F_d

$$x_s = \left[k_1 + \frac{3d_{31} n_l L_f L_b}{2h^2}\right] V - \left[k_2 + \frac{L_b L_f}{2E_b I_b}(L_b + 2L_d)\right] F_d - \left[K_3 + \frac{L_b L_f}{2E_b I_b}\left(L_b + 2\left(L_d + L_f\right)\right) + \frac{{L_f}^3}{3E_f I_f}\right] F_s$$

(42)

Equation (42) can be expressed as

$$x_s = n_1 V - n_2 F_d - n_3 F_s$$

(43)

where n_1, n_2 and n_3 are constants given by

$$n_1 = k_1 + \frac{3d_{31}n_l L_f L_b}{2h^2} \tag{44}$$

$$n_2 = k_2 + \frac{L_b L_f}{2E_b I_b}(L_b + 2L_d) \tag{45}$$

$$n_3 = k_3 + \frac{L_b L_f}{2E_b I_b}\left(L_b + 2\left(L_d + L_f\right)\right) + \frac{{L_f}^3}{3E_f I_f} \tag{46}$$

Equation (43) gives the steady state displacement of the spool. It is now possible to determine the forces F_d and F_s in terms of the displacements x_d and x_s and the bimorph applied voltage, V. This will convert the constants in Eq.(31) and Eq.(43) into stiffness constants. The derivation of these constants will be considered next.

3.2.4 Derivation of the stiffness constants

Equations (31) and (43) are repeated below.

$$x_d = k_1 V - k_2 F_d - k_3 F_s \tag{31}$$

$$x_s = n_1 V - n_2 F_d - n_3 F_s \tag{43}$$

Rearranging Eq.(43) for F_s

$$F_s = \frac{n_1}{n_3} V - \frac{n_2}{n_3} F_d - \frac{1}{n_3} x_s \tag{47}$$

Substituting Eq.(47) into Eq.(31)

$$x_d = k_1 V - k_2 F_d - k_3 \left(\frac{n_1}{n_3} V - \frac{n_2}{n_3} F_d - \frac{1}{n_3} x_s\right) \tag{48}$$

Rearranging for F_d

$$F_d = \frac{k_1 n_3 - k_3 n_1}{k_2 n_3 - k_3 n_2} V - \frac{n_3}{k_2 n_3 - k_3 n_2} x_d + \frac{k_3}{k_2 n_3 - k_3 n_2} x_s \tag{49}$$

F_d can be expressed as

$$F_d = k_4 V - k_5 x_d + k_6 x_s \tag{50}$$

where k_4, k_5 and k_6 are stiffness constants relating to V, x_d and x_s, respectively. They are given by

$$k_4 = \frac{k_1 n_3 - k_3 n_1}{k_2 n_3 - k_3 n_2} \tag{51}$$

$$k_5 = \frac{n_3}{k_2 n_3 - k_3 n_2} \tag{52}$$

$$k_6 = \frac{k_3}{k_2 n_3 - k_3 n_2} \tag{53}$$

Similarly, F_s can be expressed in terms of stiffness constants. Substituting Eq.(50) into Eq.(47) gives

$$F_s = \frac{n_1}{n_3} V - \frac{n_2}{n_3} (k_4 V - k_5 x_d + k_6 x_s) - \frac{1}{n_3} x_s \tag{54}$$

Rearranging gives

$$F_s = \frac{n_1 - n_2 k_4}{n_3} V + \frac{n_2 k_5}{n_3} x_d - \frac{n_2 k_6 + 1}{n_3} x_s \tag{55}$$

F_s can be expressed as

$$F_s = n_4 V + n_5 x_d - n_6 x_s \tag{56}$$

where n_4, n_5 and n_6 are stiffness constants relating to applied voltage, V, deflector displacement, x_d and spool displacement, x_s, respectively. They are given by

$$n_4 = \frac{n_1 - n_2 k_4}{n_3} \tag{57}$$

$$n_5 = \frac{n_2 k_5}{n_3} \tag{58}$$

$$n_6 = \frac{n_2 k_6 + 1}{n_3} \tag{59}$$

To compare the steady state stiffness constants that have been analytically derived, a FEA model of the bimorph-feedback wire assembly is developed. The modelling and analysis of the FEA model is considered next.

3.3 FEA analysis of the bimorph-feedback wire assembly

The bimorph actuator generates a constant bending moment along its length when a voltage is applied. The multilayered bimorph actuator was modelled as a simple cantilever in FEA. For a simple cantilever a constant bending moment along its length is generated by applying a constant moment at its free end. The constant bending moment generated by the bimorph actuator can be calculated using Eq.(4), as a function of voltage. The calculated moment can then be applied as bending moment at the bimorph free end in FEA. The assembly is shown in Figure 3.6. To validate the assumption made for the FEA model the deflector displacement predicted by FEA was compared to experiment measurements. This is shown in Figure 3.7.

An optical sensor of 1μm resolution was used to measure the deflector displacement for varying voltages. The corresponding moments were calculated using Eq.(4) and used in the FEA simulations to predict the deflector displacement. The experiment results show good agreement. Therefore modelling the bimorph as a simple cantilever with a constant bending moment at the tip is a reasonable assumption.

In Figure 3.6 feedback wire ball is unconstrained. A moment of 16.3Nmm was applied at the bimorph tip. This corresponds to an applied voltage of 30V for the PL127.10 bimorph described in chapter 2.

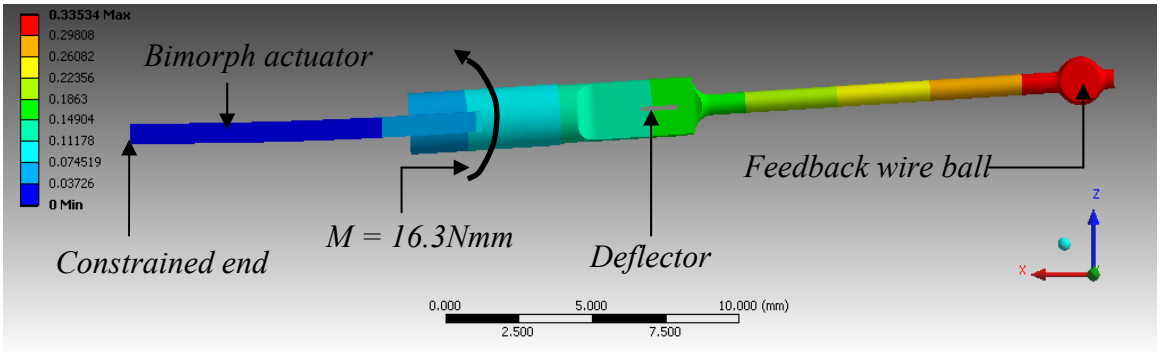

Figure 3.6: FEA model of the bimorph-feedback wire assembly

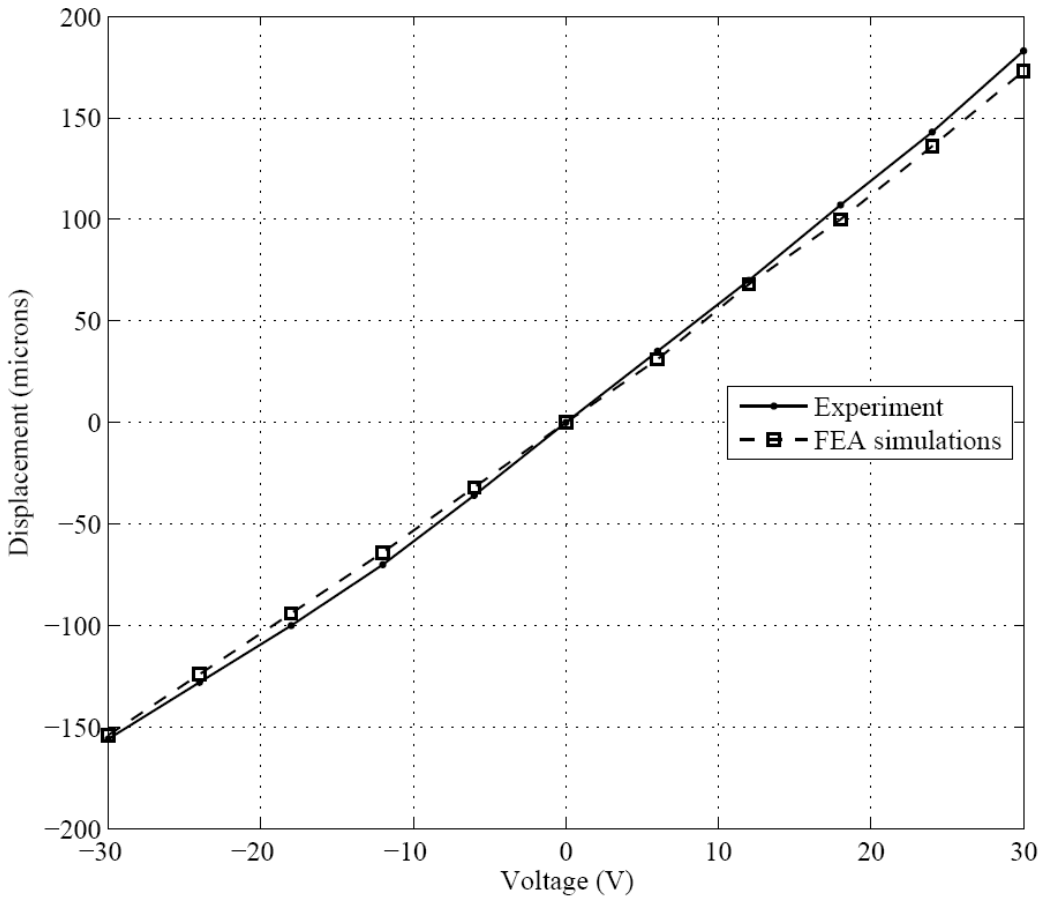

Figure 3.7: Deflector stroke comparison between FEA and experimental results

The FEA model can now be used to predict the deflector and spool displacement for discrete inputs of V, F_s and F_d. The analytical model can then be used to predict these displacements using the stiffness constants. The parameters used to derive the analytical model are given in Table 3-1. Table 3-2 shows the FEA and the analytical model results. d_{31} and E_b were obtained from the PI catalogue [72]. E_f was obtained from Moog. All other parameters were measured.

Parameter	*Value*	*Units*
d_{31}	2.23×10^{-10}	*C/N*
n_l	*13*	
h	3.25×10^{-4}	*m*
E_b	60×10^{9}	N/m^2
I_b	2.197×10^{-13}	m^4
L_b	12×10^{-3}	*m*
L_d	6×10^{-3}	*m*
L_f	12.85×10^{-3}	*m*
E_f	180×10^{9}	N/m^2
I_f	1.0496×10^{-14}	m^4

Table 3-1: Parameters used in the analytical model

Demand	*Spool displacement, x_s (mm)*			*Deflector displacement, x_d (mm)*		
	FEA	*Analytical*		*FEA*	*Analytical*	
		Parameter			*Parameter*	
Voltage (30V)	*0.316*	n_1V	*0.368*	*0.16*	k_1V	*0.177*
Deflector (1N)	*0.26*	n_2	*0.282*	*0.13*	k_2	*0.142*
Spool (1N)	*0.96*	n_3	*0.947*	*0.28*	k_3	*0.284*

Table 3-2: Comparison of analytical predictions to FEA results

The difference in displacements predicted using the analytical model and FEA are approximately 5% or less. Discrepancies in the results are expected due to the approximations of the models. Nevertheless, the results are sufficiently close. Therefore, the derived stiffness constants from the analytical model can be used to develop the nonlinear dynamic model of the valve.

3.4 Nonlinear dynamic model

3.4.1 First stage dynamics

The steady state model of the first stage force-displacement relationship was given by Eq.(50). Using a lumped parameter model, the first stage dynamics can be modelled as:

$$m_d \frac{d^2 x_d}{dt^2} + c_d \frac{dx_d}{dt} = F_d - F_f \tag{60}$$

where m_d is the effective mass at the deflector, c_d is the deflector damping coefficient and F_f is the flow force. F_d is given by Eq.(50).

The flow force, F_f, is influenced by the deflector displacement, supply pressure, the taper in the deflector and the spread angle of the jet in the deflector [70]. The spread angle defines the velocity profile of the flow in the deflector slot and the area of contact [70]. Due to the complexity of the flow profile at the deflector, CFD was chosen to predict the first stage flow forces.

3.4.1.1 CFD analysis of the first stage flow force

A model of the first stage flow profile of the 26series valve was developed in CFD. The main components that define the flow at the first stage are the amplifier, deflector, amplifier top and the amplifier base, shown in Figure 3.8. Thus the control volumes for the first stage flow model were generated from the engineering drawings of these components. The individual flow paths within these components were

merged together to form the complete flow model. The flow model for the first stage is shown in Figure 3.8.

Figure 3.8 represents a looped receiver port configuration. This configuration emulates the second stage of the valve, however not taking into account the presence of the spool. Therefore this configuration assumes an ideal valve with no leakage or frictional losses and the work done to move the spool to be negligible. These factors are considered to be of a low significance to the flow dynamics that are under investigation at the first stage.

Figure 3.9 shows the first stage hydraulic amplifier flow model. The cut away feature that can be observed in the middle of the amplifier represents the deflector. The flow profile within the deflector is also shown.

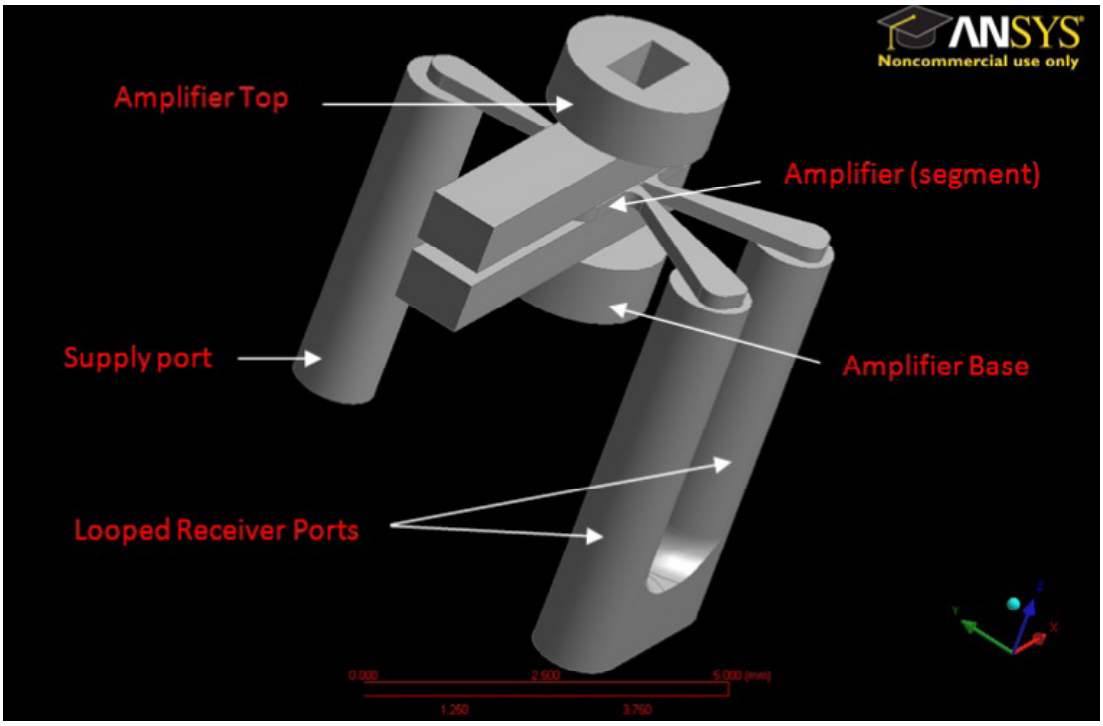

Figure 3.8: Deflector jet first stage flow model

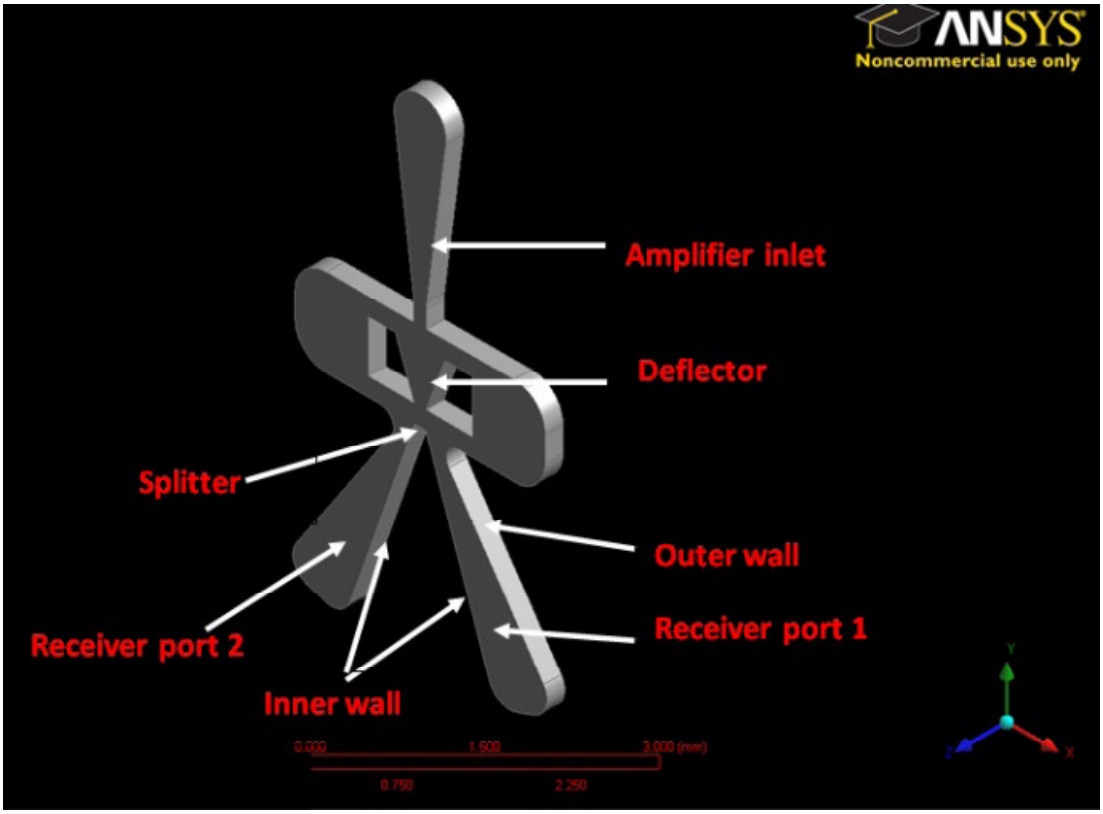

Figure 3.9: First stage hydraulic amplifier

Ansys CFX mesh generator was used to mesh the completed flow model. A custom mesh was developed to concentrate more nodes at critical flow regimes such as the flow through the amplifier, deflector and receiver ports. The mesh was sized to ensure that there were sufficient nodes at the smallest cross-section of the flow regime. Mesh adaptation techniques were used to size the neighbouring elements to ensure the aspect ratio is kept to minimum and skewing of elements is avoided. The mesh density of the regions in the vicinity of the deflector was also increased to facilitate a moving boundary domain. The increased mesh density prevents the skewing of elements when the mesh deforms as the deflector moves. The mesh information is shown in Table 3-3.

Number of nodes	*276577*
Number of elements	*952321*
Number of tetrahedra elements	*679706*
Number of wedge elements	*270735*
Number of pyramid elements	*1880*

Table 3-3: CFD mesh information

Figure 3.10 shows the mesh across the smallest cross-section of the flow model. More than ten nodes can be observed across the region at which the primary jet is formed. If a variable is averaged across this cross-section the value will be generated from the nodes spread across the cross-section. Since the average is generated from more than ten nodes, the value is expected to be a good representation of the transient values at the cross-section. The results were found to be consistent for different meshes (with increased nodes) across this section. Therefore increasing the mesh density any further will have no influence on the results and will increase computation time. Inflation layers can be observed near the walls in Figure 3.10. This captures the flow dynamics near the wall and improves solver convergence.

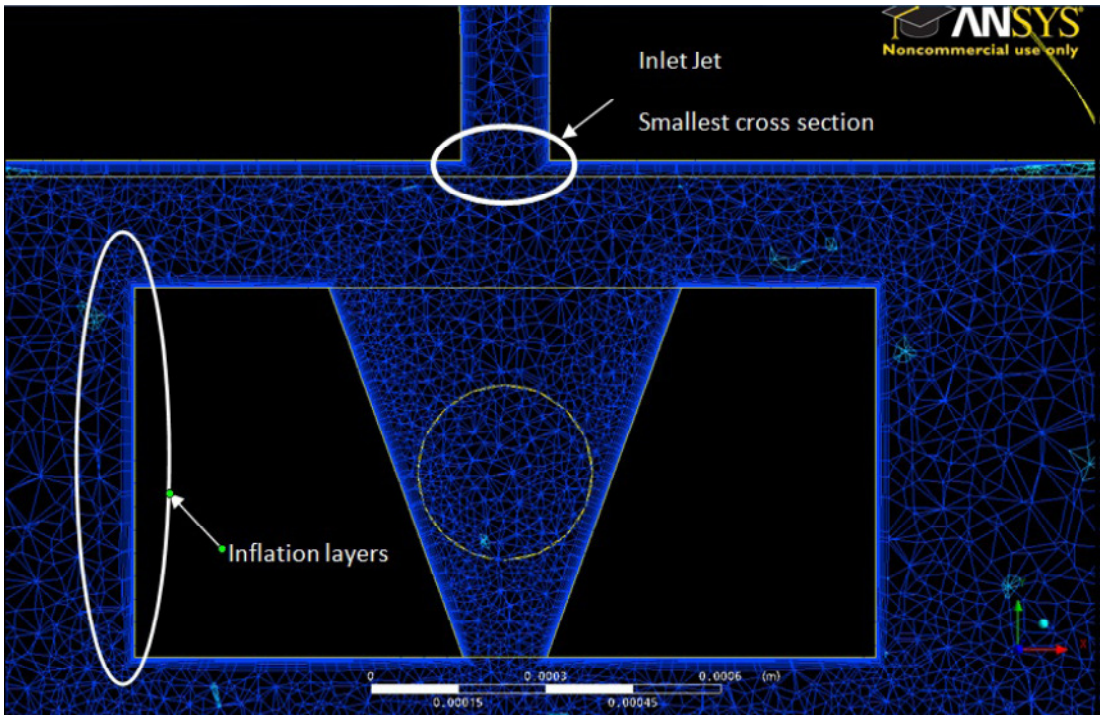

Figure 3.10: Deflector jet amplifier mesh

To validate the model and the modelling technique, the flow recovery (net flow into the control port as a ratio of supply flow) in the first stage control ports were compared to existing experiment results of the 26series valve first stage [70]. This is shown in Figure 3.11. The flow recovery in the control port is expressed as a percentage of the total first stage flow. The fluid used for testing was phosphate ester.

A k-epsilon turbulence model was chosen for the simulations. The simulation type was configured to steady-state and the fluid transport properties were changed to that of phosphate ester. Multi-phase simulations were switched on to take flow cavitations into account. The boundary conditions were set as a mass flow rate at the inlet and a pressure at the outlet. The mass flow rates at the inlet were derived from experimental results[70] for the specific supply and return pressure configuration. The discretization technique of using a mass flow rate at the inlet and a pressure at the outlet makes the solver more robust and aids convergence. High intensity turbulent option was chosen at the inlets. The gauge pressure at the outlet was set as an average over the whole outlet. The initialization parameters are shown in Table 3-4. For subsequent simulations the simulations runs were initialised using the previous run results.

Fluid density	*1004kgm^{-3}*
Dynamic viscosity	*0.01kgm^{-1}s^{-1}*
Velocity	*6.5ms^{-1}*
Relative static pressure	*500psi*
Turbulent kinetic energy	*0.0001m^{2}s^{-2}*
Turbulent eddy dissipation	*0.0001m^{2}s^{-3}*
Phosphate ester volume fraction	*1*
Phosphate ester vapour volume fraction	*0*

Table 3-4: CFD initialization values

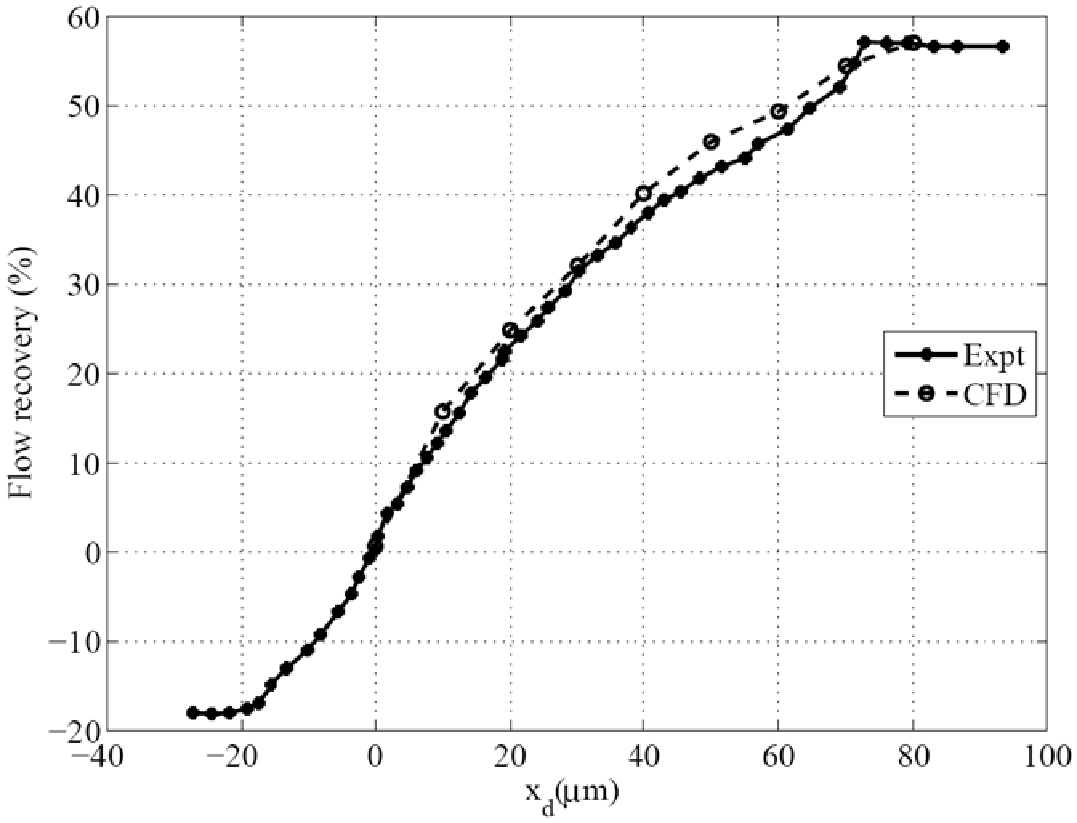

Figure 3.11: Validation of CFD modelling using existing experimental data

The predictions of flow recovery by CFD simulations are in good agreement with the experiment results. The modelling technique and the boundary conditions used for the CFD simulations are sufficiently accurate to predict the first stage flow dynamics. Therefore the model can be used to predict the net flow force at the deflector as a function of deflector displacement. Figure 3.12 shows the impingement of the flow in the deflector wall at maximum deflector displacement. The information in Figure 3.12 is limited due to commercial sensitivity.

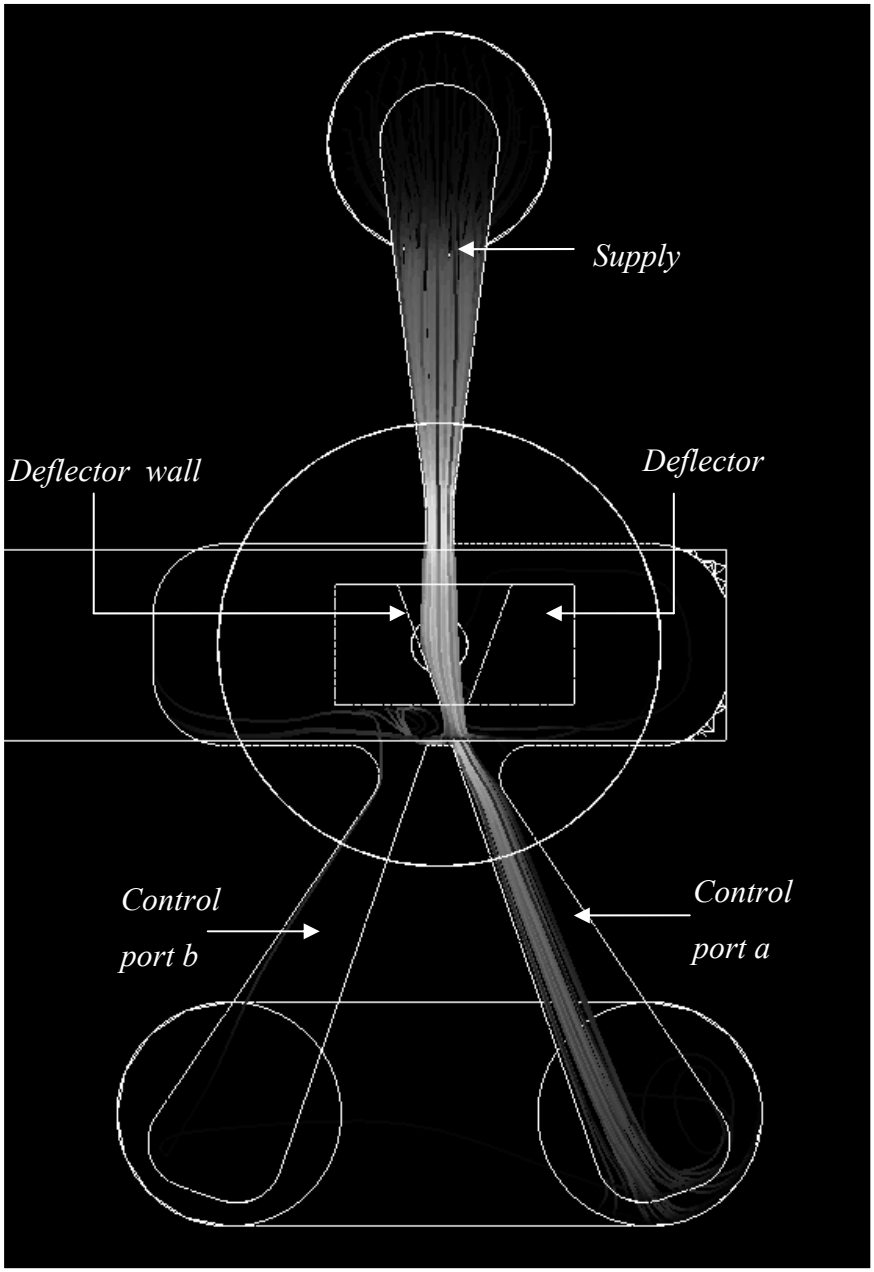

Figure 3.12: CFD simulation showing the flow dynamics at the first stage at maximum deflector displacement and 140bar supply pressure

The change in momentum of the flow at the deflector wall generates a net force in the direction opposite to the deflector displacement. This force can be extracted from the simulation results. Figure 3.13 shows the flow force generated at the deflector with respect to the deflector position at 280bar, 140bar and 70bar supply pressures. The return pressure is kept constant at 7bar.

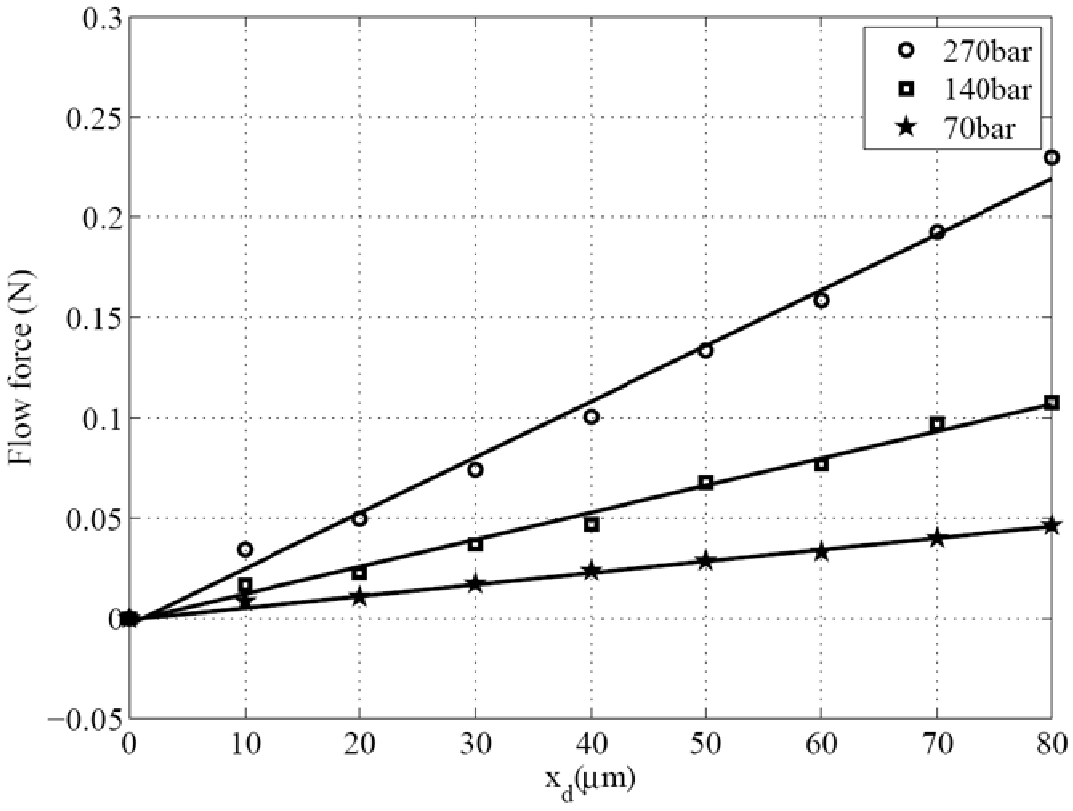

Figure 3.13: First stage flow force at 270bar, 140bar and 70bar supply pressures

Flow force is proportional to the deflector displacement. Therefore F_f can be expressed as

$$F_f = K_{ff} x_d \tag{61}$$

where, K_{ff} is the flow force per deflector displacement (flow force stiffness). The gradient of the flow force-displacement plot increases linearly with the pressure drop across the deflector. This implies that the flow force is proportional to the pressure drop across the deflector. Assuming the return pressure is negligible relative to the supply, it can be assumed that the flow force is proportional to the supply pressure P_s. Hence the first stage flow stiffness, K_{ff}, can be defined in terms of the supply pressure P_s. K_{ff} can be approximated to

$$K_{ff} = 10.5 P_s \tag{62}$$

with K_{ff} in N/m and P_s in bar.

Having defined the flow force, the first stage dynamics of the PHSV can be developed. Equation (60) can be expressed as

$$m_d \frac{d^2 x_d}{dt^2} + c_d \frac{dx_d}{dt} = F_d - K_{ff} x_d \tag{63}$$

Equation (63) represents a linear description of the bimorph actuator. A hysteresis model is required to predict the hysteretic characteristic of the bimorph and its influence on the overall valve performance.

3.4.1.2 Hysteresis model for the bimorph actuator

Many studies have modelled the hysteresis nonlinearity of piezoelectric actuators, such as the Preisach model [73], the Duhem model [74], the Maxwell slip model [75] and the Bouc-Wen model [76]. Due to the simplicity of the Bouc-Wen model to implement, this model will be used.

The Bouc-Wen model uses a nonlinear differential equation to describe the hysteresis of a piezoelectric actuator [77]. The Bouc-Wen model is mostly used in an inverse approach to fine tune the modelling parameters to match a set of experimental results. When a good approximation is obtained the resulting model is considered to be sufficient, from a practical point of view, to determine the hysteresis at all operating points [76]. The non linear differential equation of the model is given by [77]:

$$\dot{n} = \alpha d_v \dot{V} - \beta \left|\dot{V}\right| n - \gamma \dot{V} |n| \tag{64}$$

where $\dot{n}$ is the derivative of the hysteretic nonlinear term, d_v is the ratio of displacement against applied voltage V, $\dot{V}$ is the derivative of the applied voltage and α, β, and γ are the tuning parameters which determine the hysteretic loop's magnitude and shape. The lumped parameter hysteretic model of PL127.10 can be represented by

$$m_b \frac{d^2\delta}{dt^2} + c_b \frac{d\delta}{dt} + K_b\delta = K_b(d_v V - n) \tag{65}$$

where m_b is the effective mass of the actuator, c_b is the actuator damping coefficient and K_b is the actuator stiffness.

The PL127.10 actuator was clamped in cantilever configuration with a free length of 24.5mm. The tip displacement of the bimorph was measured using an optical sensor. Figure 3.14 compares the simulated results of the Bouc-Wen model to the experimental results. Figure 3.14 shows that the Bouc-Wen model can be tuned to represent the experiment results with good accuracy. The values of the modelling parameters used to match the experiment data are shown in Table 3-5.

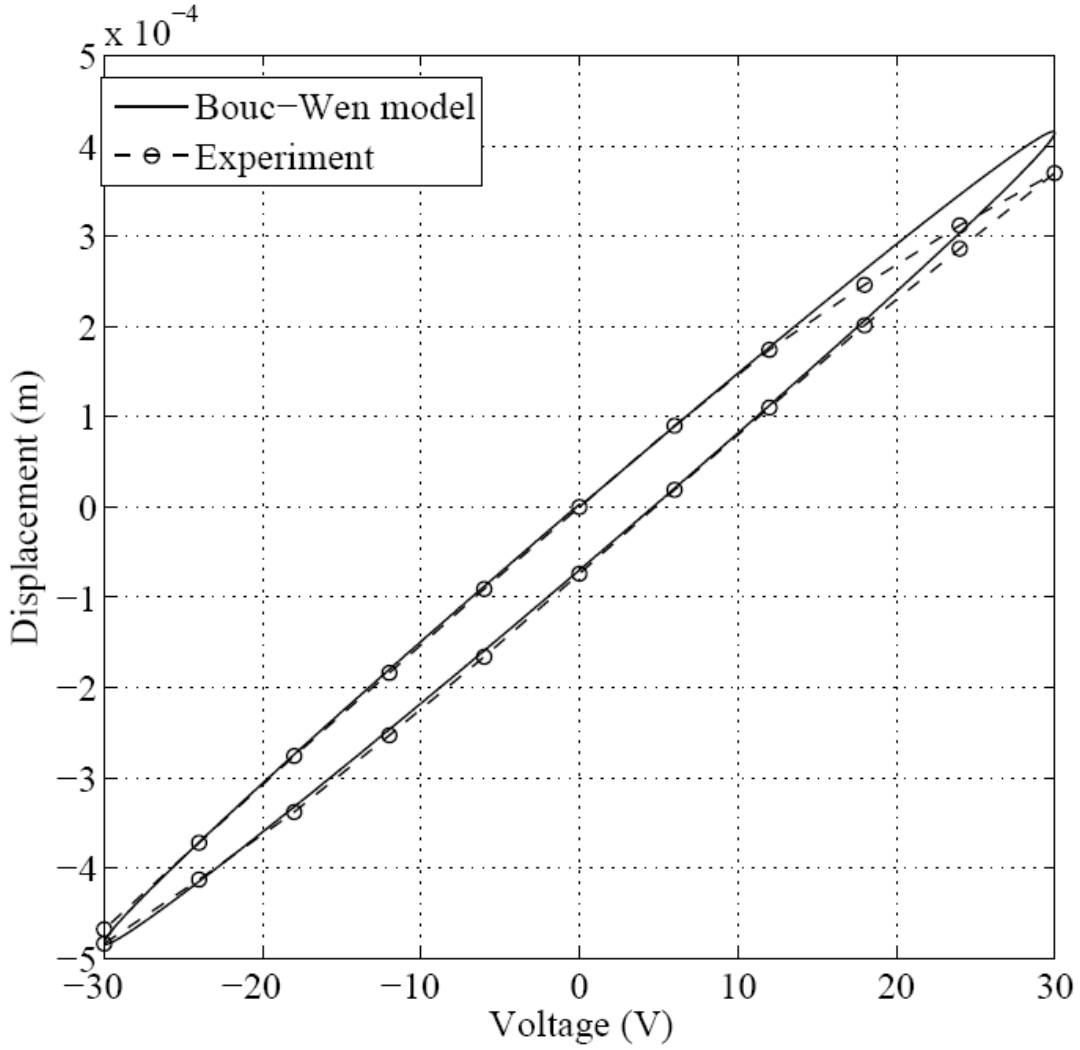

Figure 3.14: Comparison of Bouc-Wen model to experiment results

.

α	β	γ
0.6	*0.0009*	*0.0012*

Table 3-5: The Bouc-Wen model parameters

Having developed a satisfactory hysteresis model for the bimorph actuator, the model can now be modified and applied to the deflector. The effective stiffness at the deflector can be obtained from Eq.(31). Setting V and F_s to zero, the effective stiffness can be expressed as $\frac{1}{k_2}$. In addition, the d_v term in Eq.(64) will be the ratio between the deflector displacement and the applied voltage. Hence Eq.(60) becomes

$$m_d \frac{d^2 x_d}{dt^2} + c_d \frac{dx_d}{dt} = F_d - K_{ff} x_d - \frac{1}{k_2} n \tag{66}$$

The first stage control flows can now be derived.

3.4.2 First stage flows

Figure 2.31 shows the fluid flow paths at the first stage control ports. The pressure recovery in the control ports, due to the incoming jet, generates a pressure drop between the control port and the return. This pressure drop drives a flow of fluid out from the control port (see Figure 2.31). The pressure difference between the two control ports moves the second stage spool. Typically, the first stage flow paths at the control ports are modelled as orifices [48], [78]. Assuming negligible pressure drop of the flow upstream to the control ports, the first stage flows can be modelled as shown in Figure 3.15. The following adopts the modelling approach proposed in [78].

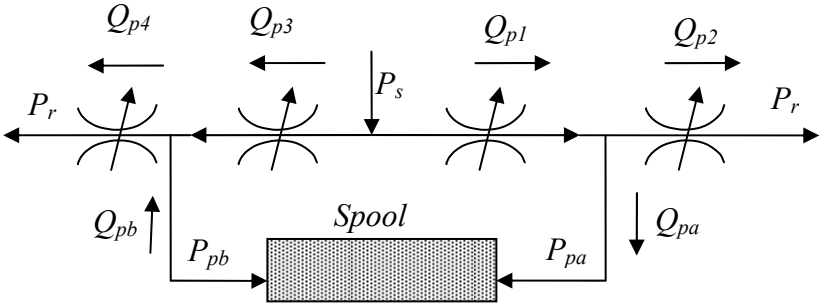

Figure 3.15: First stage flow model of the valve

With reference to Figure 2.31 and Figure 3.15 the first stage flow model can be developed. Flow into 'control port a' is given by

$$Q_{p1} = c_{df} d(x_0 + x_d) \sqrt{\frac{2}{\rho}(P_s - P_{pa})}$$

(67)

where Q_{p1} is the flow into 'control port a', c_{df} is the discharge coefficient, x_0 is the initial inlet flow width, ρ is the fluid density, P_s is the supply pressure and P_{pa} is the pressure in 'control port a'. The initial flow width can be expressed as

$$x_0 = \frac{J_w - S_w}{2}$$

(68)

where J_w is the jet width and S_w is the slot width. These parameters are shown in Figure 2.31. The flow out of 'control port a' is given by

$$Q_{p2} = c_{df} d[(R_w - x_0) - x_d] \sqrt{\frac{2}{\rho}(P_{pa} - P_r)}$$

(69)

where, R_w is the effective control port width and P_r is the flow return pressure. Hence the total flow through 'control port a' is

$$Q_{pa} = Q_{p1} - Q_{p2}$$

(70)

Similarly, the flow into 'control port b' can be given by

$$Q_{p3} = c_{df} d(x_0 - x_d) \sqrt{\frac{2}{\rho}(P_s - P_{pb})}$$

(71)

where, P_{pb} is the pressure in 'control port b'. The flow out of the control port is given by

$$Q_{p4} = c_{df} d[(R_w - x_0) + x_d] \sqrt{\frac{2}{\rho}(P_{pb} - P_r)}$$

(72)

Hence the total flow through 'control port b' is

$$Q_{pb} = Q_{p4} - Q_{p3}$$

(73)

The continuity equation for one dimensional flow can be applied to the flow volumes in the control ports. Defining the spool reference axis in the opposite direction to that of the deflector will provide a positive spool displacement for a positive deflector displacement in the steady state. Therefore applying the continuity equation in terms of the pressure derivative in 'control port a' gives

$$P_{pa} = \int \frac{\beta_f}{V_{pa}}(Q_{pa} - A_s \dot{x}_s) dt$$

(74)

where β_f is the fluid bulk modulus, V_{pa} is the flow volume in 'control port a', A_s is the spool cross sectional area and $\dot{x}_s$ is the spool velocity. Similarly, applying continuity in terms of pressure derivative in 'control port b' gives

$$P_{pb} = \int \frac{\beta_f}{V_{pb}}(A_s \dot{x}_s - Q_{pb}) dt$$

(75)

where, V_{pb} is the flow volume in 'control port b'. Having derived the first stage flows the dynamics of the second stage spool can be developed.

3.4.3 Second stage dynamics

Applying the equation of motion at the second stage spool gives

$$m_s \frac{d^2 x_s}{dt^2} + c_s \frac{dx_s}{dt} = A_s(P_{pa} - P_{pb}) - F_s - F_{fs}$$

(76)

where, m_s is the mass of the spool, c_s is the spool damping coefficient and F_{fs} is the flow force at the spool. F_s is given by Eq. (56). The flow force at the spool can be modelled as [12]

$$F_{fs} = 2c_{sf}S_{fw}x_s cos\varphi \Delta P \tag{77}$$

where c_{sf} is the spool flow port discharge coefficient, S_{fw} is the spool flow port width, φ is the flow angle and ΔP is the pressure drop across the flow port.

3.5 Bimorph amplifier response

An ideal bimorph amplifier will amplify the demand voltage by its gain and does not influence the bimorph dynamics. However, in reality, slew rate limitations of the amplifier introduce delay in the amplifier response. A low cost amplifier (E-650 LVPZT Amplifier) manufactured by PI was chosen. The measured response of the bimorph amplifier to a 30 to 15V step input is shown in Figure 3.16. Although other functions such as a slew rate limit or 2nd order response could be used to better represent the amplifier response, the best match in the overall valve response between simulation and experiment was obtained by using a simple delay of 2ms.

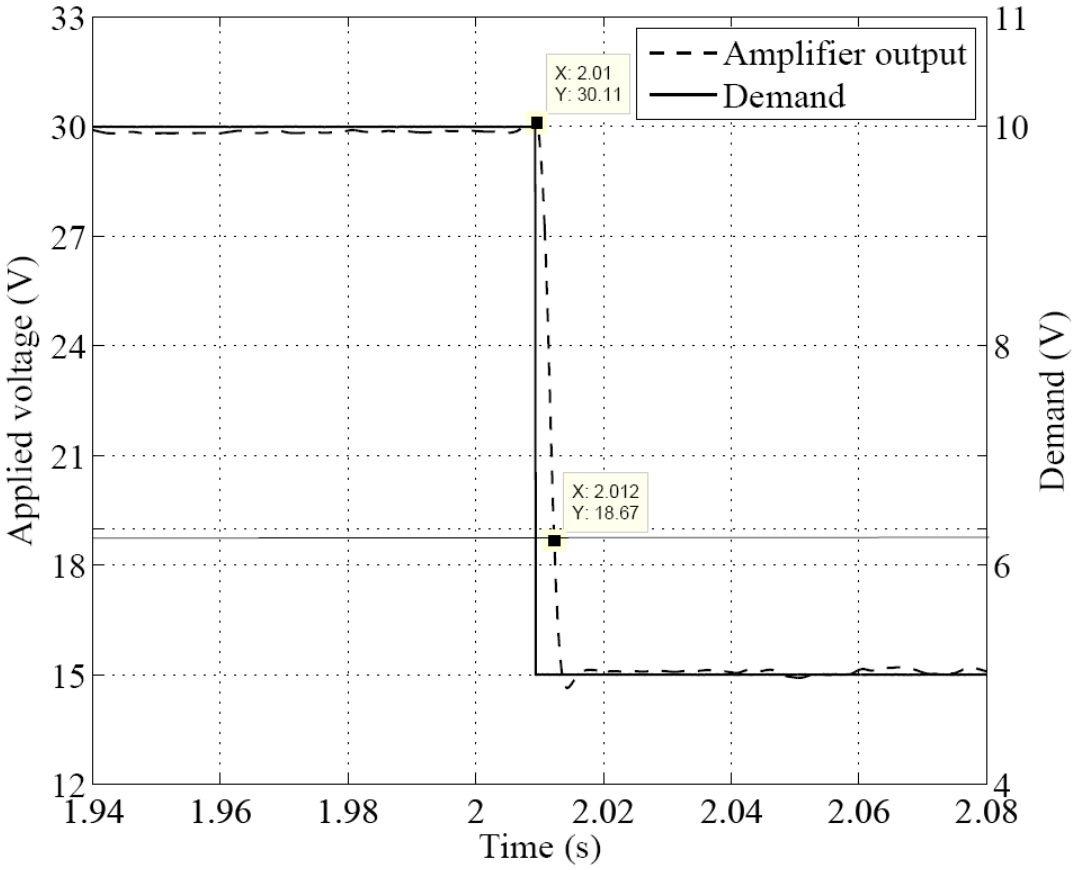

Figure 3.16: Bimorph amplifier step response at 5V demand

The flow through the valve spool is proportional to the spool position x_s and governed by the orifice equation [79]. The spool flow and the hydraulic actuator for the simulations were modelled as described in [80]. The flow force is not thought to have a significant effect on spool position, so the spool flow and actuation models do not effect the results very much. The complete model was simulated using Matlab Simulink. The amplifier lag was included as a time delay in the model. The valve parameters are given in Table 3-6, in addition to the bimorph-feedback wire assembly parameters in Table 3-1. The simulation results are presented next.

Parameter	*Value*	*Units*
m_d	7.74×10^{-4}	*Kg*
c_{df}	*0.78*	-
c_d	*1*	-
ρ	*1004*	kgm^{-3}
d	0.21×10^{-3}	*m*
J_w	0.14×10^{-3}	*m*
S_w	0.1×10^{-3}	*m*
R_w	0.18×10^{-3}	*m*
P_r	*5*	*bar*
β	0.7×10^{9}	Nm^{-2}
V_{pa}	3.46×10^{-7}	m^3
V_{pb}	3.46×10^{-7}	m^3
A_s	3.43×10^{-5}	m^2
m_s	4.4×10^{-3}	*kg*
c_s	*5*	-
c_{sf}	*0.75*	-
Sfw	*2.24×10-3*	*m*
cosφ	*69*	*o*

Table 3-6: Valve parameters

3.6 Simulation of the nonlinear dynamic model

The dynamic response of the PHSV was predicted using Simulink. The top level nonlinear Simulink block diagram is shown in Figure 3.17. A 'chirp' signal was used to generate a swept frequency demand. A frequency response for the nonlinear system was estimated using Welch's averaged periodogram method. The system input and output were the applied voltage to the bimorph actuator and the spool position, respectively. Figure 3.18 shows the frequency response plot for the valve at 140bar, 100bar and 70bar supply pressures, with a 30V amplitude chirp signal.

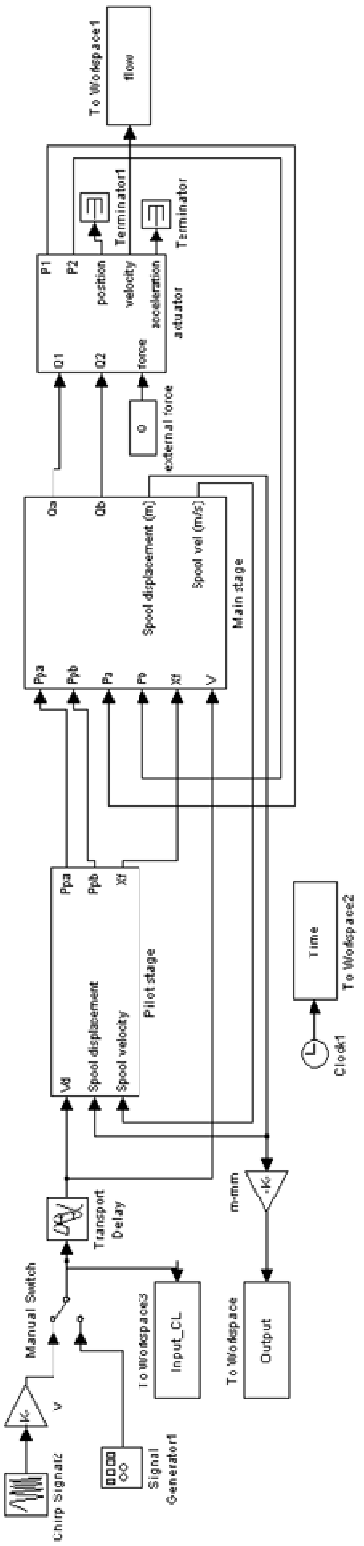

Figure 3.17: Top level nonlinear Simulink block diagram

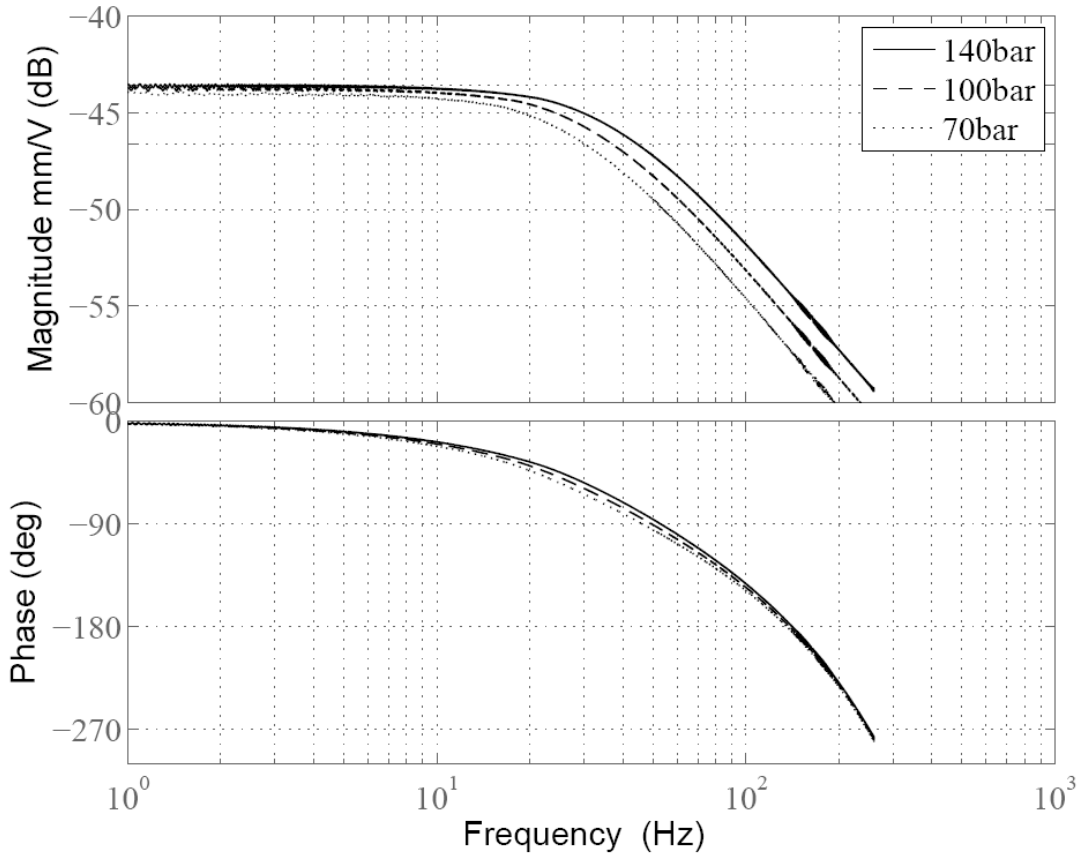

Figure 3.18: Simulated frequency response data for the nonlinear valve model at 30V amplitude applied voltage

The -3dB bandwidth of the valve at 140bar supply pressure is approximately 40Hz and the -90 degrees phase frequency is at approximately 50Hz. At 100bar supply pressure, the -3dB bandwidth is at approximately 35Hz and the -90 degrees phase frequency is at approximately 48Hz. At 70bar supply pressure, the -3dB bandwidth and -90degrees phase frequency drop to approximately 28Hz and 45Hz, respectively. The bandwidth increases with the pressure drop across the valve. The slopes of the bode plots in Figure 3.18 are -20dB/decade. This would imply that the -3dB bandwidth of the valve is determined by a single pole, which determines the first break frequency of the frequency response plot.

The low frequency line of the bode plot in Figure 3.18 is at approximately -43.6dB, where the magnitude is given in mm/V. Thus the low frequency is 6.6×10^{-3}mm/V. Therefore at 30V applied voltage, the amplitude of the spool displacement is approximately 0.2mm.

The influence of applied voltage on the frequency response is shown in Figure 3.19. The model was simulated at 30V and 3V applied voltage amplitudes. The supply pressure was kept constant at 140bar supply pressure. At 3V applied voltage the -3dB bandwidth of the valve spool increases to approximately 52Hz. This increase in response with reducing voltage is small compared to the conventional servovalve responses. This implies that the nonlinearities at the first stage do not influence the PHSV response as much. The phase response is reasonably similar for the two operating points.

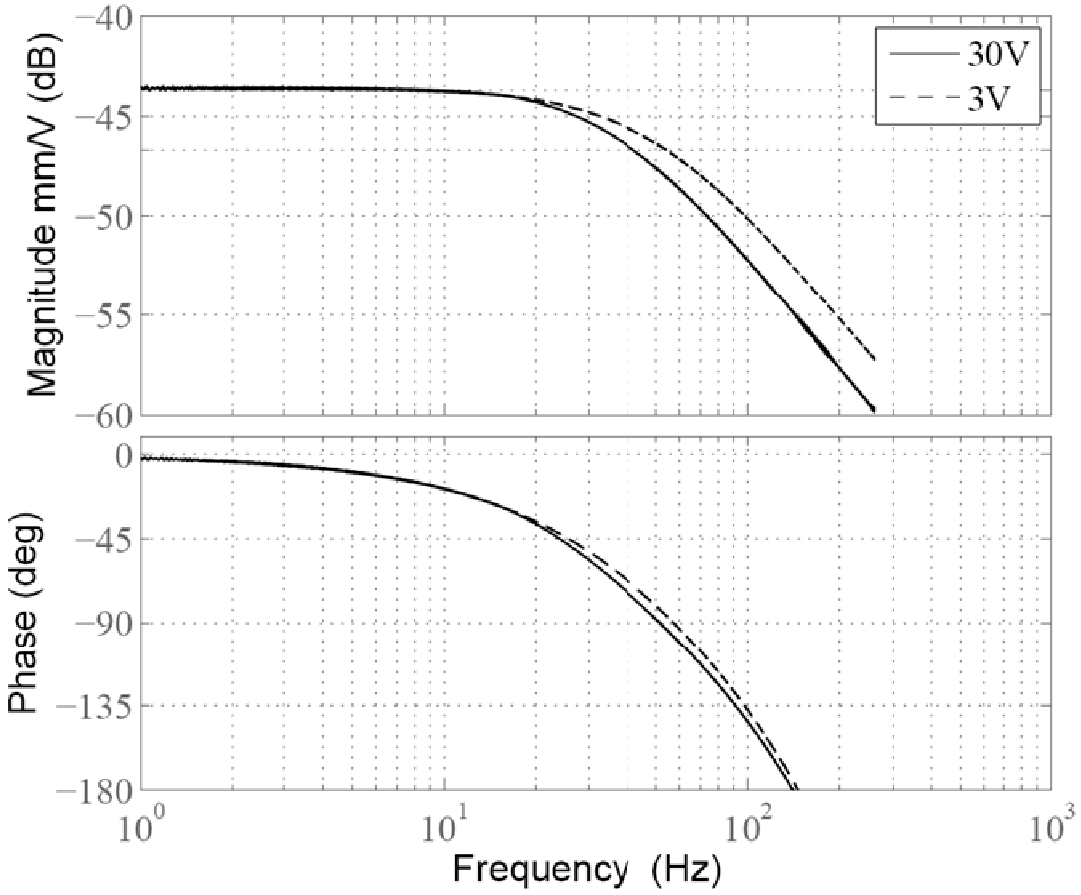

Figure 3.19: Simulated frequency response of the valve spool at varying operating voltage at 140bar supply pressure

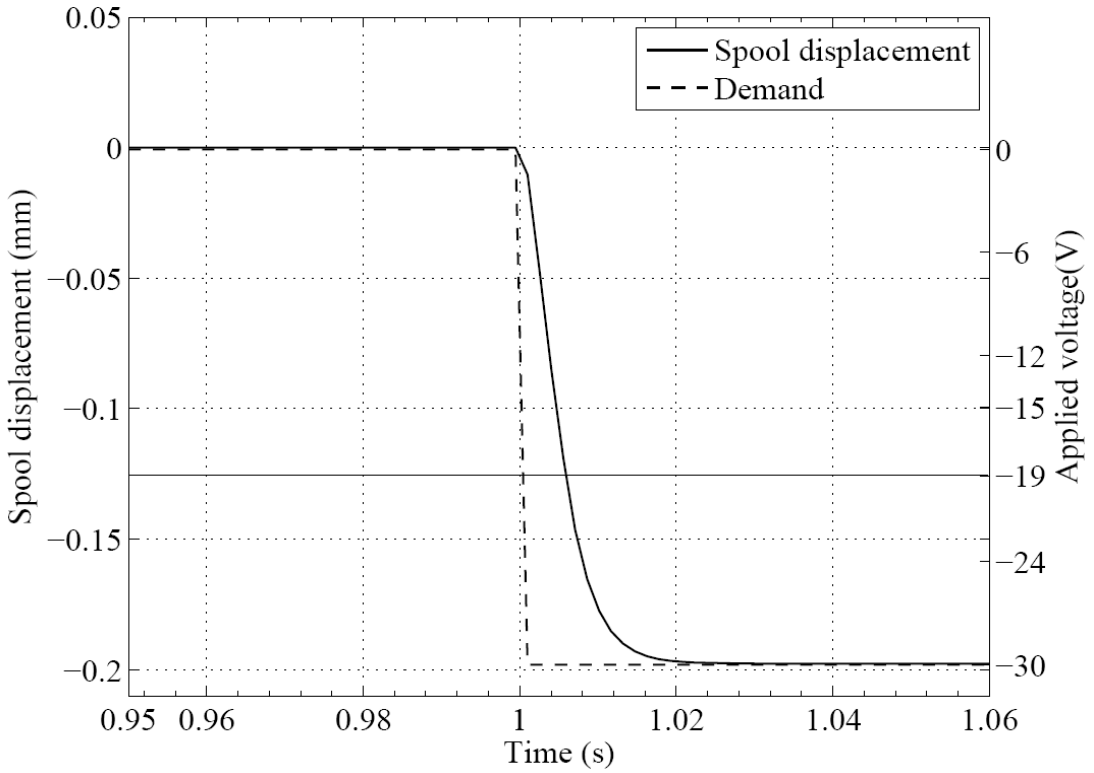

Figure 3.20: Simulated step response of the valve spool at 140bar supply pressure

Figure 3.20 shows the simulated step response of the valve at 140bar supply pressure. The step size chosen is 30V. The steady state displacement of the spool is approximately 0.2mm. This agrees with the frequency response results. The spool stroke is approximately 40% of the 26 series donor valve's maximum stroke.

Figure 3.21 shows the spool position plotted against voltage. The simulations were performed with a 0.5Hz sinusoidal voltage at 140bar supply pressure. The hysteretic behaviour of the bimorph can be observed in the spool response. The hysteresis is approximately ±4%.

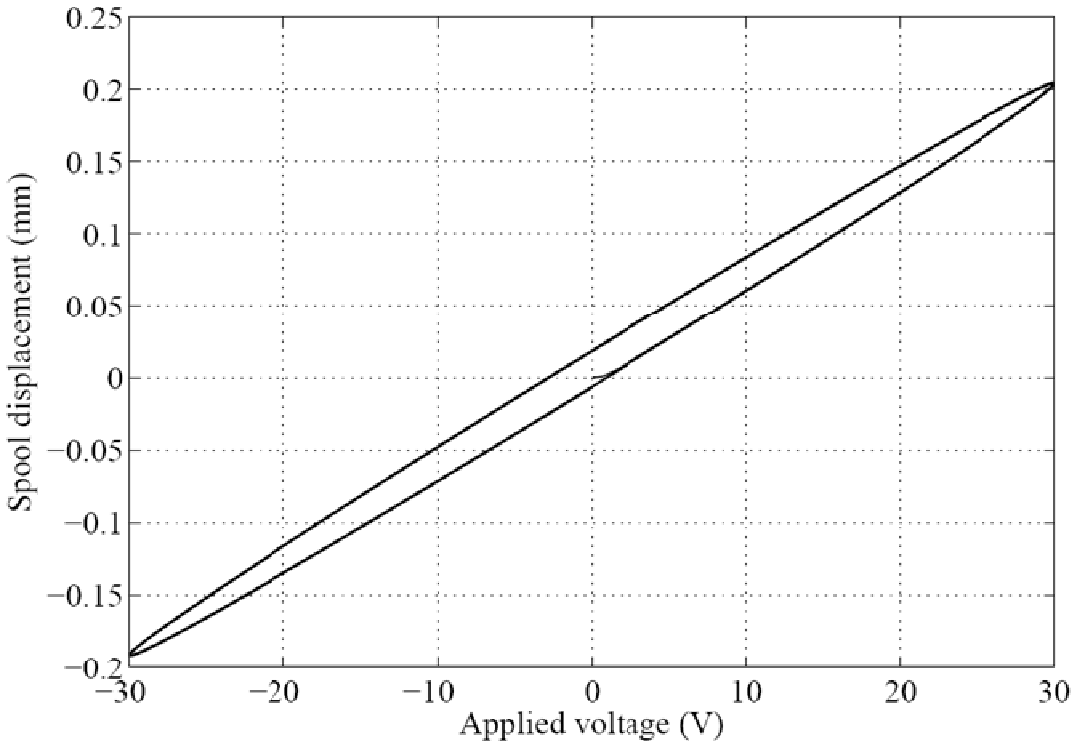

Figure 3.21: Spool response at 140bar supply pressure

To establish the most important parameters that influence the frequency response and the steady state gain of the valve, the model needs to be linearised. The linearization of the system is considered next.

3.7 Linear approximation of the nonlinear valve model

Typically in servovalve systems, the linear approximation of the dynamic model is based about a steady state operating point [49]. This operating point is generally chosen as the initial operating condition. In this condition the demand is zero and the valve is at the null position. When the input voltage is zero, the deflector will be in the mid position and the flows into the control ports will be equal. Therefore the pressure in the control ports will be equal, thus holding the second stage spool in its mid position. Assuming symmetry for the valve, the steady state control port pressures at this condition can be calculated using Eq.(74). Thereafter, the system performance can be approximated about this point.

At the initial condition V, x_d, x_s, and time t, are zero. Equation (74) simplifies to

$$Q_{pae} = 0$$

(78)

where, subscript *e* represents the parameters in the equilibrium state. Substituting Eq.(70) into Eq.(78) gives

$$Q_{p1e} - Q_{p2e} = 0$$

(79)

At the initial condition, Eq.(67) and Eq.(69) simplify to

$$Q_{p1e} = c_{df} dx_0 \sqrt{\frac{2}{\rho}\left(P_s - P_{pae}\right)}$$

(80)

And

$$Q_{p2e} = c_{df} d(R_w - x_0) \sqrt{\frac{2}{\rho}\left(P_{pae} - P_r\right)}$$

(81)

Substituting Eq.(80) and Eq.(81) into Eq.(79) gives

$$\left[c_{df} dx_0 \sqrt{\frac{2}{\rho}\left(P_s - P_{pae}\right)}\right] - \left[c_{df} d(R_w - x_0) \sqrt{\frac{2}{\rho}\left(P_{pae} - P_r\right)}\right] = 0$$

(82)

Simplifying and rearranging Eq.(82) for P_{pae}

$$P_{pae} = \frac{{x_0}^2 P_s + (R_w - x_0)^2 P_r}{(R_w - x_0)^2 + {x_0}^2}$$

(83)

Due to symmetry

$$P_{pae} = P_{pbe} \tag{84}$$

where, P_{pae} and P_{pbe} are the equilibrium operating pressures. And now the performance of the valve can be linearised about this point.

3.6.1 Linear approximation of flow Q_{p1}

At time, *t*, flow, Q_{p1} is

$$Q_{p1}(t) = c_{df} d\big(x_0 + x_d(t)\big)\sqrt{\frac{2}{\rho}\Big(P_s - P_{pa}(t)\Big)} \tag{85}$$

The derivative of Q_{p1} with respect to x_d, about the operating point is

$$\frac{\partial Q_{p1}}{\partial x_d} = c_{df} d\sqrt{\frac{2}{\rho}\big(P_s - P_{pae}\big)} \tag{86}$$

The derivative of Q_{p1} with respect to P_{pa}, about the operating point is

$$\frac{\partial Q_{p1}}{\partial x_d} = \frac{-c_{df} d x_0\sqrt{\frac{2}{\rho}}}{2\sqrt{\big(P_s - P_{pae}\big)}} \tag{87}$$

Therefore Q_{p1} can be approximated as the sum of the integrals of Eq.(86) and Eq.(87)

$$Q_{p1}(t) = \left[c_{df} d\sqrt{\frac{2}{\rho}\big(P_s - P_{pae}\big)}\right] x_d(t) + \left[\frac{-c_{df} d x_0\sqrt{\frac{2}{\rho}}}{2\sqrt{\big(P_s - P_{pae}\big)}}\right] P_{pa}(t) \tag{88}$$

3.6.2 Linear approximation of flow Q_{p2}

At time, *t*, flow, Q_{p2} is

$$Q_{p2}(t) = c_{df} d[(R_w - x_0) - x_d(t)] \sqrt{\frac{2}{\rho}\left(P_{pa}(t) - P_r\right)} \tag{89}$$

The derivative of Q_{p2} with respect to x_d, about the operating point is

$$\frac{\partial Q_{p2}}{\partial x_d} = -c_{df} d \sqrt{\frac{2}{\rho}\left(P_{pae} - P_r\right)} \tag{90}$$

The derivative of Q_{p1} with respect to P_{pa}, about the operating point is

$$\frac{\partial Q_{p2}}{\partial P_{pa}} = \frac{c_{df} d(R_w - x_0)\sqrt{\frac{2}{\rho}}}{2\sqrt{\left(P_{pae} - P_r\right)}} \tag{91}$$

Therefore, Q_{p2} can be approximated as the sum of the integrals of Eq.(90) and Eq.(91)

$$Q_{p2}(t) = \left[-c_{df} d \sqrt{\frac{2}{\rho}\left(P_{pae} - P_r\right)}\right] x_d(t) + \left[\frac{c_{df} d(R_w - x_0)\sqrt{\frac{2}{\rho}}}{2\sqrt{\left(P_{pae} - P_r\right)}}\right] P_{pa}(t) \tag{92}$$

3.6.3 Linear approximation of flow Q_{pa}

Q_{pa} at time, t is given by

$$Q_{pa}(t) = Q_{p1}(t) - Q_{p2}(t) \tag{93}$$

Substituting for $Q_{p1}(t)$ and $Q_{p2}(t)$ in Eq.(93)

$$Q_{pa}(t) = \left[c_{df} d \sqrt{\frac{2}{\rho}\left(P_s - P_{pae}\right)}\right] x_d(t) + \left[\frac{-c_{df} d x_0 \sqrt{\frac{2}{\rho}}}{2\sqrt{\left(P_s - P_{pae}\right)}}\right] P_{pa}(t)$$
$$- \left[-c_{df} d \sqrt{\frac{2}{\rho}\left(P_{pae} - P_r\right)}\right] x_d(t) + \left[\frac{c_{df} d (R_w - x_0)\sqrt{\frac{2}{\rho}}}{2\sqrt{\left(P_{pae} - P_r\right)}}\right] P_{pa}(t)$$

(94)

Simplifying gives

$$Q_{pa}(t) = (w_1 + w_2) x_d(t) - (u_1 + u_2) P_{pa}(t)$$

(95)

where

$$w_1 = c_{df} d \sqrt{\frac{2}{\rho}\left(P_s - P_{pae}\right)}$$

(96)

$$w_2 = c_{df} d \sqrt{\frac{2}{\rho}\left(P_{pae} - P_r\right)}$$

(97)

$$u_1 = \frac{c_{df} d x_0 \sqrt{\frac{2}{\rho}}}{2\sqrt{\left(P_s - P_{pae}\right)}}$$

(98)

$$u_2 = \frac{c_{df} d (R_w - x_0)\sqrt{\frac{2}{\rho}}}{2\sqrt{\left(P_{pae} - P_r\right)}}$$

(99)

3.6.4 Linear approximation of flow Q_{p3}

At time, t, flow, Q_{p3} is

$$Q_{p3}(t) = c_{df} d\big(x_0 - x_d(t)\big)\sqrt{\frac{2}{\rho}\Big(P_s - P_{pb}(t)\Big)}$$

(100)

The derivative of Q_{p3} with respect to x_d, about the operating point is

$$\frac{\partial Q_{p3}}{\partial x_d} = -c_{df} d\sqrt{\frac{2}{\rho}\big(P_s - P_{pae}\big)}$$

(101)

The derivative of Q_{p3} with respect to P_{pb}, about the operating point is

$$\frac{\partial Q_{p3}}{\partial P_{pb}} = \frac{-c_{df} d x_0\sqrt{\frac{2}{\rho}}}{2\sqrt{\big(P_s - P_{pae}\big)}}$$

(102)

Q_{p3} can be approximated as the sum of the integrals of Eq.(101) and Eq.(102)

$$Q_{p3}(t) = \left[-c_{df} d\sqrt{\frac{2}{\rho}\big(P_s - P_{pae}\big)}\right] x_d(t) + \left[\frac{-c_{df} d x_0\sqrt{\frac{2}{\rho}}}{2\sqrt{\big(P_s - P_{pae}\big)}}\right] P_{pb}(t)$$

(103)

Equation (103) can be expressed as

$$Q_{p3}(t) = -w_1 x_d(t) - u_1 P_{pb}(t)$$

(104)

3.6.5 Linear approximation of flow Q_{p4}

At time, t, flow, Q_{p4} is

$$Q_{p4}(t) = c_{df} d[(R_w - x_0) + x_d(t)]\sqrt{\frac{2}{\rho}\big(P_{pb}(t) - P_r\big)}$$

(105)

The derivative of Q_{p4} with respect to x_d, about the operating point is

$$\frac{\partial Q_{p4}}{\partial x_d} = c_{df} d \sqrt{\frac{2}{\rho}\left(P_{pae} - P_r\right)}$$

(106)

The derivative of Q_{p4} with respect to P_{pb}, about the operating point is

$$\frac{\partial Q_{p4}}{\partial P_{pb}} = \frac{c_{df} d (R_w - x_0)\sqrt{\frac{2}{\rho}}}{2\sqrt{\left(P_{pae} - P_r\right)}}$$

(107)

Q_{p3} can be approximated as the sum of the integrals of Eq.(106) and Eq.(107)

$$Q_{p4}(t) = \left[c_{df} d \sqrt{\frac{2}{\rho}\left(P_{pae} - P_r\right)}\right] x_d(t) + \left[\frac{c_{df} d (R_w - x_0)\sqrt{\frac{2}{\rho}}}{2\sqrt{\left(P_{pae} - P_r\right)}}\right] P_{pb}(t)$$

(108)

Equation (108) can be expressed as

$$Q_{p4}(t) = w_2 x_d(t) + u_2 P_{pb}(t)$$

(109)

3.6.6 Linear approximation of flow Q_{pb}

Q_{pb} at time, t is given by

$$Q_{pb}(t) = Q_{p4}(t) - Q_{p3}(t)$$

(110)

Substituting for $Q_{p3}(t)$ and $Q_{p4}(t)$ in Eq.(93)

$$Q_{pb}(t) = \left[w_2 x_d(t) + u_2 P_{pb}(t)\right] - \left[-w_1 x_d(t) - u_1 P_{pb}(t)\right]$$

(111)

Simplifying gives

$$Q_{pb}(t) = (w_1 + w_2)x_d(t) + (u_1 + u_2)P_{pa}(t)$$

(112)

3.6.7 Linearisation of control port pressure P_{pa}

The derivative of the control port pressure, P_{pa}, is given by Eq. (74). Equation (74) can be expressed as

$$\frac{dP_{pa}}{dt}(t) = \frac{\beta_f}{V_{pa}}\left(Q_{pa}(t) - A_s\frac{dx_s}{dt}(t)\right)$$

(113)

Substituting for $Q_{pa}(t)$ gives,

$$\frac{dP_{pa}}{dt}(t) = \frac{\beta_f}{V_{pa}}\left((w_1 + w_2)x_d(t) - (u_1 + u_2)P_{pa}(t) - A_s\frac{dx_s}{dt}(t)\right)$$

(114)

Using '*s*' as a differential operator Eq.(114) can be expressed as

$$sP_{pa} = \frac{\beta_f}{V_{pa}}\left((w_1 + w_2)x_d - (u_1 + u_2)P_{pa} - sA_sx_s\right)$$

(115)

Rearranging for P_{pa} gives

$$P_{pa} = \frac{(w_1 + w_2)x_d - sA_sx_s}{s\frac{V_{pa}}{\beta_f} + (u_1 + u_2)}$$

(116)

3.6.8 Linearisation of control port pressure P_{pb}

The derivative of control port pressure P_{pb} is given in Eq.(75). Equation (75) can be expressed as

$$\frac{dP_{pb}}{dt}(t) = \frac{\beta_f}{V_{pb}}\left(A_s \frac{dx_s}{dt}(t) - Q_{pb}(t)\right)$$

(117)

Substituting for $Q_{pb}(t)$ gives

$$\frac{dP_{pb}}{dt}(t) = \frac{\beta_f}{V_{pb}}\left[A_s \frac{dx_s}{dt}(t) - (w_1 + w_2)x_d(t) - (u_1 + u_2)P_{pa}(t)\right]$$

(118)

Using '*s*' as a differential operator Eq.(118) can be expressed as

$$sP_{pb} = \frac{\beta_f}{V_{pb}}\left[sA_s x_s - (w_1 + w_2)x_d - (u_1 + u_2)P_{pa}\right]$$

(119)

Rearranging for P_{pb} gives

$$P_{pb} = \frac{sA_s x_s - (w_1 + w_2)x_d}{s\frac{V_{pa}}{\beta_f} + (u_1 + u_2)}$$

(120)

The linearised control port pressures and control port flows can now be used to linearise the first stage and second stage dynamics.

3.6.7 Linearisation of the first stage dynamics

The first stage equation of motion defining the deflector dynamics is given by Eq.(66). The behaviour of the bimorph is assumed to be linear. Therefore the hysteretic characteristic of the bimorph is assumed to be negligible and is therefore not considered. The first stage flow force is proportional to the deflector displacement, x_d. Therefore Eq. (66) can be expressed as

$$m_d \frac{d^2 x_d}{dt^2}(t) + c_d \frac{dx_d}{dt}(t) = F_d(t) - K_{ff}(t)$$

(121)

Substituting for F_d

$$m_d \frac{d^2 x_d}{dt^2}(t) + c_d \frac{dx_d}{dt}(t) = k_4 V(t) - k_5 x_d(t) - k_6 x_s(t) - K_{ff}(t)$$

(122)

To be consistent with the nonlinear model, the reference axis of x_s is defined opposite to that of x_d. Using 's' as a differential operator Eq. (122) can be expressed as

$$s^2 m_d x_d + s c_d x_d = k_4 V - k_5 x_d - k_6 x_s - K_{ff} x_d$$

(123)

Rearranging for x_d

$$x_d = \frac{k_4 V - k_6 x_s}{s^2 m_d + s c_d + k_5 + K_{ff}}$$

(124)

3.6.8 Linearisation of the second stage dynamics

The spool dynamics are defined by Eq.(76). The flow force at the spool is a nonlinearity. Therefore the second stage flow force is neglected in the linearised model. Equation (76) can be expressed as

$$m_s \frac{d^2 x_s}{dt^2}(t) + c_s \frac{dx_s}{dt}(t) = A_s \left(P_{pa}(t) - P_{pb}(t) \right) - F_s(t)$$

(125)

Substituting for F_s

$$m_s \frac{d^2 x_s}{dt^2}(t) + c_s \frac{dx_s}{dt}(t) = A_s \left(P_{pa}(t) - P_{pb}(t) \right) + n_4 V(t) + n_5 x_d(t) - n_6 x_s(t)$$

(126)

The reference axis of x_s is defined opposite to that of the deflector for consistency. Using 's' as a differential operator Eq.(126) can be expressed as

$$s^2 m_s x_s + s c_s x_s = A_s \left(P_{pa} - P_{pb} \right) + n_4 V + n_5 x_d - n_6 x_s$$

(127)

Substituting for P_{pa} and P_{pb}

$$s^2 m_s x_s + s c_s x_s = A_s \left[\frac{(w_1 + w_2) x_d - s A_s x_s}{s \frac{V_{pa}}{\beta_f} + (u_1 + u_2)} - \frac{s A_s x_s - (w_1 + w_2) x_d}{s \frac{V_{pa}}{\beta_f} + (u_1 + u_2)} \right] + n_4 V + n_5 x_d - n_6 x_s \tag{128}$$

Substituting for x_d

$$s^2 m_s x_s + s c_s x_s = A_s \left[\frac{(w_1 + w_2) \frac{k_4 V + k_6 x_s}{s^2 m_d + s c_d + k_5 + K_{ff}} - s A_s x_s}{s \frac{V_{pa}}{\beta_f} + (u_1 + u_2)} - \frac{s A_s x_s - (w_1 + w_2) \frac{k_4 V + k_6 x_s}{s^2 m_d + s c_d + k_5 + K_{ff}}}{s \frac{V_{pa}}{\beta_f} + (u_1 + u_2)} \right] + n_4 V + n_5 \frac{k_4 V + k_6 x_s}{s^2 m_d + s c_d + k_5 + K_{ff}} - n_6 x_s \tag{129}$$

Simplifying and rearranging Eq.(129) gives

$$\frac{x_s}{V} = \frac{\frac{k_6}{s^2 m_d + s c_d + k_5 + K_{ff}} \left[n_5 + \frac{2 A_s (w_1 + w_2)}{s \frac{V_{pa}}{\beta_f} + (u_1 + u_2)} \right] + n_4}{s^2 m_s + s c_s + n_6 + \frac{s 2 {A_s}^2}{s \frac{V_{pa}}{\beta_f} + (u_1 + u_2)} + \frac{k_6}{s^2 m_d + s c_d + k_5 + K_{ff}} \left[n_5 + \frac{2 A_s (w_1 + w_2)}{s \frac{V_{pa}}{\beta_f} + (u_1 + u_2)} \right]} \tag{130}$$

Substituting the values for the parameters in the above transfer function will yield the linearised frequency response for the system. At 140bar supply pressure the transfer function for the valve is

$$T_{(s)} = \frac{x_s}{V}$$
$$= \frac{191.17(s + 8.38 \times 10^4)(s^2 - 4.46 \times 10^4 s + 4.65 \times 10^9)}{(s + 329)(s^2 + 3606s + 5.47 \times 10^7)(s^2 + 3.63 \times 10^4 s + 6.62 \times 10^8)} \quad (131)$$

The steady stage gain of $T_{(s)}$ is 6.25×10^{-3}m/V. Therefore at 30V demand voltage, the displacement is 0.19mm. This is 5% lower than the nonlinear simulation predictions. Figure 3.22 compares the frequency response of the linear and nonlinear models at 140bar supply pressure. The lag in the amplifier is not included in the models. The amplifier is assumed to be ideal. The frequency range of the nonlinear model is limited by computing memory. The magnitude plots in Figure 3.22 of the linear and nonlinear models show good agreement. The -3dB bandwidth of the linearised system is approximately 52Hz. This shows 100% agreement to the nonlinear model bandwidth at 3V.

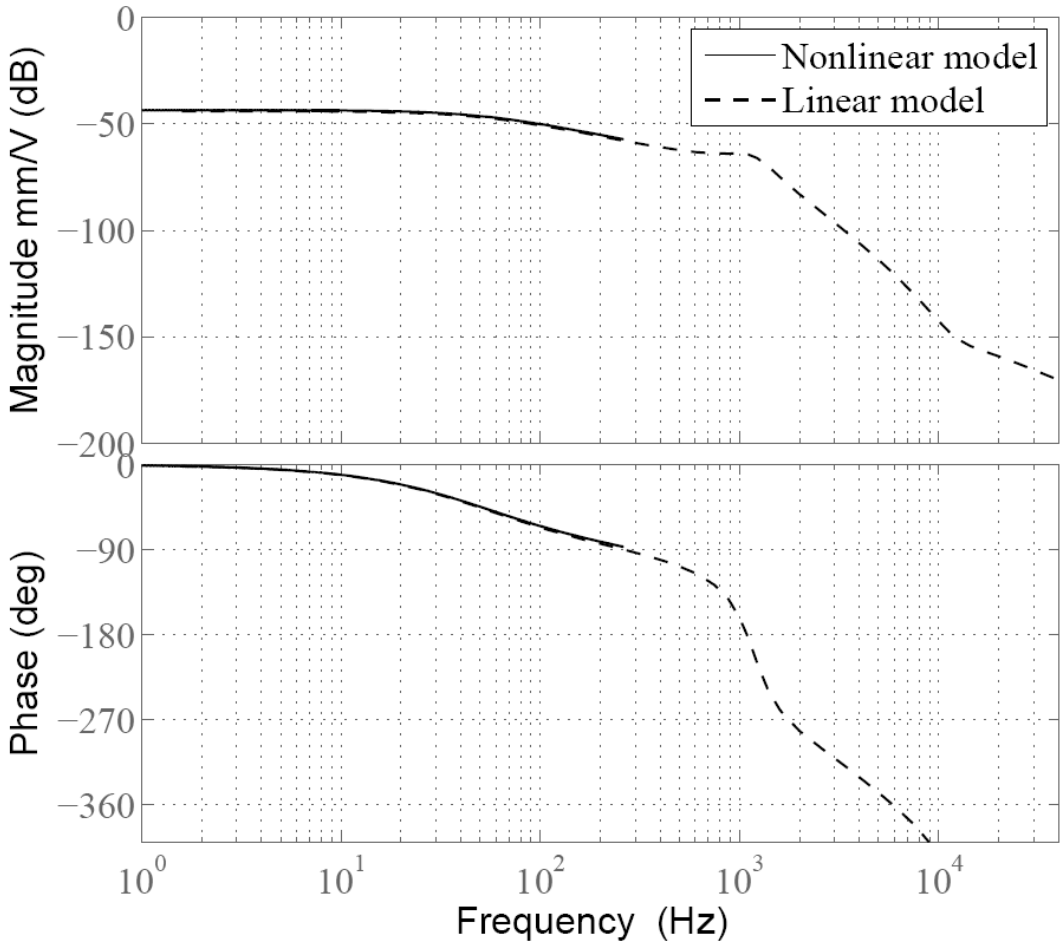

Figure 3.22: Comparison of linear and nonlinear (3V applied voltage amplitude) frequency response at 140bar supply pressure

The first break frequency of the linear model is at approximately 45Hz. The break frequency observed at approximately 1kHz corresponds to the natural frequency of the bimorph-feedback wire assembly. At 10khz the break point corresponds to the second stage spool dynamics. The poles that determine the break frequencies are given by Eq. (131). The break frequency at 45Hz is determined by a single pole. Increasing this frequency will improve the bandwidth of the valve. To identify the system parameters that determine this pole, the system needs to simplified.

The simplest transfer function that can represent the system response including the first break frequency is a first order lag. The following section discusses the development of the reduced order linear model.

3.7 Reduced order linear model of the valve

Assuming the higher order dynamics do not influence the slow pole of the system, the model can be reduced. The first stage dynamics only affect higher frequencies, so the equation of motion for the deflector reduces from Eq.(124) to

$$x_d = \frac{k_4 V - k_6 x_s}{k_5 + K_{ff}} \tag{132}$$

Assuming the fluid to be incompressible, the continuity equation for the first stage flow simplifies to

$$0 = A_s \frac{dx_s}{dt} - (w_1 + w_2) x_d \tag{133}$$

Using the differential operator and rearranging gives

$$s A_s x_s = (w_1 + w_2) x_d \tag{134}$$

Assuming the second stage dynamics to be fast, substituting Eq.(132) into Eq.(134) gives

$$s A_s x_s = (w_1 + w_2) \left[\frac{k_4 V - k_6 x_s}{k_5 + K_{ff}} \right] \tag{135}$$

The reduced model transfer function can be expressed as

$$\frac{x_s}{V} = \frac{k_4 (w_1 + w_2)}{s A_s \left(k_5 + K_{ff}\right) + k_6 (w_1 + w_2)} \tag{136}$$

Rearranging to the standard first order lag transfer function gives

$$\frac{x_s}{V} = \frac{\frac{k_4}{k_6}}{\frac{A_s(k_5 + K_{ff})}{k_6(w_1 + w_2)}s + 1}$$

(137)

Therefore the steady state gain, K_{ss}, of the valve is

$$K_{ss} = \frac{k_4}{k_6}$$

(138)

And the bandwidth, w_b, of the valve is

$$w_b = \frac{1}{\frac{A_s(k_5 + K_{ff})}{k_6(w_1 + w_2)}}$$

(139)

Rearranging gives

$$w_b = \frac{\frac{k_6}{(k_5 + K_{ff})}(w_1 + w_2)}{A_s}$$

(140)

The bandwidth of the valve is proportional to the steady state stiffness ratio, including the first stage flow force stiffness. Substituting the parameters at 140bar supply pressure yields the first order response

$$\frac{x_s}{V} = \frac{1.97}{s + 284.4}$$

(141)

The -3dB bandwidth of the valve predicted by the reduced model is 45Hz. This is approximately 13.5% lower than the higher order linear model prediction. The spool displacement predicted by the reduced model at 30V demand is approximately 0.2mm. This is 5% greater than the higher order linear model. The discrepancies between the modelling techniques are expected due to the approximation and

simplification made to the models. Figure 3.23 compares the reduced model frequency response to that of the higher order linear model at 140bar supply pressure. The trend of the reduced model response is in good agreement with the higher order model. Therefore the assumptions made for the reduced model are reasonable.

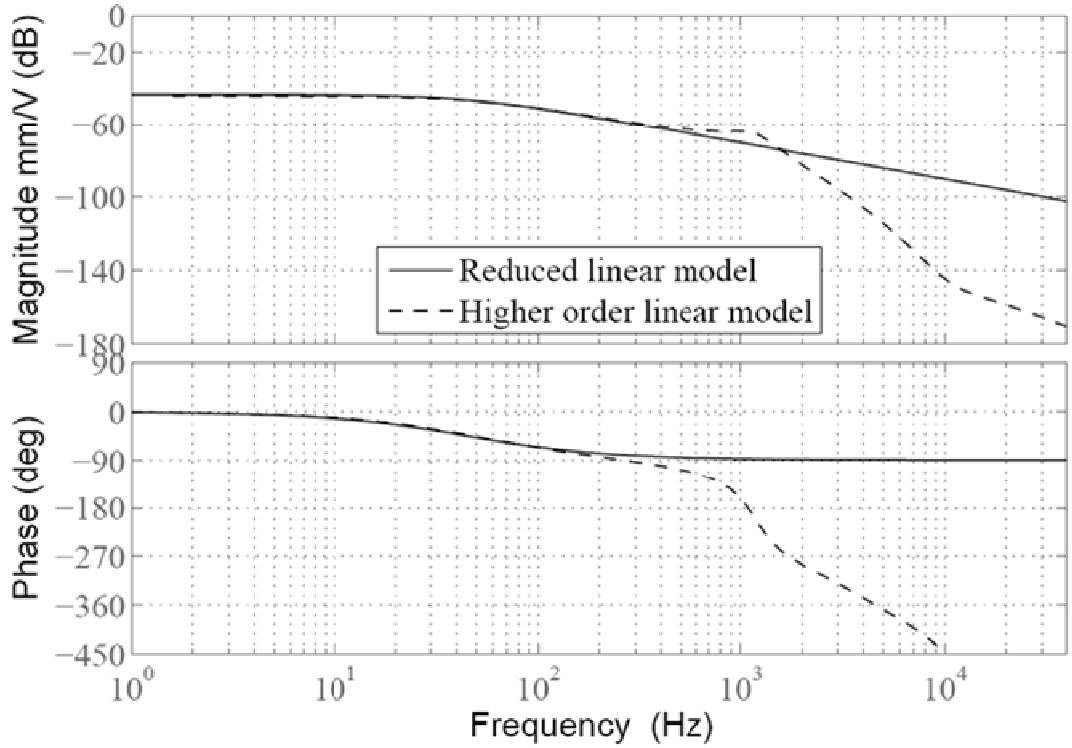

Figure 3.23: Comparison of reduced linear model frequency response to higher order linear model frequency response at 140bar supply pressure

3.8 Conclusion

A steady state analytical model for the bimorph-feedback wire assembly was developed to derive the stiffness constants which determine the deflector and spool displacements. To compare with the displacements predicted by the analytical model, an FEA model of the assembly was developed. The FEA model was partially validated using experimental measurements of the deflector. The results show good agreement. The validated FEA model was subsequently used to predict the deflector and spool displacement for discrete inputs of V, F_d and F_s. The results were within 5% difference to the steady state analytical model results. The stiffness constants were subsequently used to develop the dynamic model of the valve.

The flow force at the deflector was determined using CFD. The simulation results show that the flow force is proportional to the deflector displacement and the pressure drop across the deflector.

The nonlinear dynamic model was simulated using Matlab Simulink. The lag in the bimorph amplifier was measured and included in the simulations. At 140bar supply pressure and 30V applied voltage the -3dB bandwidth of the valve was approximately 40Hz. The -90 degrees phase frequency was at approximately 50Hz. The spool stroke was predicted to be approximately 0.38mm. At small applied voltage amplitudes (3V) the -3dB bandwidth of the valve increased to 52Hz. The nonlinear dynamic model was linearised to establish the most important parameters that influence the frequency response and the steady state gain of the valve. The frequency response of the linearised model was in 100% agreement with that of the nonlinear model at small applied voltages.

The higher order linear model was reduced to a first order lag system. The frequency response of this reduced model was 13.5% lower than the higher order linear model prediction. The system parameters that influence the pole at the first break frequency of the higher order models are the steady state stiffness constants k_5 and k_6 and the deflector flow force F_f. The steady state gain of the valve spool is proportional to the ratio k_4/k_6. k_4 and k_6 are the constants of proportionality giving the force at the

deflector generated due to the applied voltage and spool displacement, respectively, when the deflector is held in its null position. k_5 is the deflector stiffness when the spool is held in its null position.

A Bouc-Wen hysteresis model was developed to determine the hysteretic characteristic of the valve. The model was developed using the experimental measurements of the bimorph actuator. Hysteresis of ±4% was predicted at the spool.

The following section discusses the testing of the valve.

Chapter 4

Experimental results

4.1 Introduction

This chapter discusses the experimental set up and the test results of the PHSV. Two prototypes PVP1 (Piezoelectric Valve Prototype) and PVP2 were built and tested. The experiment results are used to validate the analytical models. The responses of the valve spool at varying operating conditions such as operating pressure and applied voltages are analysed. The spool response is compared to the flow response of the valve. The step response of the valve spool is also presented and discussed. The performance of the PHSV is analysed in relation to the donor valve.

4.2 Experimental setup

The experiment setup was developed using a test PC and LabVIEW data acquisition. To obtain the frequency response of the valve, LabVIEW was programmed to generate a swept frequency demand and collate the measured signals.

The flow ports of the PHSV were connected to an equal area double-ended hydraulic actuator. All tests were intended to be performed under no-load conditions. The test fluid used was HLP-32 mineral oil. A LVDT was used to measure the hydraulic actuator displacement. The displacement measurements can subsequently be used to obtain the flow though the valve. The valve LVDT measures position of the second stage spool. A controller was developed to maintain the hydraulic actuator about its mid position in continuous operations. This prevents the hydraulic actuator from hitting the end stops. Accumulators were used at the supply and return ports of the valve to provide constant pressure. This will reduce pressure fluctuations at high frequencies. The schematic of the experiment setup is shown in Figure 4.1. A photograph of the experiment setup is shown in Figure 4.2.

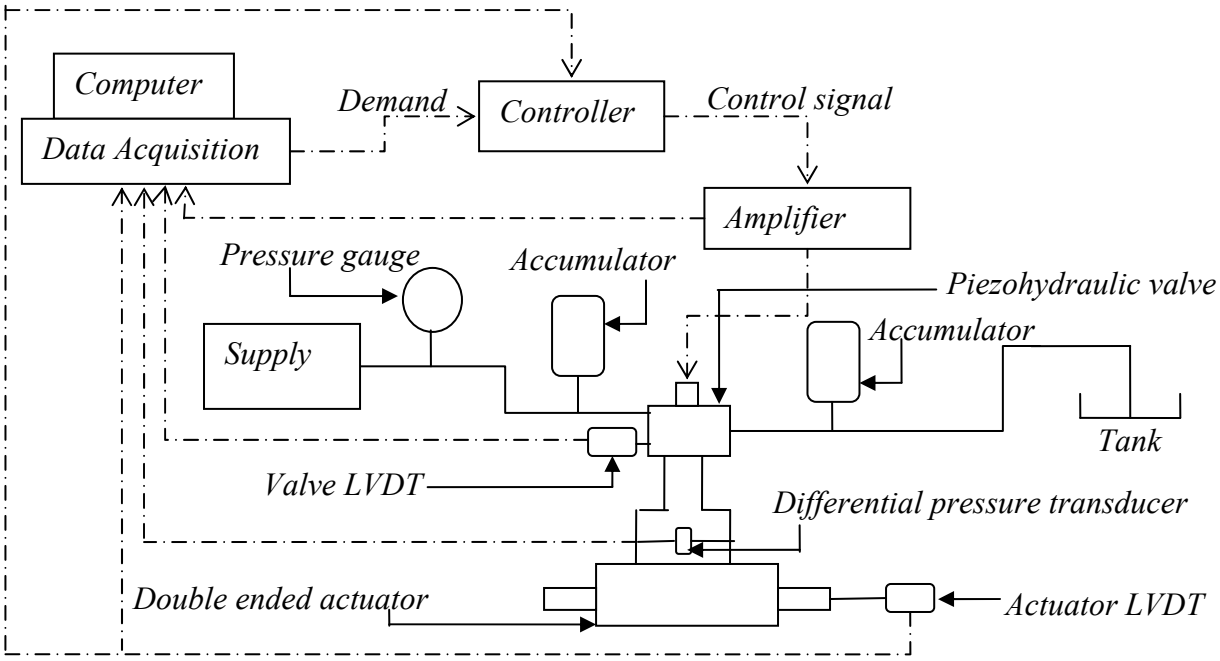

Figure 4.1: Schematic of the PHSV experimental setup

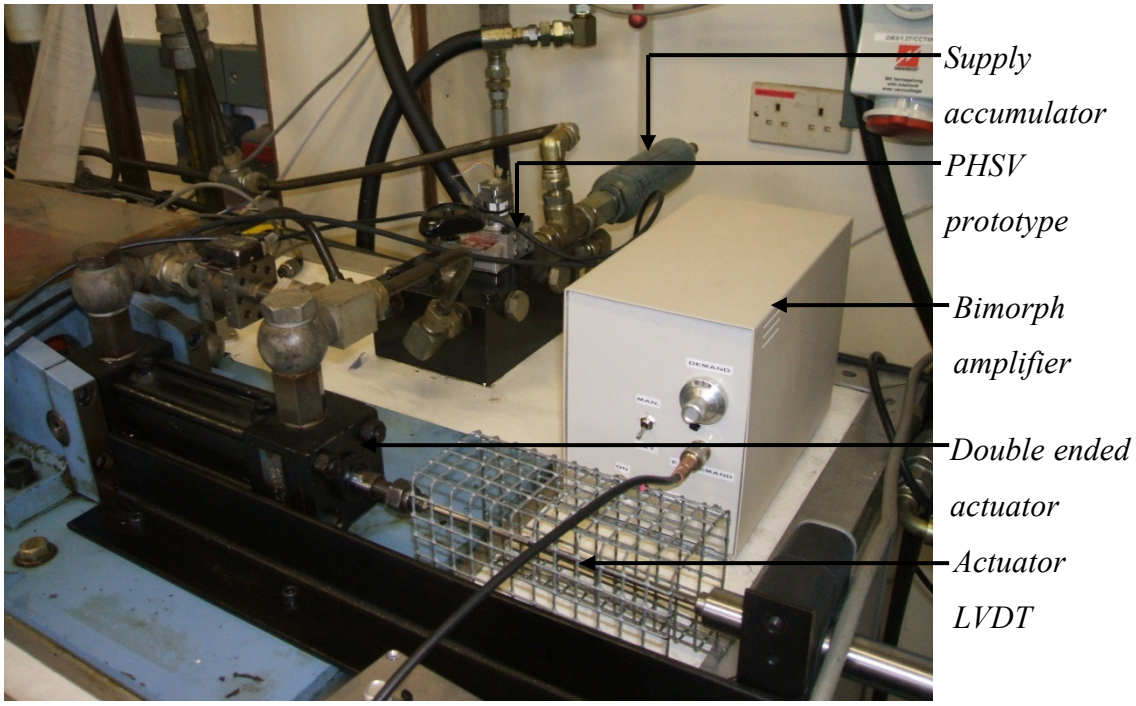

Figure 4.2: Photograph of the PHSV experiment setup

4.3 Comparison of experiment results to simulations

A frequency sweep from 1Hz to 100Hz was used. The maximum voltage for PVP1 was limited by the assembly tolerance. This was compensated by the controller. The controller offsets the demand voltage to operate the hydraulic actuator about its mid position. It does not significantly influence the amplitude of the demand. Hence the demand voltage can be expressed as the bimorph applied voltage to be consistent with the simulations. The controller limits the maximum amplitude of the applied voltage to ±22.5V. The frequency response of the spool position of PVP1 is compared to simulation results in Figure 4.3. The operating conditions are 140bar supply pressure and 22.5V applied voltage amplitude.

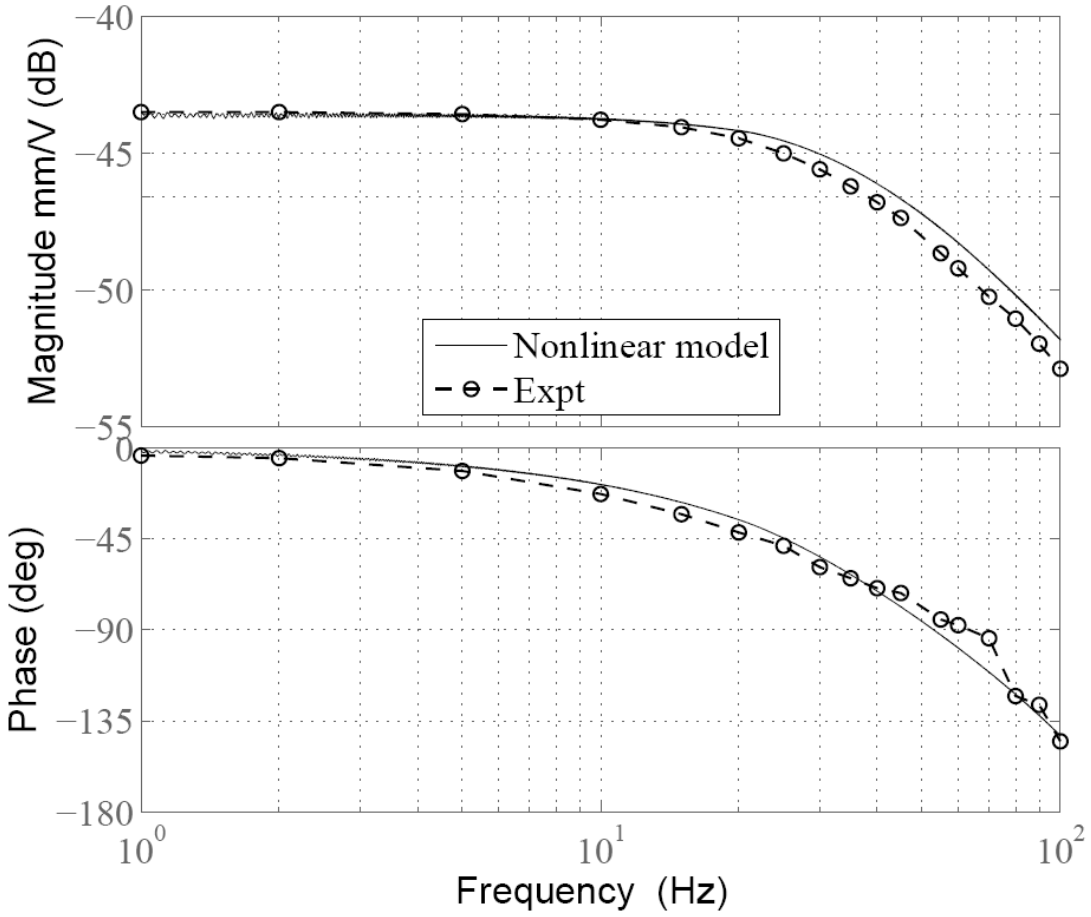

Figure 4.3: Comparison of spool position frequency response between experiment and simulation at 140bar supply pressure and 22.5V demand

Figure 4.3 shows good agreement between the experimental and simulated frequency response of the spool position. The -3dB bandwidth of the experiment results is approximately 38Hz. This is 13.6% slower compared to the predictions. In practice, the flow through the amplifier inlet and the deflector will experience some pressure drop, which will influence the frequency response. This was assumed negligible in the analytical model. In addition manufacturing and assembly tolerance can influence the flow recovery in the control ports and thus the frequency response.

At higher frequencies (>60Hz) the amplitude of the measured signal is small thus increasing the noise to signal ratio. This is predominantly evident in the phase plot of Figure 4.3. The measured data is less reliable at these frequencies. Nevertheless, the overall response of the valve agrees well with the simulation results.

Figure 4.4 compares the experiment spool displacement to simulation results at 1Hz operating frequency. The supply pressure is 140bar.

The simulated results shown in Figure 4.4 include the Bouc-Wen hysteresis model, discussed in section 3.4.1.2. The shape of the simulated response and the spool stroke are in good agreement. As predicted, the hysteresis of the valve spool is approximately ±4%. Additional offset to the hysteretic characteristic can be observed in the experiment results. This is because of the assembly tolerance in the first stage body. The error in the assembly misaligns the deflector in the amplifier, at the first stage. To compensate, the second stage body is intentionally misaligned to flex the feedback wire and pull the deflector to its null position. This aligns the deflector in the amplifier arrangement, however the bimorph remains pre-stressed. This pre-stress introduces nonlinearity in the valve response and the spool displaces less in the direction of the pre-stress.

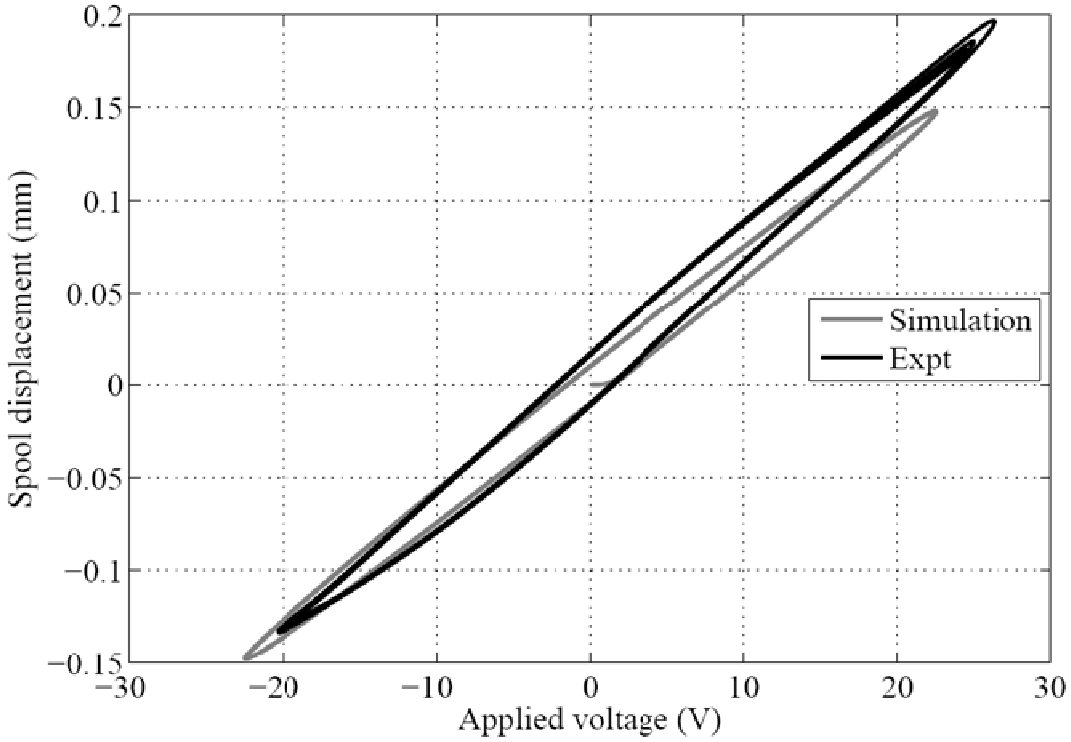

Figure 4.4: Comparison of spool displacement between experiment and simulation results at 140bar supply pressure and 22.5V applied voltage amplitude.

Overall, the performance of the valve spool is in reasonable agreement with the simulation results. Therefore the simulation models are assumed to be sufficient to predict the valve performance with reasonable accuracy. The performance of the valve at alternative operating conditions is considered next.

4.4 Additional experimental frequency response results

4.4.1 Frequency response of the spool at varying applied voltage

Figure 4.5 compares the frequency response of the spool at ±22.5V, ±10.5V and ±3V applied voltage. The supply pressure is kept constant at 140bar. The magnitude plots in Figure 4.5 are normalised.

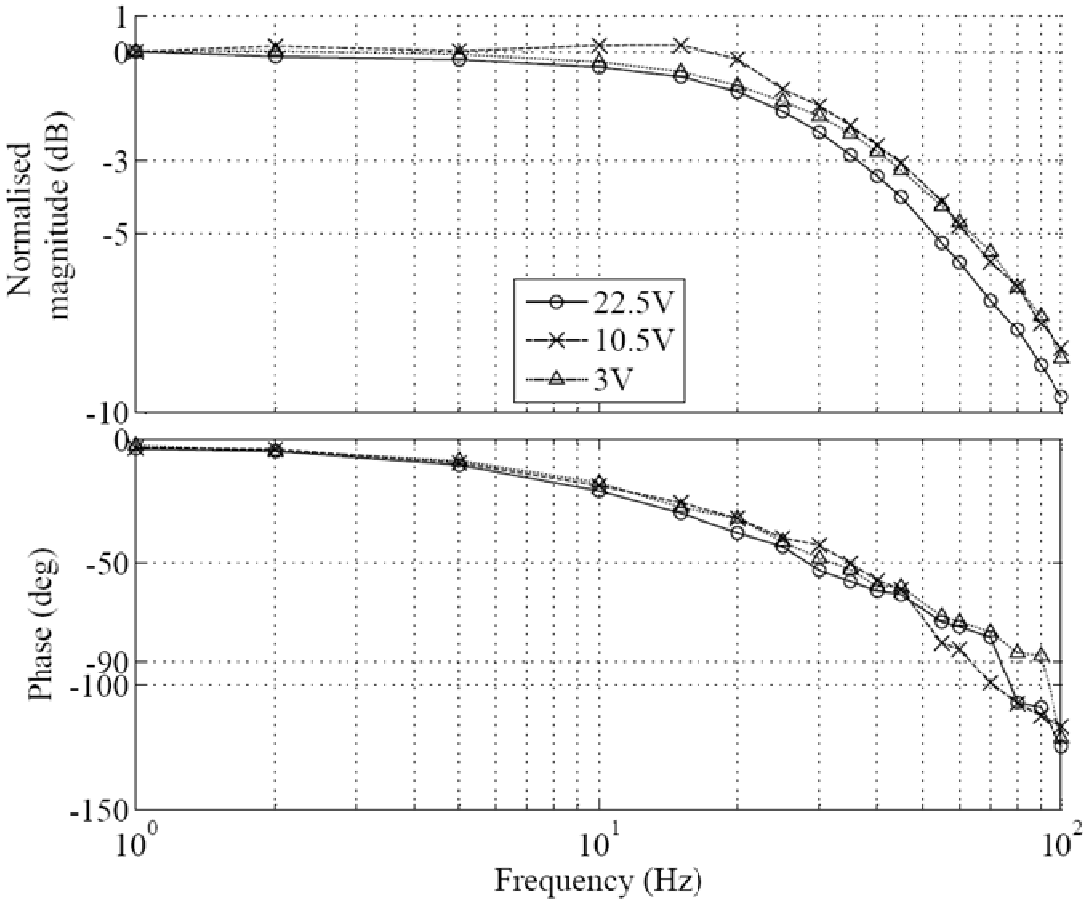

Figure 4.5: Normalised frequency response of the spool for varying applied voltage at 140bar supply pressure

The -3dB bandwidth of the spool marginally increases with decrease in applied voltage. This is because of the nonlinearities associated with the valve. At 3V applied voltage the -3dB bandwidth increases to approximately 44Hz. The measured -3dB bandwidth of the valve to at this applied voltage is approximately 15% slower than the simulation predictions. The reliability of the phase response is greatly reduced at higher frequencies due to the increase in noise to signal ratio. The response of the valve is reasonably consistent with varying applied voltage.

4.4.2 Frequency response of the spool at varying supply pressures

Figure 4.6 compares the frequency response of the spool at 140bar, 100bar and 70bar supply pressure. The applied voltage is kept constant 22.5V.

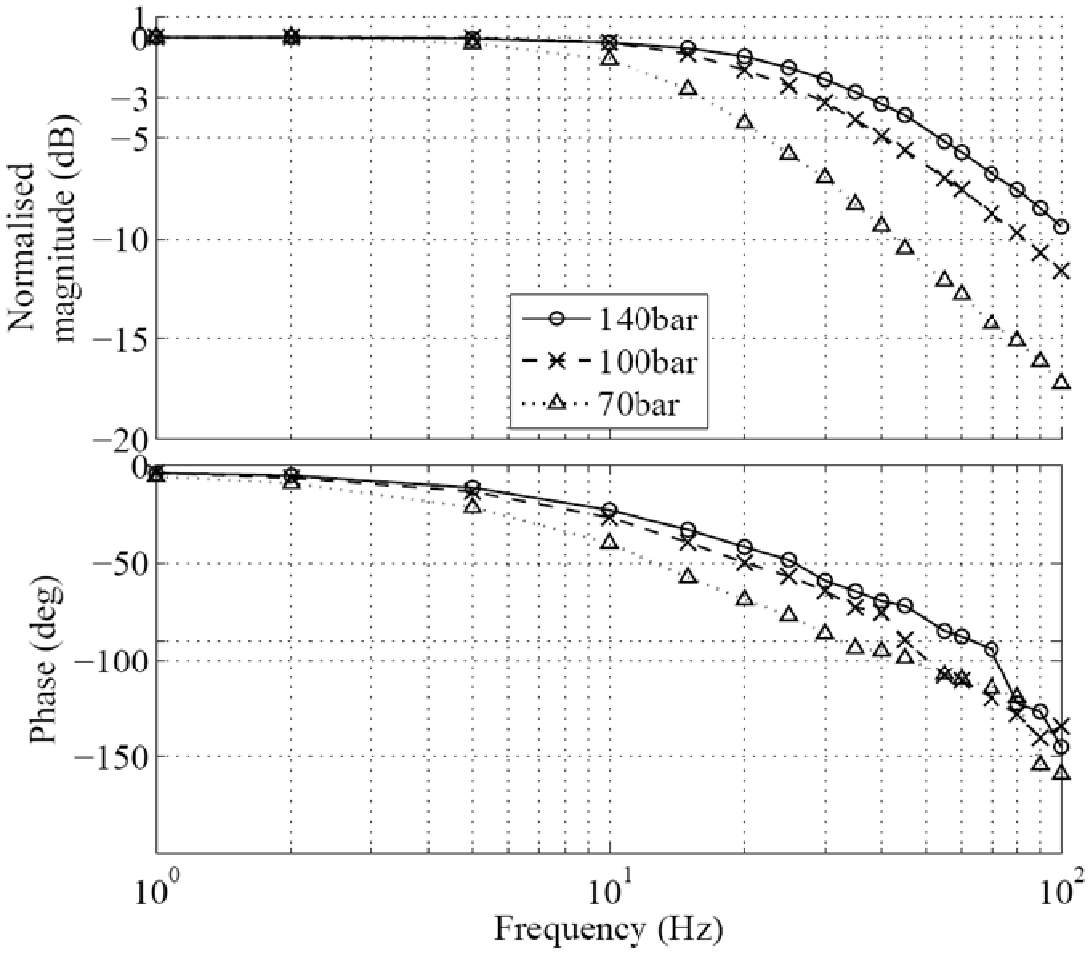

Figure 4.6: Normalised frequency response of the spool at varying supply pressures at 22.5V applied voltage amplitude

The -3dB bandwidth of the valve at 140bar and 100bar supply pressures are approximately 38Hz and 29Hz, respectively. At 70bar supply pressure, the drop in valve performance is substantial. The -3dB bandwidth is approximately 16Hz. The frequency response of the valve spool at 100bar supply pressure is 22.5% lower than nonlinear simulation predictions. At 70bar supply pressure the measured bandwidth is approximately 50% lower than nonlinear model prediction. This implies the nonlinearity of the valve at low operating pressures is not captured by the analytical model. The approximation of the control port flows into orifice flows is likely to be less accurate at low pressures.

Equation (140) shows that the bandwidth of the valve spool is related to the pressures in the control ports, as these affect w_1 and w_2. A higher supply pressure increases the

pressure recovery in the control ports and thus the control ports flows. This increases the spool velocity, therefore improving the frequency response of the valve.

Thus far, the frequency response of the valve has been determined by the second stage spool measurements. To validate this, the frequency response of the flow through the valve is considered.

4.4.3 Determining the frequency response of the valve using flow

The flow through the valve can be determined by the displacement measurement of the hydraulic actuator [81]. The flow can be expressed as

$$Q = 2\pi FYA_a \tag{142}$$

where Q is the amplitude of the flow through the valve, F is the operating frequency (Hz), Y is the hydraulic actuator displacement amplitude and A_a is the Annulus area of the piston. The frequency response of the valve can be obtained by substituting the parameters into Eq. (142). The response of the valve is shown in Figure 4.7. The hydraulic actuator displacement lags the spool displacement by 90 degrees. This phase lag is reproduced in the flow measurements. For comparison, the -90 degrees phase shift of the flow measurements is compensated in Figure 4.7 and the magnitude plot is normalised.

Figure 4.7 compares the frequency response of the spool and valve flow at 140bar supply pressure and 22.5V applied voltage amplitude. The phase of the flow increases at higher frequencies. This is possibly due to the influence of friction in the hydraulic actuator. The compressibility of the fluid will influence the response at higher frequencies and contribute to phase lag. Using the hydraulic stiffness and the mass of the hydraulic actuator, the resonant frequency of the actuator was calculated as approximately 130Hz. Therefore the dip in magnitude response in Figure 4.7 at 55Hz is not due to actuator resonance.

The stroke of the hydraulic actuator was substantially reduced at higher frequencies. Small signals are susceptible to noise contamination and the data becomes less

reliable at frequencies greater than 40Hz. At lower frequencies the results between the flow and spool responses are close. The actuator resonance is not expected to influence the measurements at these frequencies. Hence it is reasonable to conclude that the spool response results are a sufficient representation of the overall valve performance.

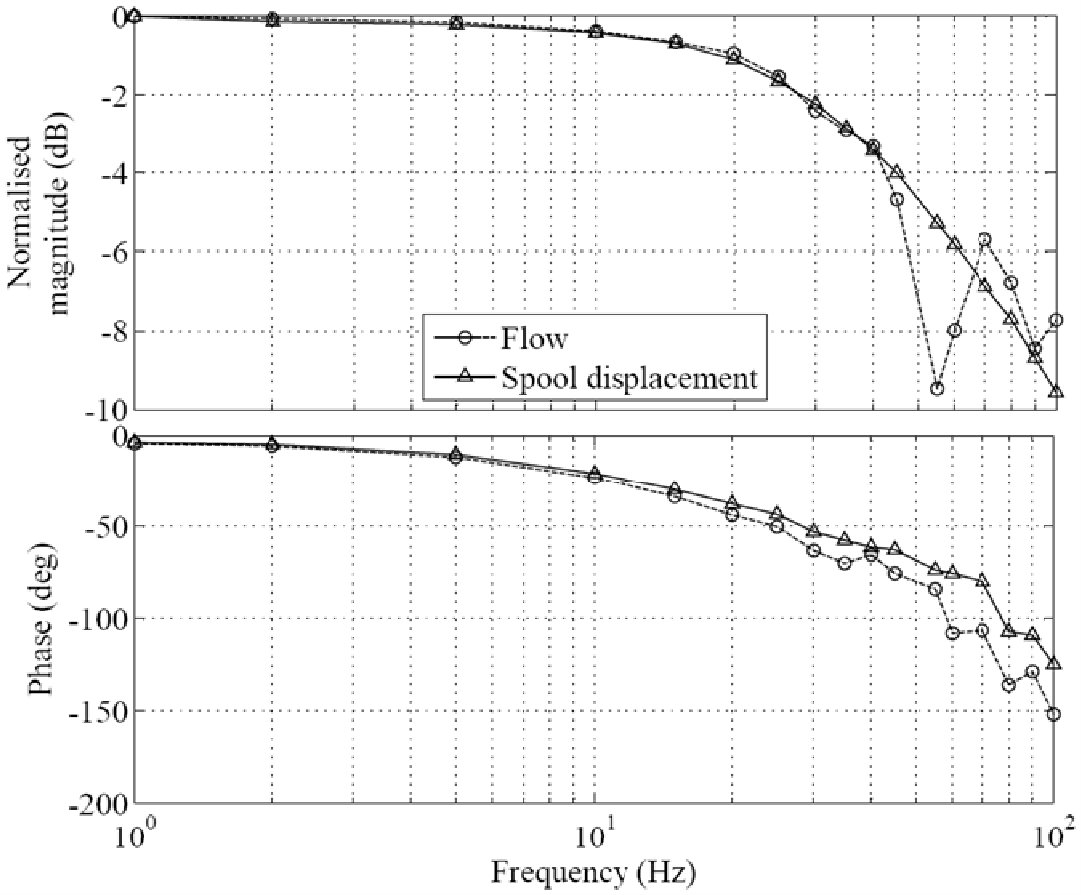

Figure 4.7: Normalised comparison of spool and flow frequency response at 140bar supply pressure and ±22.5V applied voltage.

4.5 Step response of the valve spool

Figure 4.8 shows the step response of the valve spool at 140bar supply pressure. A 30 to 0V bimorph voltage step was required, but due to amplifier dynamics a perfect step cannot be achieved. Figure 4.8 includes the demand step, amplifier response, simulated spool response and the measured spool response.

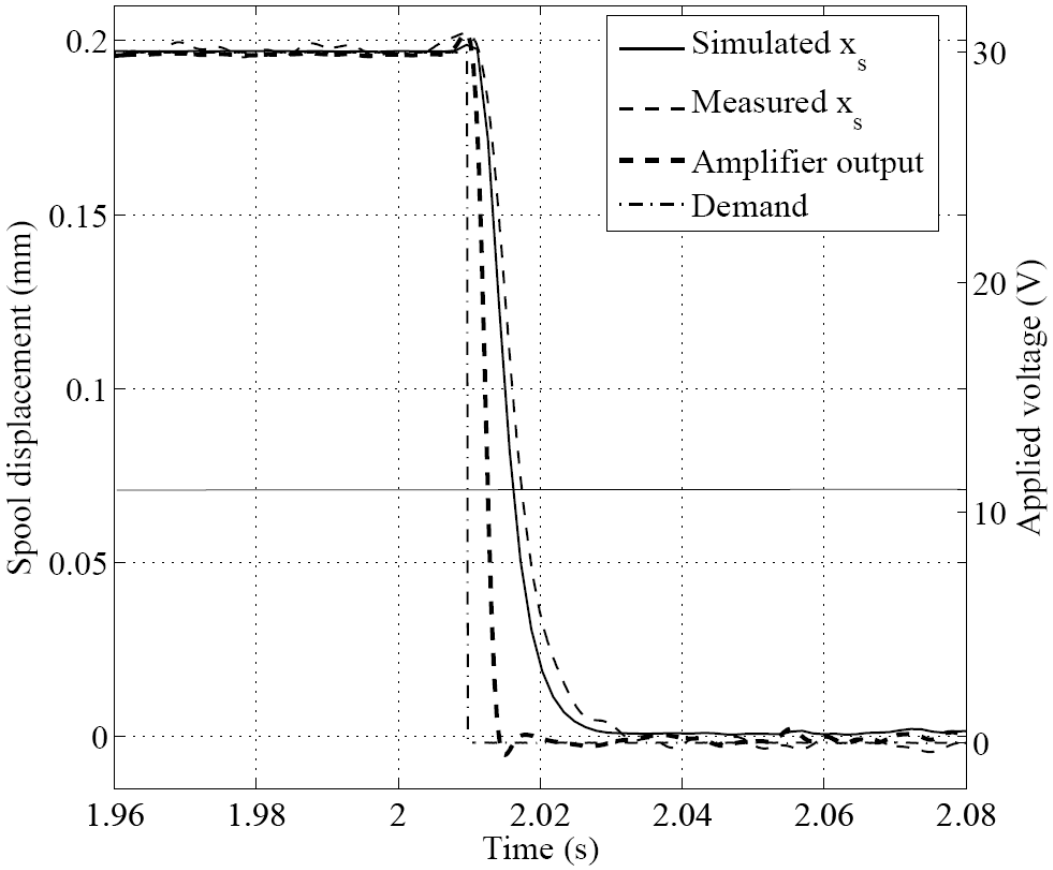

Figure 4.8: Step response of the valve spool at 140bar supply pressure

The measured displacement of the valve spool is approximately 0.21mm. This is 5% higher than the simulation predictions. The simulated spool response is marginally faster (1ms at first time constant) compared to the experiment results. However the overall trend and response between the simulated and measured response are in reasonably good agreement.

To confirm the consistency of the valve performance and the accuracy of the predictions, an identical second prototype, PVP2, was developed and tested. The experiment results of PVP2 are considered next.

4.6 Frequency response of second prototype

The construction of PVP2 was identical to PVP1. The bimorph and feedback wire characteristics of the two prototypes are the same. Therefore, the responses of the

two prototypes are expected to be similar. Figure 4.9 compares the frequency response of the spool of prototype PVP2 at 140bar and 70bar supply pressure to that of PVP1. The applied voltage amplitude is kept constant at 22.5V.

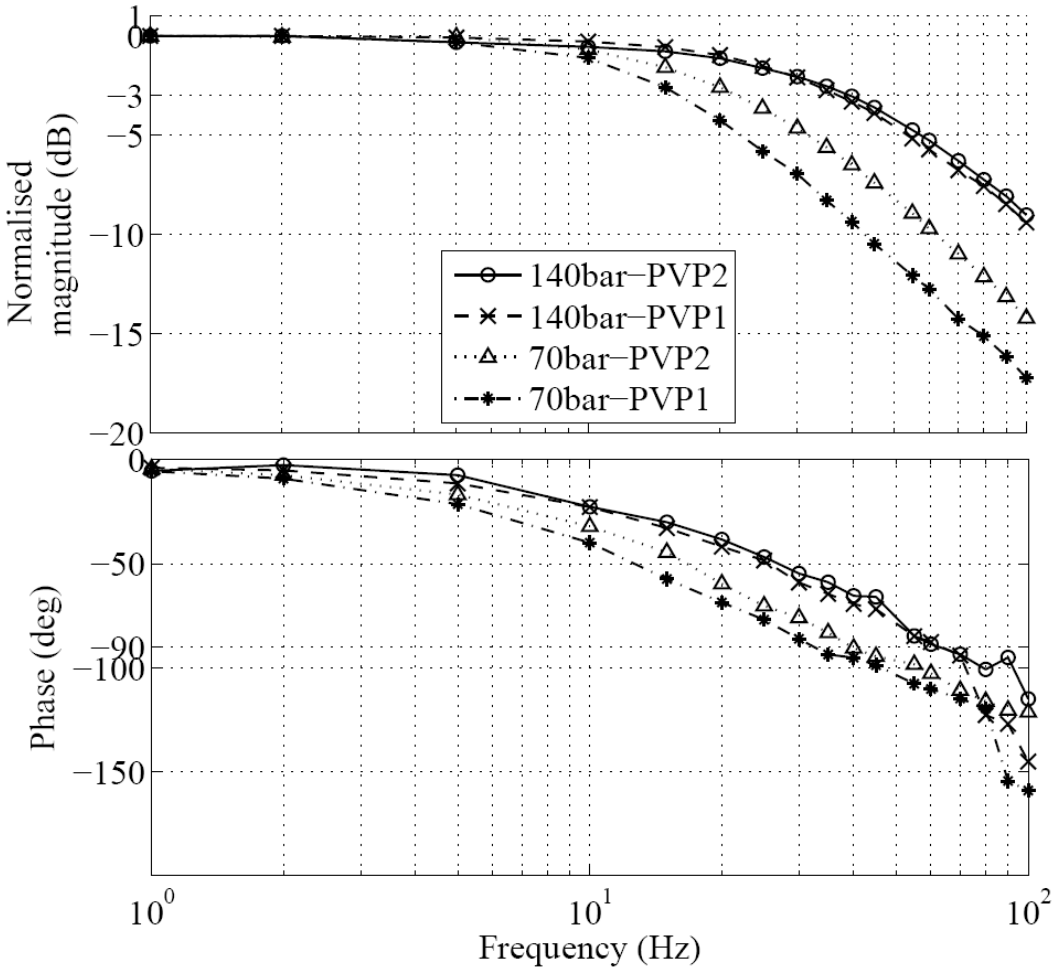

Figure 4.9: Comparison of normalised frequency response of the spool between PVP2 and PVP1 at varying supply pressures, at 22.5V applied voltage amplitude

The -3dB bandwidth of the PVP2 valve spool at 140bar supply pressure is approximately 41Hz. This is approximately 8% greater compared to PVP1 and is 9% lower than the simulation predictions. The -3dB bandwidths at 70bar supply pressure of PVP2 valve spool is 21Hz. The drop in performance at 70bar pressure drop is not as pronounced as in prototype PVP1. Overall, the frequency responses of the two prototypes are reasonably consistent with the simulation results and each other, for varying supply pressures.

The performances of PVP2 and PVP1 at varying applied voltages are shown in Figure 4.10. The frequency response of the spool at ±10.5V and ±3V applied voltages are considered. The supply pressure is kept constant at 140bar.

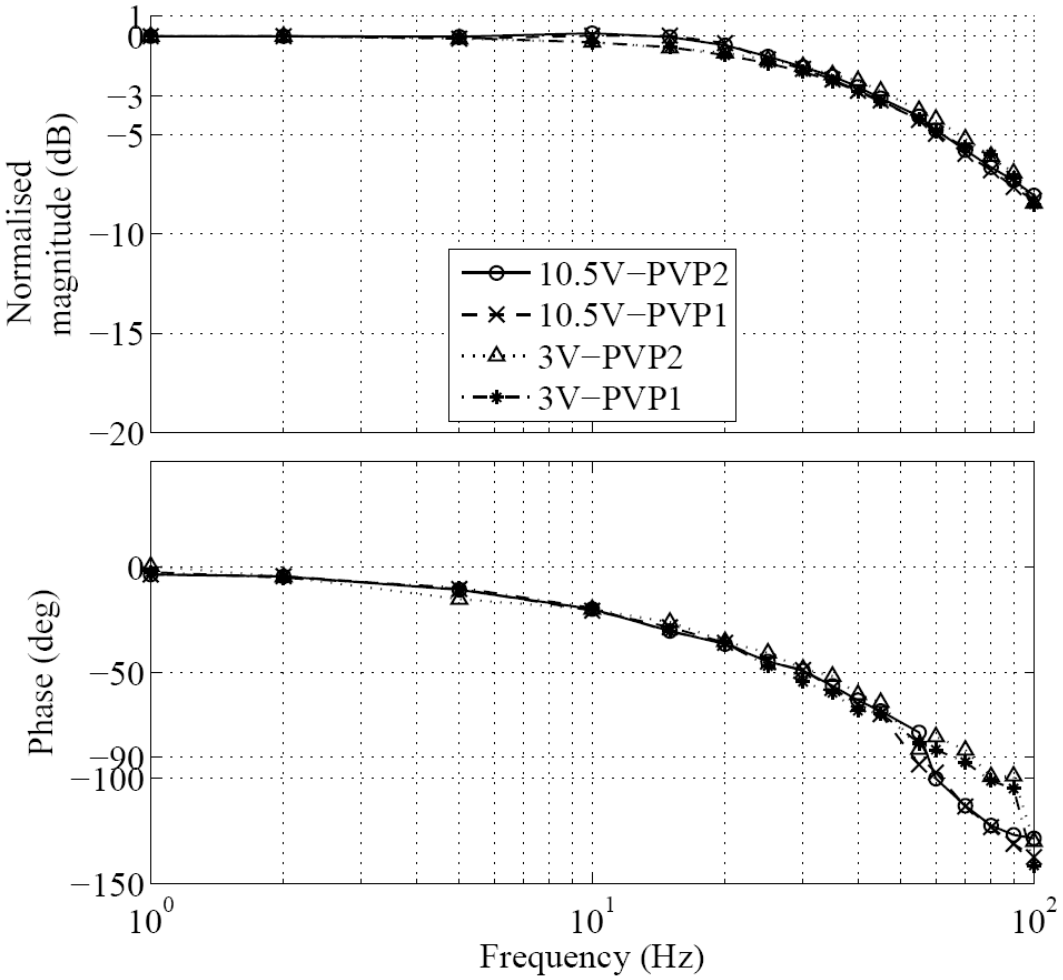

Figure 4.10: Comparison of normalised frequency response of the spool between PVP2 and PVP1 at varying applied voltages, at 140bar supply pressure

The frequency response test results at varying applied voltages are consistent for the two prototypes. The fastest response is observed at the small voltage demand. The -3dB bandwidth of PVP2 valve spool at 10.5V and 3.5V are at approximately 45Hz and 48Hz, respectively. The response of prototype PVP2 at small applied voltage amplitudes is approximately 7.5% lower than the simulation predictions. Overall, the simulation predictions are reasonably close to the PVP2 experiment results. This implies that the assumption of negligible pressure drop of the flow upstream to the control ports is reasonable. The marginally slower response of the prototype PVP1 could be primarily due to machining and assembly tolerance at the first stage. Nevertheless, the performances of the valves are consistent with the each other and the simulations. The analysis of the valve performance in relation to the donor valve is considered next.

4.7 Analysis of the valve performance in relation to the donor valve

The maximum spool displacement of the 26series donor valve [69] is ±0.508mm. A typical frequency response of a standard 26series servovalve at 210bar supply pressure is shown in Figure 4.11. The test fluid is MIL-H-5606. At 100% demand, the -3dB bandwidth of the valve is approximately 38Hz. The -90 degrees phase frequency is at approximately 75Hz. At 25% demand, the -3dB of the valve is approximately 110Hz and -90 degrees phase it at approximately 150Hz.

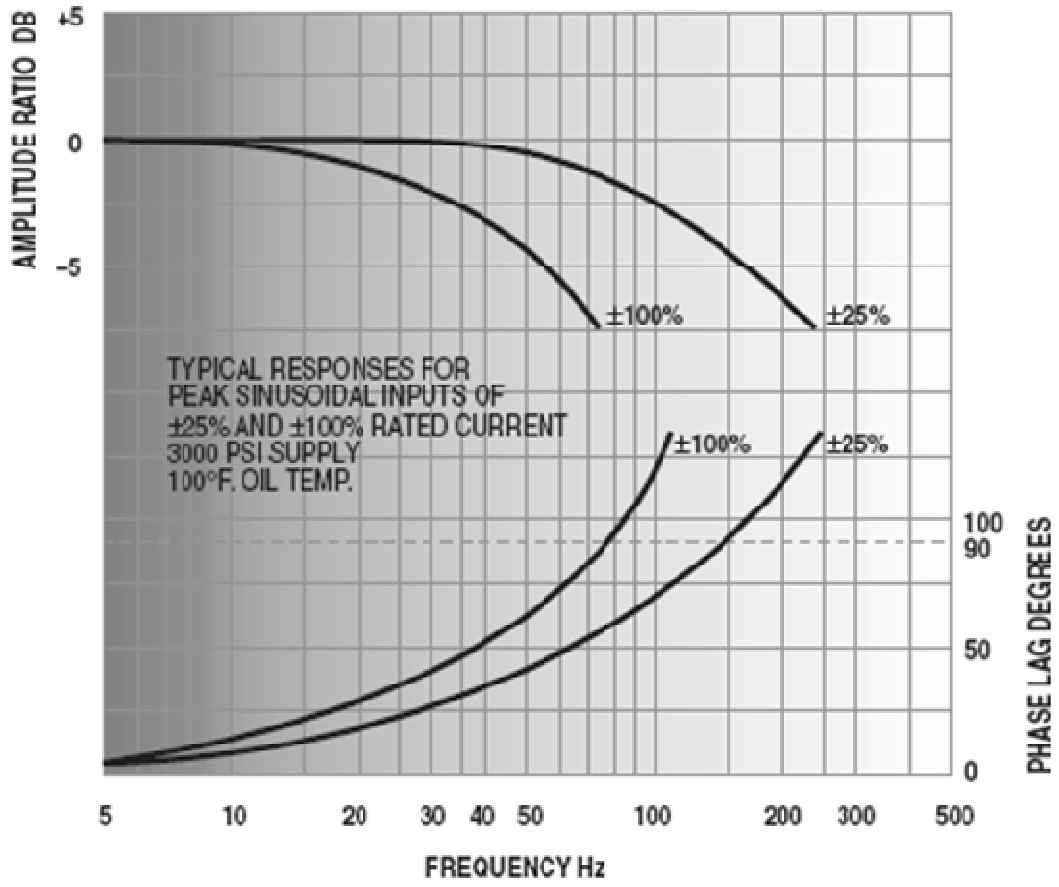

Figure 4.11: Frequency response of the 26 series donor valve at 210bar supply pressure [69]

The frequency response of the donor valve is significantly influenced by the demand. At maximum demand the deflector is at its maximum displacement causing flow saturations at the first stage. The feedback wire has to travel 0.508mm to generate the restoring torque to move the deflector back to its null position, in this condition. At 25% demand the spool travels 0.127mm to centralise the deflector. No flow saturation at the first stage occurs at this demand. This phenomenon can be observed in the substantial increase in the frequency response of the valve.

In contrast, the PHSV prototypes travel ±0.2mm at maximum demand. This is approximately 40% of the maximum displacement. The frequency responses of the PHSV prototypes are relatively constant with varying demand. This implies that there is no flow saturation at the first stage. Thus the deflector does not move its full

displacement. This implies that the force generated by the bimorph actuator is less than the torque motor.

Considering similar spool displacements, the PHSV frequency response is substantially smaller compared to the donor valve. The slower response of the PHSV spool is due to smaller spool velocities. The donor valve deflector travels a greater distance in relation to the PHSV, increasing the flow in the control ports and thus the spool velocity. This implies that the limited stroke of the deflector causes first stage flow limitations in the PHSV. It also implies that the bimorph actuator is stiffer compared to the torque motor assembly. Hence for a given deflector displacement, the spool of the PHSV has to travel further to centralise the deflector.

In order to meet the performance of the donor valve the bimorph force needs to be increased and the stiffness needs to be decreased. Increasing the length of the bimorph will reduce its stiffness and thus the second stage spool displacement. This will improve frequency response of the valve, however, the flow through the valve will be compromised (i.e. maximum spool displacement will be decreased). Increasing the length also reduces the bimorph tip force which will reduce the deflector displacement and thus the first stage flow. Decreasing the bimorph length will have the converse effect.

The first order linear model of the valve, discussed in section 3.7, showed that the frequency response and the steady state gain are influenced by the stiffness constants (section 3.2.4). These stiffness constants comprise the aforementioned parameters which influence the valve performance. Therefore the performance of the valve can be improved by optimising these constants. However, the donor valve was chosen for convenience and therefore it is not within the scope of this research to match the performance of the donor valve.

4.8 Conclusion

Two PHSV prototypes were built and tested. An equal area double-ended hydraulic actuator was connected to the PHSV prototype and tested under no-load conditions. The valve spool LVDT measurements were used to determine the spool frequency

response. The hydraulic actuator measurements were used to determine the flow through the valve and thus the frequency response of the valve flow. The performances of the two valves were consistent (8% difference at large input voltage amplitudes (22.5V) and 140bar supply pressure). The measured frequency responses of the valve spools were in close agreement with the simulation results (9% difference at large input voltage amplitudes (22.5V) and 140bar supply pressure). At 140bar supply pressure and 22.5V applied voltage the -3dB bandwidth of the valve was measured at approximately 41Hz. The flow frequency response was in close agreement with the valve spool response. This confirms that the response of the spool is a sufficient representation of the valve response.

The frequency response of the valve was influenced by the supply pressure. The supply pressure influences the pressure recovery in the control ports and thus the spool velocity. At 70bar supply pressure and maximum applied voltage amplitude (22.5V) the -3dB bandwidth of the valve dropped to 21Hz. Only marginal increase (17%) in valve performance was observed with decrease in applied voltage. At small applied voltages (3V) and maximum supply pressure (140bar) the frequency response of the valve increased to approximately 48Hz.

The hysteretic curve of the spool response was in close agreement with the simulation predictions. The valve spool response for a 0 to 30V applied voltage step at maximum supply pressure showed reasonably agreement with the simulation predictions. The simulations predictions were marginally faster (1ms at first time constant).

At low operating demands the -3dB bandwidth of the PHSV is approximately 30% of the donor valve bandwidth. This is because of flow limitations at the first stage resulting from relatively lower deflector displacements. In addition, the bimorph arrangement appears to be relatively stiffer compared to the torque motor assembly. This will compromise the frequency response of the PHSV due to greater spool travel.

At maximum demand the -3dB bandwidth of the two valves are similar, however, the spool stroke of the PHSV is approximately 40% of the donor valve. This is due to lack of deflector displacement. The force generated by the bimorph actuator is less than the torque motor.

The frequency response and the steady state gain of the PHSV are influenced by the stiffness constants of the bimorph-feedback wire assembly. Therefore, the performance of the valve can be improved by optimising these constants. However, the donor valve was chosen for convenience and therefore it is not within the scope of this research to match the performance of the donor valve.

Chapter 5

Optimisation of the PHSV performance

5.1 Introduction

In chapter 3, it was concluded that the bandwidth and the steady state gain of the valve were influenced by the stiffness constants of the bimorph-feedback wire assembly and the first stage flow force. In this chapter, these stiffness constants are expressed in terms of ratios between the forward and feedback path variables of the valve system. The performance of the valve is evaluated in terms of these ratios in a design trade-off plot. The design trade-off predictions are then compared to the nonlinear dynamic model simulations. To verify the design trade-off, a Mark-2 valve is developed and tested. The test results are compared to the nonlinear dynamic simulation results and the design trade-off plot predictions.

5.2 Evaluating the bandwidth of the valve

In Eq.(140) the bandwidth of the valve was expressed as

$$w_b = \frac{\frac{k_6}{\left(k_5 + K_{ff}\right)}\left(w_1 + w_2\right)}{A_s} \tag{140}$$

where w_1 and w_2 were given by Eq.(96) and Eq.(97), respectively. For a given supply pressure w_1 and w_2 will be constants. A_s is the cross sectional area of the second stage spool. Changes to the spool are beyond the scope of the project and thus A_s is considered to be a constant. Therefore, the variables which influence the bandwidth of the valve at a given operating condition are the stiffness constants k_5 and k_6 and the flow forces stiffness K_{ff}. These variables can be collectively expressed as

$$w_{br} = \frac{k_6}{(k_5 + K_{ff})} \tag{143}$$

where, w_{br} is the ratio which influences the bandwidth at a given supply pressure. k_5 and k_6 are given by Eq.(52) and Eq.(53), respectively as

$$k_5 = \frac{n_3}{k_3 n_2 - k_2 n_3} \tag{52}$$

$$k_6 = \frac{k_3}{k_3 n_2 - k_2 n_3} \tag{53}$$

Therefore w_{br}, can be expressed as

$$w_{br} = \frac{\frac{k_3}{k_3 n_2 - k_2 n_3}}{\left(\frac{n_3}{k_3 n_2 - k_2 n_3} + K_{ff}\right)} \tag{144}$$

Rearranging

$$w_{br} = \frac{k_3}{n_3 + K_{ff}(k_2 n_3 - k_3 n_2)} \tag{145}$$

where k_2, k_3, n_2 and n_3 were given by Eq.(33), Eq.(34), Eq.(45) and (46), respectively. These constants depend on the bimorph free length, L_b, bimorph flexural stiffness, $E_b I_b$, deflector guide length, L_d, feedback wire length L_f, and the feedback wire flexural stiffness $E_f I_f$. In the PHSV system the bimorph and deflector parameters are in the forward path and the feedback wire parameters are in the feedback path, as shown in Figure 5.1. In the bimorph-feedback wire arrangement, increasing the forward path variables have the same effect as reducing the feedback path variables and vice versa. Therefore it is convenient to express the stiffness constants in terms of ratios between the forward and feedback path variables. These

ratios are the bimorph to feedback wire length ratio, L_r, bimorph to feedback wire flexural stiffness ratio, k_r, and the deflector guide to feedback wire length ratio, L_{dr}. These ratios can be expressed as

$$L_r = \frac{L_b}{L_f} \tag{146}$$

$$k_r = \frac{E_b I_b}{E_f I_f} \tag{147}$$

And

$$L_{dr} = \frac{L_d}{L_f} \tag{148}$$

The ratios can be used to express the stiffness constants and subsequently be substituted into Eq. (140) to evaluate the bandwidth.

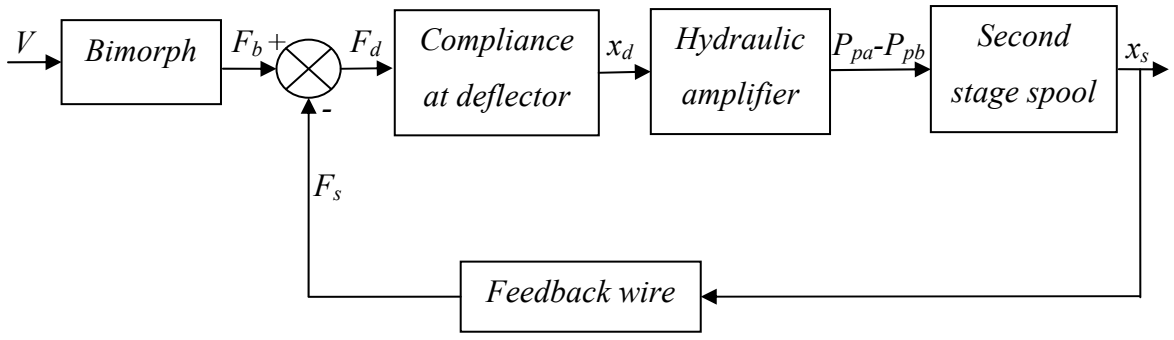

Figure 5.1: Block diagram of the PHSV system

5.2.1 Redefining the stiffness constants

A common factor in the stiffness constants k_2, k_3, n_2 and n_3 is

$$\frac{L_b}{2E_bI_b} \tag{149}$$

When k_2, k_3, n_2 and n_3 are divided by Eq.(149), Eq.(145) becomes

$$w_{br} = \frac{k_{31}}{n_3 + \frac{K_{ff}L_b(k_{21}n_{31} - k_{31}n_{21})}{2E_bI_b}} \tag{150}$$

Hence k_{21} can be expressed as

$$k_{21} = \left[\frac{2{L_b}^2}{3} + 2L_dL_b + 2{L_d}^2\right] \tag{151}$$

Multiplying by

$$\frac{{L_f}^2}{{L_f}^2} \tag{152}$$

And simplifying gives

$$k_{21} = {L_f}^2\left[\frac{2{L_r}^2}{3} + 2L_{dr}L_r + 2{L_{dr}}^2\right] \tag{153}$$

k_{31} can be expressed as

$$k_{31} = \left[\frac{2{L_b}^2}{3} + L_b\left(L_d + L_f\right) + 2L_d\left(L_d + L_f\right) + L_dL_b\right] \tag{154}$$

Multiplying by Eq.(152) and simplifying gives

$$k_{31} = {L_f}^2 \left[\frac{2{L_r}^2}{3} + (L_{dr} + 1)(L_r + 2L_{dr}) + L_{dr}L_r\right]$$

(155)

n_{21} can be expressed as

$$n_{21} = \left[\frac{2{L_b}^2}{3} + 2L_dL_b + 2{L_d}^2\right] + L_f(L_b + 2L_d)$$

(156)

Multiplying by Eq.(152) and simplifying gives

$$n_{21} = {L_f}^2 \left[\frac{2{L_r}^2}{3} + L_r + 2L_{dr} + 2L_{dr}L_r + 2{L_{dr}}^2\right]$$

(157)

n_{31} can be expressed as

$$n_{31} = \left[\frac{2{L_b}^2}{3} + L_b\big(L_d + L_f\big) + 2L_d\big(L_d + L_f\big) + L_dL_b\right] + L_f\left(L_b + 2\big(L_d + L_f\big)\right) + \frac{2E_bI_b{L_f}^3}{3E_fI_fL_b}$$

(158)

Multiplying by Eq.(152) and simplifying gives

$$n_{31} = {L_f}^2 \left[\frac{2{L_r}^2}{3} + (L_{dr} + 1)(L_r + 2L_{dr}) + L_{dr}L_r + \big(L_r + 2(L_{dr} + 1)\big) + \frac{2k_r}{3L_r}\right]$$

(159)

Another common factor that can be removed from the stiffness constants is L_f^2. Therefore, the constants can be expressed as

$$k_{22} = \left[\frac{2{L_r}^2}{3} + 2L_{dr}L_r + 2{L_{dr}}^2\right]$$

(160)

$$k_{32} = \left[\frac{2{L_r}^2}{3} + (L_{dr} + 1)(L_r + 2L_{dr}) + L_{dr}L_r\right] \tag{161}$$

$$n_{22} = \left[\frac{2{L_r}^2}{3} + L_r + 2L_{dr} + 2L_{dr}L_r + 2{L_{dr}}^2\right] \tag{162}$$

$$n_{32} = \left[\frac{2{L_r}^2}{3} + (L_{dr} + 1)(L_r + 2L_{dr}) + L_{dr}L_r + \big(L_r + 2(L_{dr} + 1)\big) + \frac{2k_r}{3L_r}\right] \tag{163}$$

Taking L_f^2 into consideration Eq.(150) can be expressed as

$$w_{br} = \frac{k_{32}}{n_{32} + \dfrac{K_{ff}{L_f}^2 L_b(k_{22}n_{32} - k_{32}n_{22})}{2E_bI_b}} \tag{164}$$

It is convenient to express w_{br} in terms of the feedback wire dimensions. This is because changes to the feedback wire are not within the scope of this study. Therefore

$$w_{br} = \frac{k_{32}}{n_{32} + \dfrac{K_{ff}{L_f}^3(k_{21}n_{31} - k_{31}n_{21})}{2E_fI_fk_r}} \tag{165}$$

Substituting for the stiffness constants, the bandwidth of the valve can be evaluated for varying length and flexural stiffness ratios.

5.3 Evaluating the steady state gain of the valve

Equation (138) shows that the steady state gain of the valve can be expressed as

$$K_{ss} = \frac{k_4}{k_6} \tag{138}$$

where, k_4 was given by Eq.(51)

$$k_4 = \frac{k_1 n_3 - k_3 n_1}{k_2 n_3 - k_3 n_2}$$

(52)

And k_6 was given by Eq.(53)

$$k_6 = \frac{k_3}{k_2 n_3 - k_3 n_2}$$

(53)

Substituting Eq.(51) and Eq.(53) into Eq.(138) and simplifying gives

$$K_{ss} = \frac{k_1 n_3 - k_3 n_1}{k_3}$$

(166)

Similar to the evaluation of bandwidth, it is convenient to express the stiffness constants in terms of the ratios shown in Eq.(146) – Eq.(148). k_1 was given by Eq.(32) as

$$k_1 = (L_b + 2L_d)\frac{3L_b d_{31}}{4h^2}$$

(32)

Multiplying by Eq.(152) and simplifying gives

$$k_1 = (L_r + 2L_{dr})\frac{3{L_f}^2 L_r d_{31}}{4h^2}$$

(167)

n_1 was given by Eq.(44) as

$$n_1 = k_1 + \frac{3d_{31}L_f L_b}{2h^2}$$

(44)

Multiplying by Eq.(152) and simplifying gives

$$n_1 = \frac{3{L_f}^2 L_r d_{31}}{4h^2}(L_r + 2L_{dr} + 2) \tag{168}$$

Similarly, k_3 and n_3 can be redefined in terms of the ratios and expressed as

$$k_3 = {L_f}^2\left[\frac{2{L_r}^2}{3} + (L_{dr} + 1)(L_r + 2L_{dr}) + L_{dr}L_r\right] \tag{169}$$

$$n_3 = {L_f}^2\left[\frac{2{L_r}^2}{3} + (L_{dr} + 1)(L_r + 2L_{dr}) + L_{dr}L_r + \big(L_r + 2(L_{dr} + 1)\big) + \frac{2k_r}{3L_r}\right] \tag{170}$$

Substituting the redefined stiffness constants into K_{ss}, the steady gain can be evaluated. Hence, the performance of the valve can be evaluated by generating design trade-offs comprising of bandwidth and steady state gain in terms of the length and flexural stiffness ratios.

5.4 Design evaluation for performance optimisation of the valve

The performance of the valve can be evaluated for various configurations of the bimorph-feedback wire assembly. Figure 5.2 shows the design trade-offs for the bandwidth and steady state gain of the valve at varying flexural stiffness ratio, k_r, and length ratio, L_r. k_r and L_r were given by Eq.(146) and Eq.(147), respectively. The length ratio of the deflector guide to the feedback wire, L_{dr}, is kept constant at 0.7, which is the value for the existing valve prototypes. The model was evaluated at 140bar supply pressure and the steady state gain is expressed as the maximum spool displacement, i.e. displacement with maximum applied voltage. Large values were used for k_r and L_r to analyse the variation in bandwidth and steady state gain.

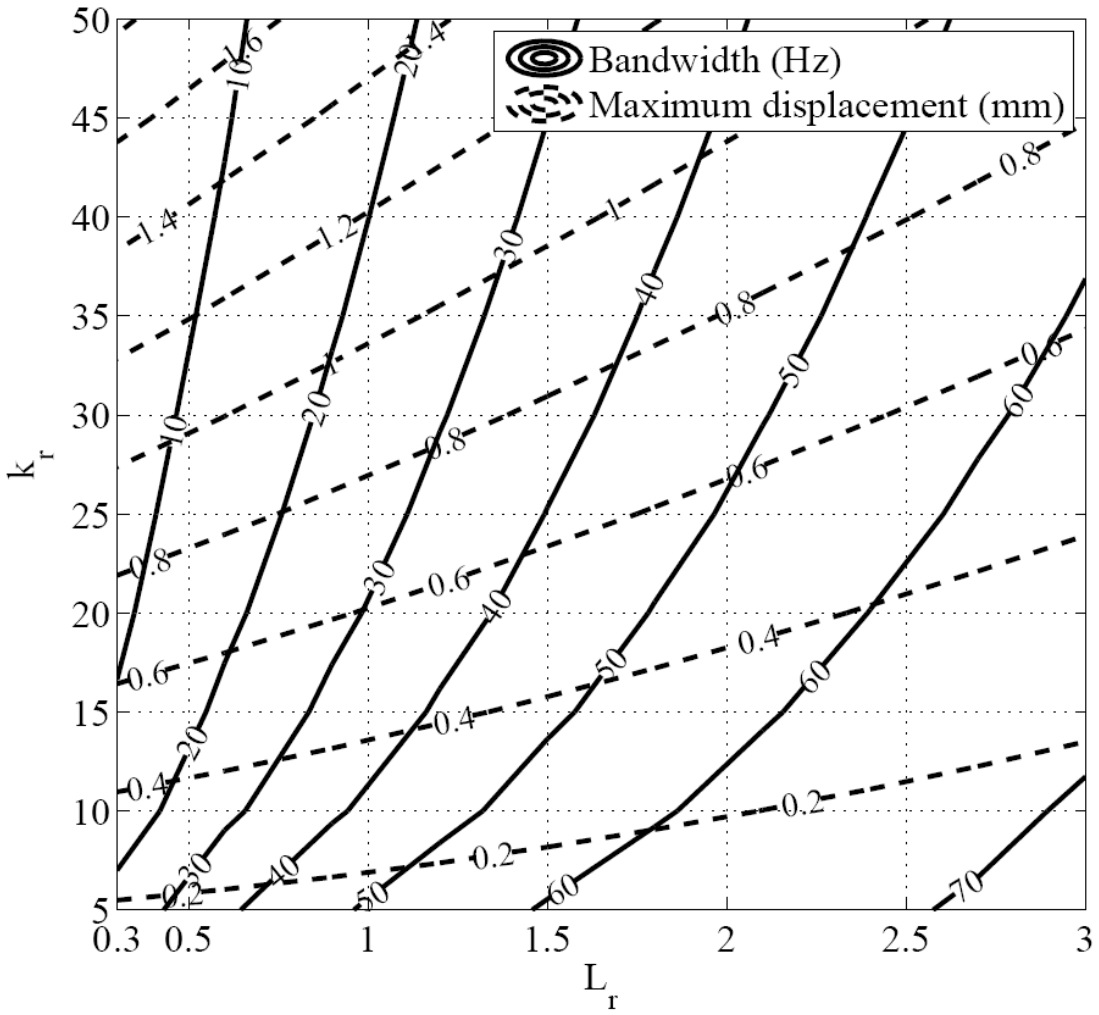

Figure 5.2: Design trade-off for the bandwidth and steady state gain at 140bar supply pressure and 30V applied voltage

For a given k_r, the bandwidth increases with L_r. Increasing L_r reduces the relative stiffness of the bimorph to the feedback wire. The spool travel (steady state gain) is reduced due to the relatively increased feedback wire stiffness. This reduces the time taken by the feedback wire to centralise the deflector. Hence the bandwidth is increased.

At a given L_r, the steady state gain increases with increasing k_r. Increasing k_r increases the relative stiffness of the bimorph to the feedback wire. The spool travel is increased due to the relatively low stiffness of the feedback wire. This increases the time required by the feedback wire to centralise the deflector. The bandwidth of the valve reduces. Increasing the stiffness of the bimorph will limit the bimorph tip

displacement and thus the deflector displacement. This will reduce the first stage flows, reducing the spool velocity and thus the bandwidth of the valve.

To understand the influence of flow force on the bandwidth Figure 5.2 was re-plotted without flow force. This is shown in Figure 5.3. At small values of L_r (<1) the response predicted by Figure 5.2 and Figure 5.3 are similar. For these values of L_r, the bimorph free length will be relatively short (<12mm). The force generated by the bimorph (>2.25N) is considerably bigger compared to the flow force (≈0.2N at 140bar pressure), discussed in section 3.4.1.1. Hence the influence of flow on the bandwidth of the valve is small.

At L_r values of about 2 the force generated by the bimorph is approximately 1N. The influence of flow force on the bandwidth will increase. This can observed by the reduced bandwidth in Figure 5.2 compared to Figure 5.3. A greater flow force will reduce the deflector displacement and thus the first stage flow in the control ports. This will reduce the velocity of the spool and therefore the valve bandwidth. Increasing L_r further will reduce the force generated by the bimorph further. Hence there is a limit to the increase in bandwidth with increase in bimorph length. In addition a long bimorph may introduce bimorph-feedback wire resonance issues.

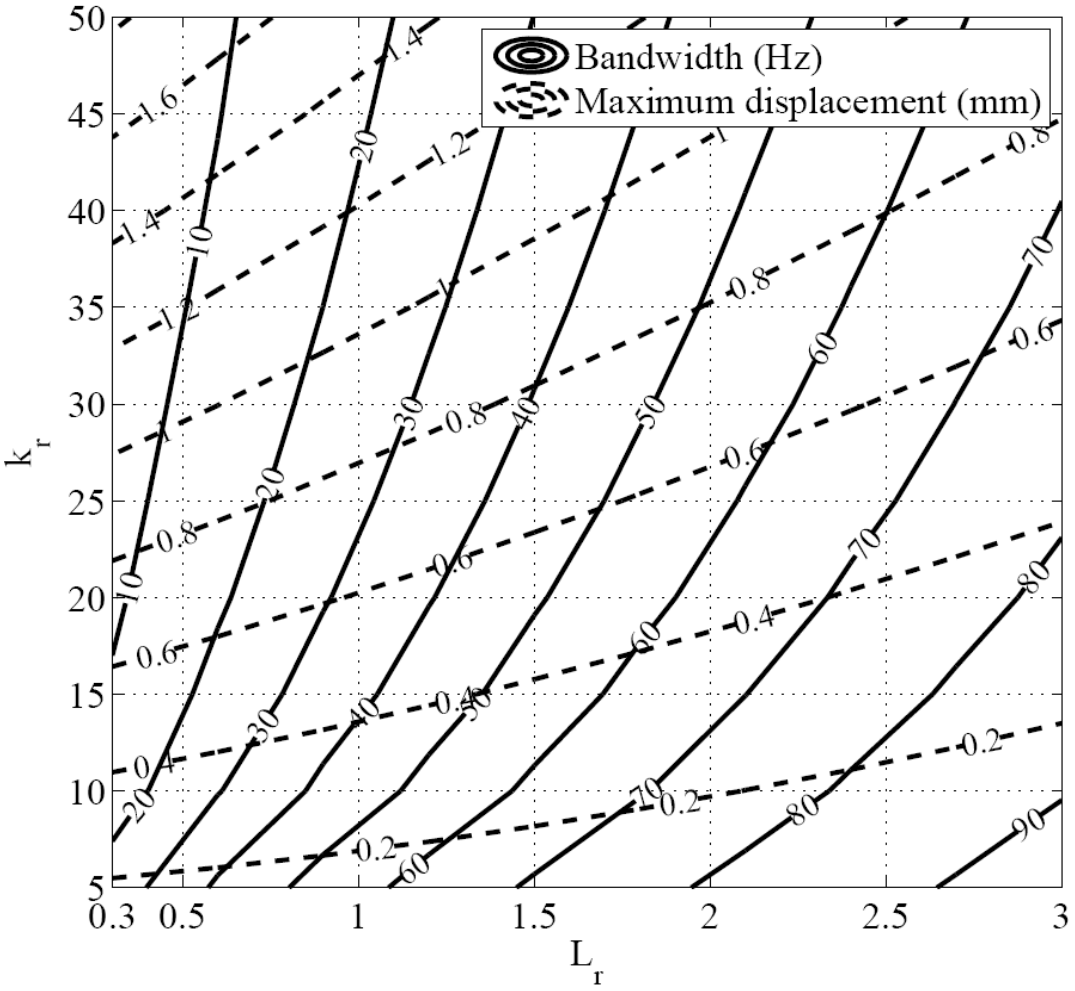

Figure 5.3: Design trade-off for the bandwidth and steady state gain at 140bar supply pressure and 30V applied voltage without flow force

Figure 5.4 shows the valve performance if L_{dr} is doubled. The operating conditions are identical to Figure 5.2. The influence of L_{dr} on the valve performance can be evaluated by comparing Figure 5.2 and Figure 5.4.

Doubling L_{dr} increases the bandwidth of the valve by approximately 10Hz. However, the steady state gain is reduced. The deflector guide length acts as an amplifier to the bimorph tip deflection. Therefore, increasing L_{dr} by increasing the deflector guide length, increases the deflector deflection. The increased deflector deflection for a given bimorph tip displacement, improves the flow in the control ports. The greater flow improves the spool velocity and thus the bandwidth of the valve spool. However, increasing the deflector guide length reduces the effective force at the

deflector, generated by the bimorph. Therefore the restoring force required by the feedback wire to centralise the deflector is reduced. Hence the spool travel is reduced. This reduces the steady state gain of the valve.

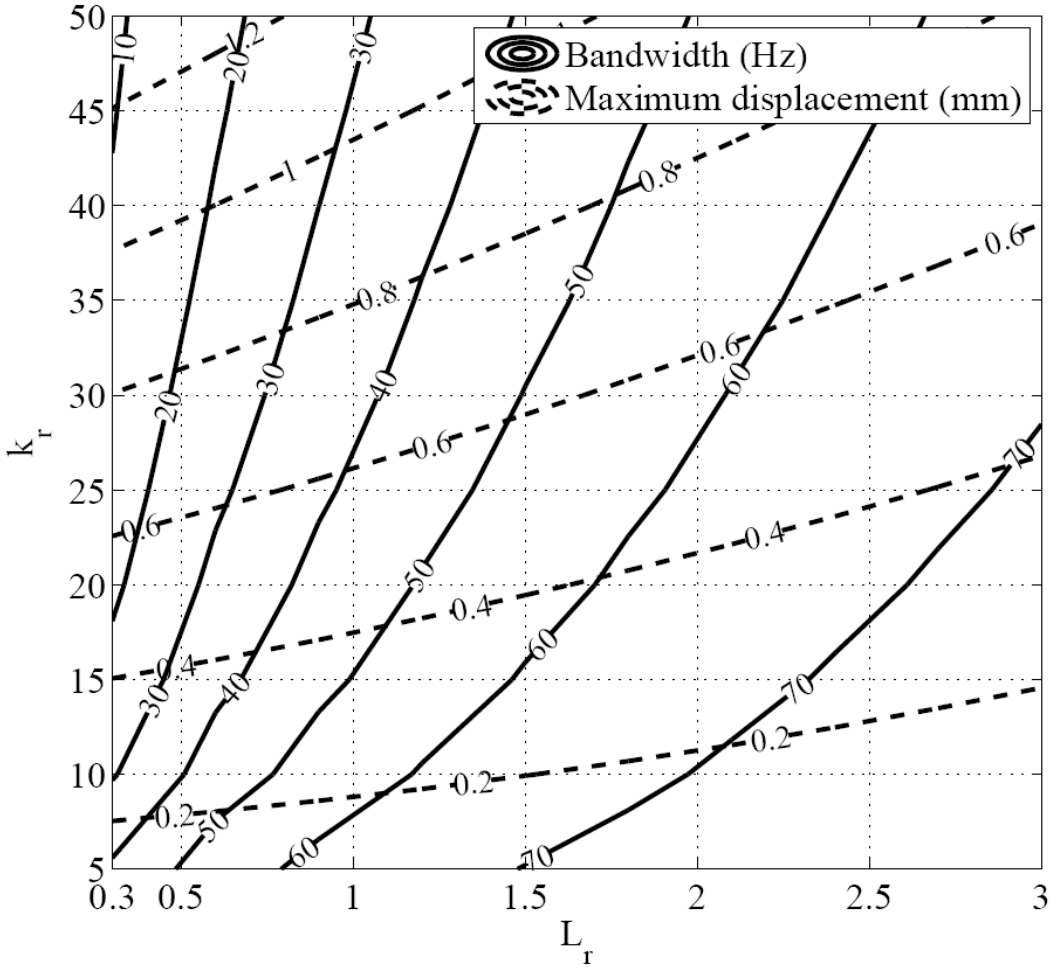

Figure 5.4: Design trade-off for the bandwidth and steady state gain at 140bar supply pressure and 30V applied voltage for double L_{dr}

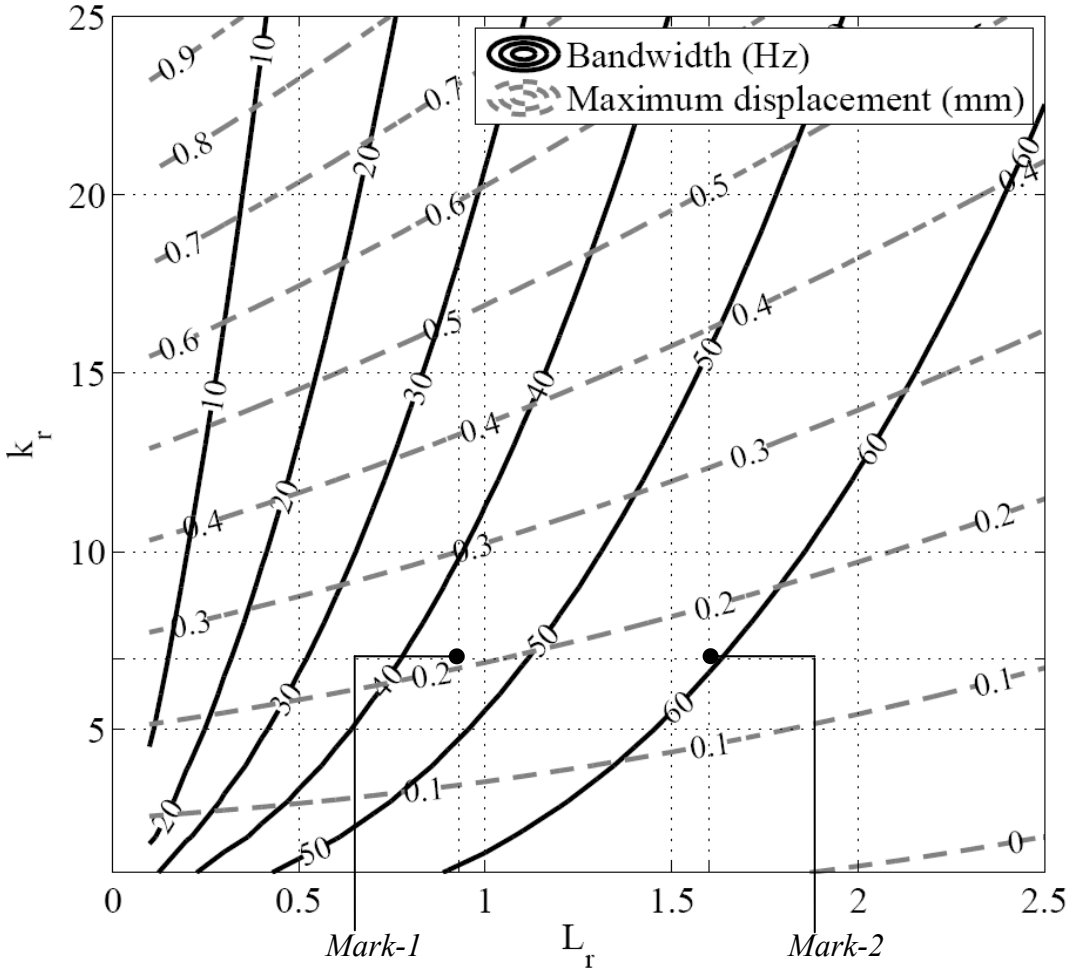

Figure 5.5: Scaled down design trade-off plot of the bandwidth and steady state gain at 140bar supply pressure and 30V applied voltage

For the Mark-1 PHSV prototypes L_r is approximately 0.93 and k_r is approximately 7. Figure 5.5 shows a scaled down design trade-off plot of Figure 5.2.

To improve the valve performance k_r can be increased by increasing the width or thickness of the bimorph or by reducing the radius of the feedback wire. The thickness of the bimorph can be increased by bonding two actuators one on top of the other. For fixed feedback wire dimensions and bimorph width, doubling the thickness increases k_r to approximately 56. For Mark-1 prototype bimorph length, this reduces the bandwidth of the valve to approximately 14Hz (see Figure 5.2). The steady state gain is increased to approximately 1.7mm.

To achieve the 45Hz predicted bandwidth of Mark-1 prototype, L_r needs to be approximately 2.5. The steady state gain reduces to approximately 1mm. To limit the spool stroke to its maximum, 0.5mm, L_r needs to be increased to approximately 6. This increases the bandwidth to approximately 77Hz. With the existing feedback wire, this requires the bimorph free length to be approximately 78mm. This increases the complexity of the design and oversizes the valve.

Alternatively, bimorphs can be bonded side by side to improve *kr*. Pair of bimorphs increase *kr* to approximately 14. 45Hz bandwidth can be achieved by increasing L_r to approximately 1.3 (see Figure 5.5). The steady state gain of the valve is increased to 0.37mm. The first stage design changes required to accommodate two bimorphs side by side are substantial relative to the initial prototype. The much wider first stage body poses mounting issues on the amplifier body (see section 2.7).

To validate the design trade-offs another point on the curve needs to be verified. A convenient approach is to use a longer free length of the existing bimorph. *kr* will remain unchanged at approximately 7 and L_r will increase. This will increase the bandwidth of the valve, however, the steady state gain will be compromised.

The length of the PL127.10 actuator discussed in section 2.5.3 is 31mm. Choosing a clamping length of 10mm and a overhanging length of 1mm for the electrodes, the free length of the bimorph can be increased to 20mm. This increases L_r to approximately 1.6. A Mark-2 prototype can be built and tested for this bimorph specification. The bandwidth and the steady state gain of the Mark-2 valve are expected to be approximately 59Hz and 0.16mm, at 140bar supply pressure and 30V applied voltage (see Figure 5.5). Prior to building the valve, the valve performance is simulated using the nonlinear dynamic model. The following section discusses the simulation results.

5.5 Simulating the Mark-2 PHSV performance

To compare the steady state design trade-off results, the nonlinear analytical model of the valve is simulated with the Mark-2 bimorph dimensions. Figure 5.6 shows the frequency response plot for the valve at 140bar, 100bar and 70bar supply pressures. The applied voltage amplitude is kept constant at 30V.

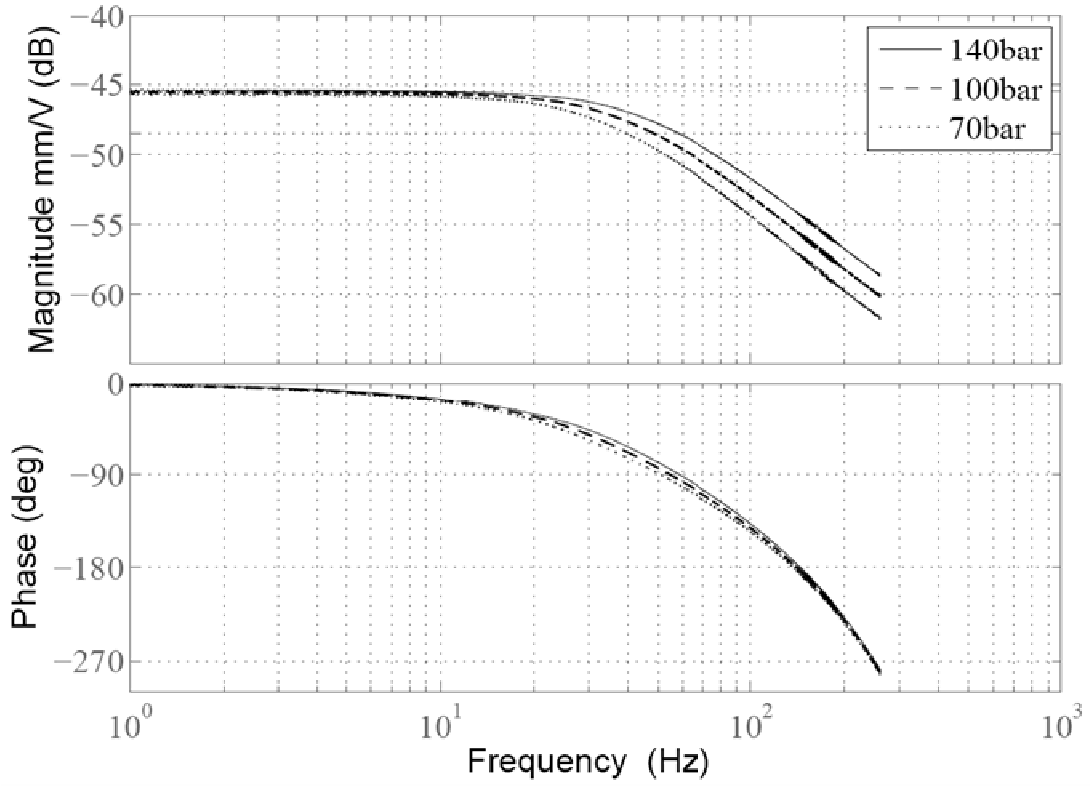

Figure 5.6: Nonlinear frequency response data simulated for Mark-2 valve at 30V applied voltage amplitude

The -3dB bandwidth of the valve at 140bar supply pressure is approximately 59Hz and -90 degrees phase frequency is at approximately 60Hz. The bandwidth is in 100% agreement with the design trade-off prediction. At 100bar and 70bar supply pressure the -3dB bandwidth of the valve reduces to approximately 49Hz and 40Hz, respectively. The -90 degrees phase at 100bar and 70bar supply pressures are at approximately 55Hz and 50Hz, respectively.

The low frequency line on the bode plot in Figure 5.6 is at approximately -45.5dB. Thus the low frequency magnitude is 5.31×10^{-3}mm/V. At 30V applied voltage the amplitude of the spool displacement is approximately 0.16mm. This is in 100% agreement with the design trade-off prediction. The valve spool bandwidth and the steady state gain predictions are consistent between the linear and the nonlinear models. Having verified the design trade-off predictions with the nonlinear dynamic simulation results, the Mark-2 prototype is built and tested.

5.6 Experiment results of the Mark-2 PHSV

5.6.1 Comparison of experiment results to simulations

The experiment set up used for the initial prototype was used to test the Mark-2 valve performance. The frequency response of the spool position of Mark-2 valve is compared to the nonlinear simulation discussed in results in Figure 5.7. The operating conditions are 140bar supply pressure and 22.5V applied voltage amplitude.

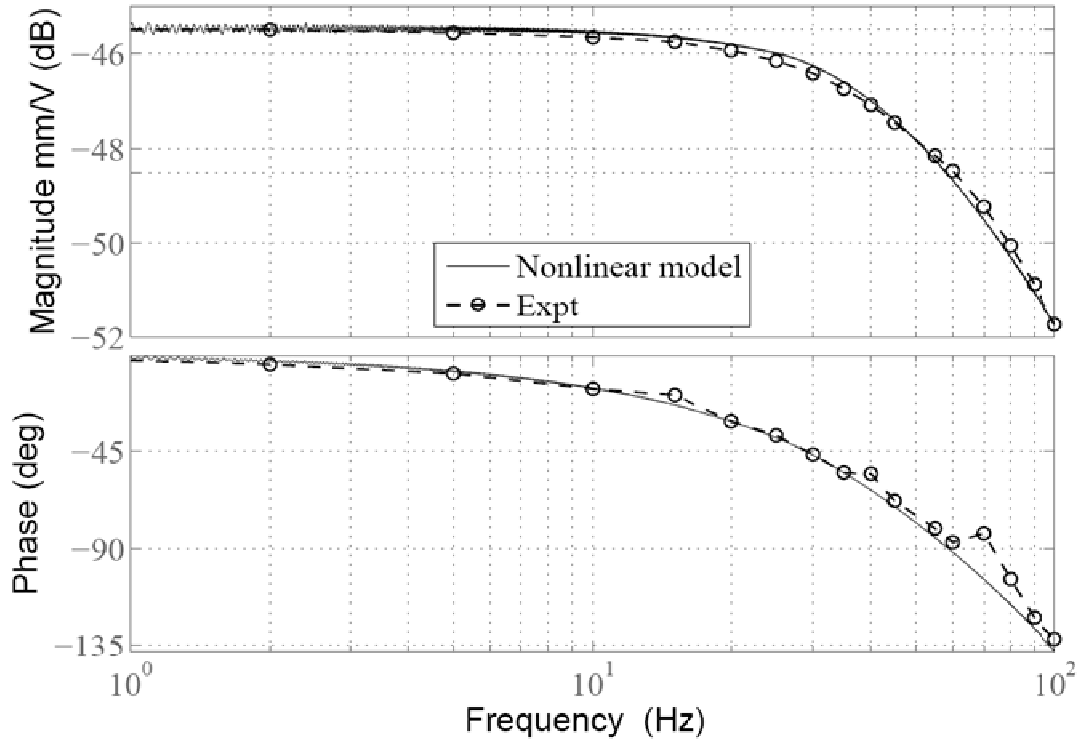

Figure 5.7: Comparison of experiment and nonlinear simulation frequency response of the Mark-2 valve spool at 140bar supply pressure and 22.5V applied voltage amplitude

Figure 5.7 shows close agreement between the experimental and simulated frequency response of the Mark-2 valve spool. The trend of the measured frequency response has been predicted well by the simulations. The -3dB bandwidth of the experiment results is approximately 60Hz. This is approximately 1.6% higher than the design trade-off predictions. The -90 degrees phase frequency of the measured response cannot be determined with reasonable accuracy due to the high noise to signal ratio in the measurements at higher frequencies. Nevertheless, the trend at the lower frequencies is close with simulations.

Figure 5.8 compares the experiment spool displacement to simulation results at 1Hz operating frequency. The supply pressure is 140bar and the applied voltage amplitude is 22.5V.

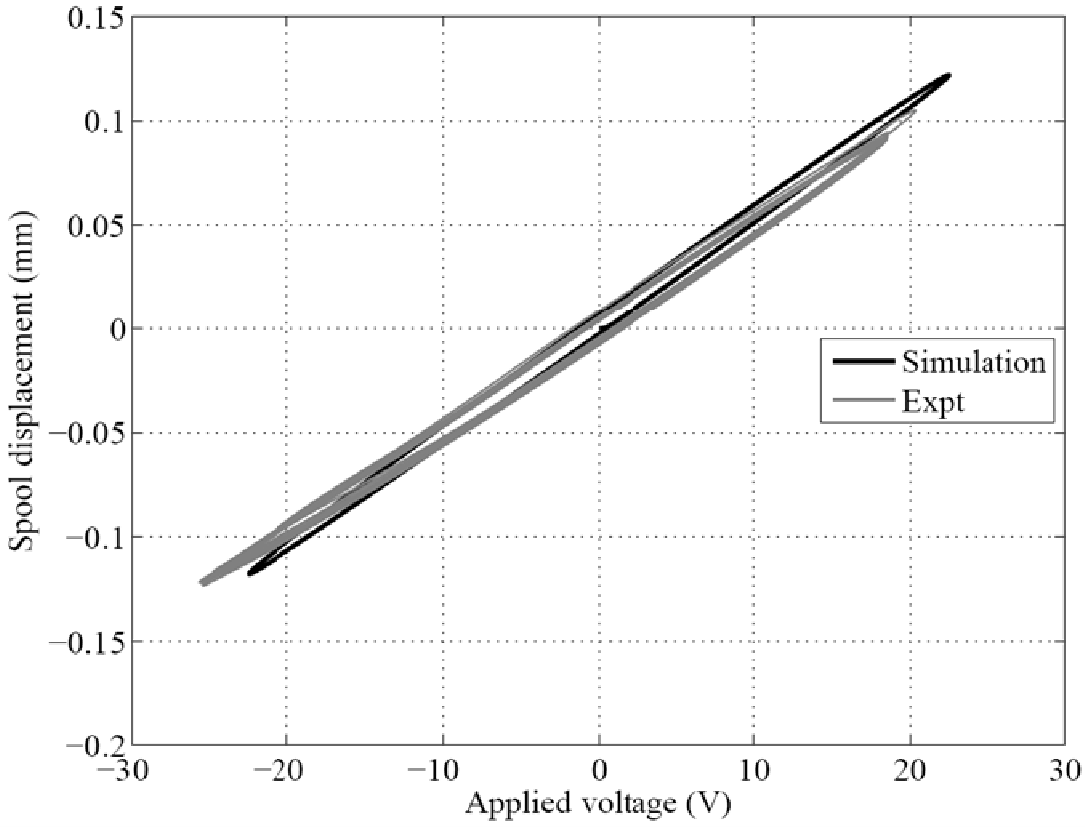

Figure 5.8: Comparison of measured and simulated spool displacement at 140bar supply pressure and 22.5V applied voltage amplitude

The predicted stroke of the valve spool at 22.5V applied voltage amplitude is approximately 0.24mm. The measured spool stroke is 4% greater than the simulation predictions. The shape and trend of the measured and simulated hysteretic curves are in good agreement. The hysteresis of the valve spool can be measured from Figure 5.8 to be approximately ±2%. This is 50% of the hysteresis observed for the initial prototype.

The bimorph hysteresis is proportional to the applied voltage and tip displacement. The spring force generated by the feedback wire on the bimorph is relatively higher than that for the initial prototype. In addition the longer bimorph generates a smaller blocking force. The force limitation can limit the bimorph tip displacement. The reduced bimorph displacement reduces the influence of the hysteretic nonlinearity on the bimorph response.

5.6.2 Frequency response of the Mark-2 valve spool for varying applied voltages

Figure 5.9 shows the normalised frequency response of the valve spool for varying applied voltages at 140bar supply pressure. As expected, the frequency response of the valve spool is consistent with applied voltage. The nonlinearities are much less pronounced in the Mark-2 valve results compared to the initial prototypes. This could be a result of the first stage flow nonlinearities having a smaller influence due to the reduced deflector displacements.

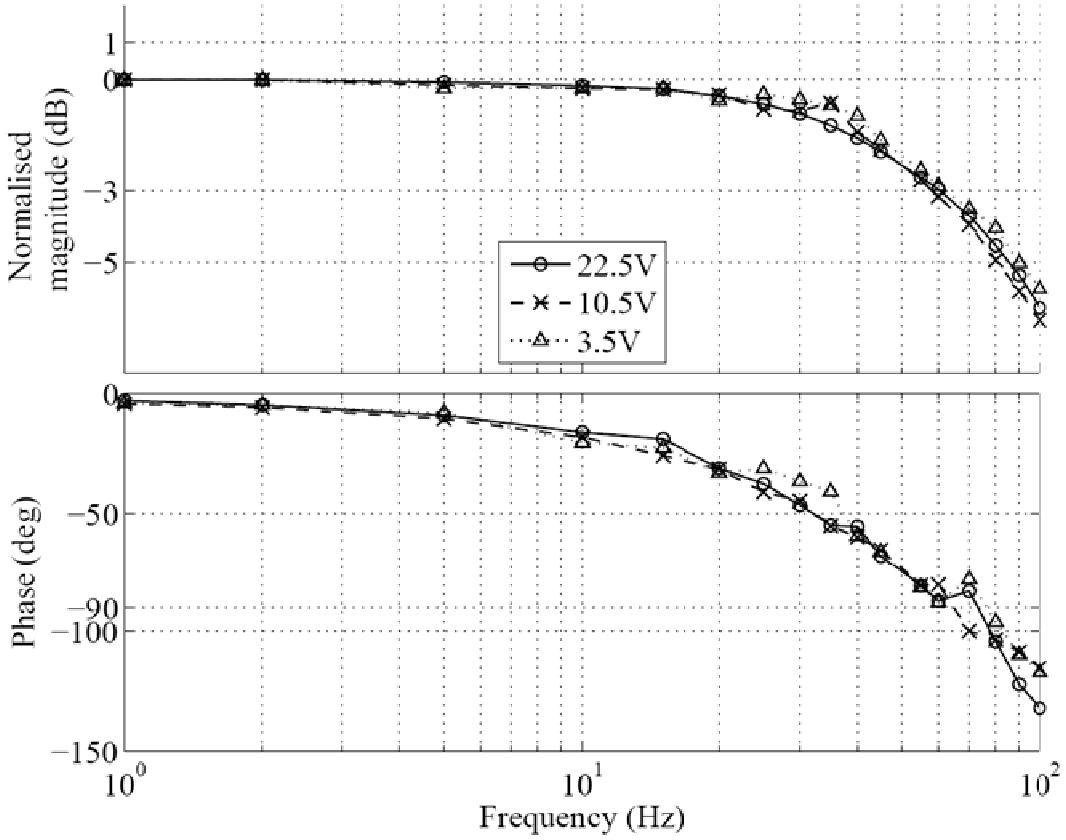

Figure 5.9: Normalised frequency response of the Mark-2 valve spool for varying applied voltages at 140bar supply pressure

5.6.3 Frequency response of the Mark-2 valve spool for varying supply pressures

Figure 5.10 compares the normalised frequency response of the Mark-2 valve spool at 140bar, 100bar and 70bar supply pressures. The amplitude of the applied voltage is kept constant at 22.5V.

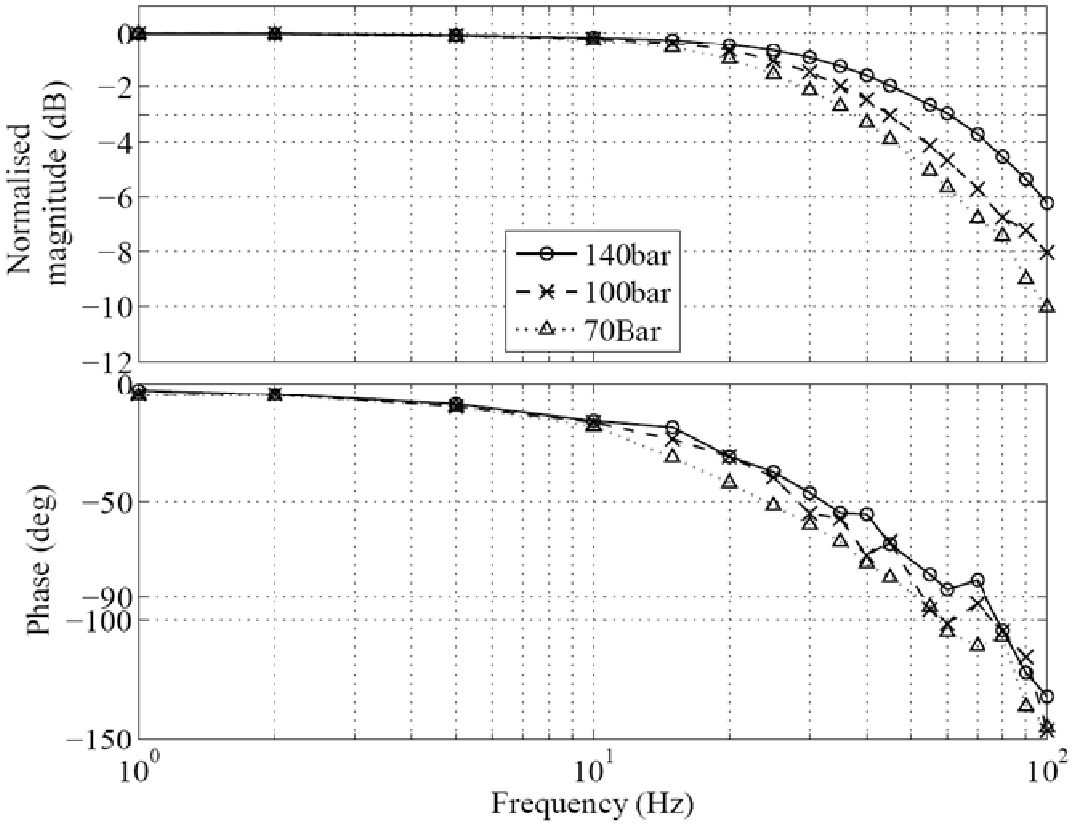

Figure 5.10: Normalised frequency response of the Mark-2 valve spool for varying supply pressures at 22.5V applied voltage amplitude

Similar to the initial prototype frequency response measurements, the response is proportional to the supply pressure. The -3dB bandwidth of the Mark-2 valve spool at 100bar supply pressure is 45Hz. This is 6.7% lower than the nonlinear simulation predictions. The -3dB bandwidth at 70bar supply pressure is approximately 38Hz. This is approximately 5% lower than the nonlinear simulation predictions. The high noise to signal ratio in the measurements of the phase response makes it impractical to measure -90 degree phase frequency. Nevertheless, the trend is in good agreement with the simulated results at lower frequencies.

The experiment results of the Mark-2 valve and the simulation results of the nonlinear dynamic model are in good agreement with the design trade-off predictions. Therefore, the design trade-off can be used to optimise the valve performance to meet a specified bandwidth and steady state gain. The bimorph, deflector guide and the feedback wire can be sized to meet a specific performance requirement. From Figure 5.4, the optimum performance for the valve for a reasonable bimorph length is 60Hz bandwidth at ±0.5mm spool displacement. At this operating point L_r is approximately 2.1, k_r is approximately 28 and L_{dr} is 1.4.

The optimum PHSV performance is lower than the donor valve performance. This is due to lack of deflector displacement at the first stage. The deflector displacement is limited by the blocking force of the bimorph actuator. If a bimorph with greater force capability is used then the deflector displacement will increase. This will improve the first stage flows and thus the bandwidth of the valve. The greater deflector travel will also increase the spool displacement. Alternatively, the feedback wire can be replaced by electronic feedback. This would require the bimorph to overcome only the first stage flow forces. Since these forces are small a greater deflector displacement can be achieved.

5.7 Conclusion

To evaluate the bimorph-feedback wire assembly design trade-offs the stiffness constants that determine the bandwidth and steady state gain of the valve were expressed in terms of ratios between the forward and feedback path variables of the

valve system. Subsequently, the bandwidth and the steady state gain of the valve were expressed in terms of these ratios. These ratios were k_r, L_r and L_{dr}. The performance of the valve was evaluated in terms these ratios.

The bandwidth of the valve increased with increasing L_r. A longer bimorph improved the response of the valve. However, the steady state gain of the valve reduced with increasing L_r. Increasing k_r increased the steady state gain, however, the bandwidth of the valve was compromised. To improve the valve performance both L_r and k_r need to be increased. Increasing L_{dr} improved the bandwidth of the valve, however, compromised the steady state gain.

Increasing L_r by increasing the bimorph length to improve the bandwidth of the valve is limited by the flow force at the deflector. At long bimorph free lengths (>25mm) the flow force influence becomes significant due to drop in force generated by the bimorph. In addition a long bimorph may introduce bimorph-feedback wire assembly resonance issues.

To validate the design trade-off results, a Mark-2 prototype was developed by choosing a convenient point on the plot. The free length of the bimorph was increased to 20mm. At 140bar supply pressure and 30V applied voltage amplitude, the predicted bandwidth and steady state gain of the valve spool were 59Hz and 0.16mm, respectively. To compare the design trade-off results, the nonlinear dynamic model was simulated with the revised bimorph dimensions. The simulated results were in 100% agreement with the design trade-off results.

From experiment results of the Mark-2 valve, the -3dB bandwidth of the valve at 140bar supply pressure and 22.5V applied voltage amplitude was measured at approximately 60Hz. At the same applied voltage amplitude the -3dB bandwidth of the valve 70bar supply pressure dropped to 38Hz. These are approximately 1.6% and 5% different to the nonlinear simulation predictions, respectively. The trend of the experiment bode plots are also in good agreement with the simulations. The response of the valve was consistent with varying applied voltage amplitudes.

The measured spool stroke was in close agreement with the simulation predictions (4% difference). At maximum applied voltage amplitude the spool stroke was approximately 0.24mm. The hysteresis of the valve was approximately ±2%.

The experiment results and the nonlinear simulation results of the Mark-2 valve are in close agreement with the design trade-off predictions. Therefore the design trade-off model can be used to optimise the performance of the PHSV. The dimensions of the bimorph, deflector guide and the feedback wire can be sized to meet a specified valve performance.

The optimum PHSV performance is lower than the donor valve performance. This is due to lack of deflector displacement at the first stage. The deflector displacement is limited by the blocking force of the bimorph actuator. If a bimorph with greater force capability is used then the deflector displacement will increase. This will improve the first stage flows and thus the bandwidth of the valve. The greater deflector travel will also increase the spool displacement. Alternatively, the feedback wire can be replaced by electronic feedback. This would require the bimorph to overcome only the first stage flow forces. Since these forces are small a greater deflector displacement can be achieved.

Chapter 6

Conclusions and future work

6.1 Conclusions

High performance hydraulic servo systems use servovalves as the primary power modulation unit. The dynamic response of these valves influences the overall system performance. In two stage servovalves the first stage actuator response is known to be the dominant factor influencing the overall valve performance. In recent years researchers have improved the performance envelopes of servovalves by using active material actuators at the first stage.

In this research a novel first stage actuator assembly fitted to a conventional deflector jet servovalve was investigated. The torque motor assembly in the first stage was replaced by a multilayered bimorph actuator. A mechanical feedback wire was used for proportional flow control. The bimorph was directly coupled to the feedback wire for submerged operation. This considerably simplified the first stage assembly and reduced the part count which could lead to potential cost savings.

To analyse the bimorph-feedback wire assembly, a steady state analytical model was developed. This model was used to derive the stiffness constants influencing the deflector and the valve spool. An FEA model of the assembly was developed to compare the analytically derived stiffness constants. The results between the two models were within 5% difference. The first stage flow forces at the deflector were determined using CFD analysis. The CFD model was validated using existing experimental data. From the CFD model it was found that the flow force was proportional to the pressure drop across the deflector and the deflector displacement.

The derived stiffness constants and the first stage flow force were used to develop and simulate a high order nonlinear model of the valve. A Bouc-Wen hysteresis

model was developed to determine the hysteretic characteristic of the valve. Hysteresis of ±4% was predicted at the spool.

The nonlinear dynamic model was linearised to establish the most important parameters that influence the frequency response and the steady state gain of the valve. The frequency response of the linearised model was in close agreement with that of the nonlinear model. The -3dB bandwidths predicted by the two models is compared in Table 6-1.

The higher order linear model was reduced to a first order lag system. The frequency response of this reduced model is in close agreement with higher order linear model and the nonlinear dynamic model. The system parameters that influence the pole at the first break frequency of the higher order models are the steady state stiffness constants k_5 and k_6 and the deflector flow force F_f. The steady state gain of the valve spool is proportional to the ratio k_4/k_6. k_4 and k_6 are the constants of proportionality giving the force at the deflector generated due to the applied voltage and spool displacement, respectively, when the deflector is held in its null position. k_5 is the deflector stiffness when the spool is held in its null position.

Two initial Mark-1 prototype PHSVs were built and tested. The -3dB bandwidth and the spool stroke are compared to the simulation predictions in Table 6-1 and Table 6-2, respectively. The hysteresis (±4%) of the second stage spool was also in close agreement with the simulation results.

The frequency response of the valve was influenced by the supply pressure. The supply pressure influences the pressure recovery in the control ports and thus the spool velocity. Reducing the supply pressure from 140bar to 70bar reduced the -3dB bandwidth of the valve by approximately 50%. At small applied voltages the -3dB bandwidth of the valve spool increased by approximately 17%.

	P_s=140bar, V=22.5V	P_s=100bar, V=22.5V	P_s=70bar, V=22.5V	P_s=140bar, V=3V
Nonlinear model	*45Hz*	*37.5Hz*	*32.3Hz*	*52Hz*
Higher order linear model	-	-	-	*52Hz*
first order model	-	-	-	*45Hz*
PVP1 experiment results	*38Hz*	*29Hz*	*16Hz*	*44Hz*
PVP2 experiment results	*41Hz*	*36Hz*	*21Hz*	*48Hz*

Table 6-1: Comparison of -3dB bandwidths for Mark-1 prototype

	V=30V
Nonlinear model	*±0.2mm*
Higher order linear model	*±0.19mm*
first order model	*±0.2mm*
PVP1 experiment results	*±0.21mm*

Table 6-2: Comparison of spool displacement for Mark-1 prototype

At low operating demands the -3dB bandwidth of the PHSV is approximately 30% of the donor valve bandwidth. This is because of flow limitations at the first stage resulting from lower deflector displacements. In addition, the bimorph arrangement is stiffer compared to the torque motor assembly. This will compromise the frequency response of the PHSV as more spool travel is required to recentralise the deflector. At maximum demand the frequency response of the two valves are similar, however, the spool stroke of the PHSV is approximately 40% of the donor valve. This is due to lack of deflector displacement. The force generated by the bimorph actuator is less than the torque motor. However, the donor valve was chosen for convenience and therefore it is not the objective of this research to match the performance of the donor valve.

Design trade-offs for the bimorph-feedback wire assembly were investigated to improve the Mark-1 valve performance. The bandwidth of the valve increased with

increasing bimorph to feedback wire length ratio. However, this reduced the steady state gain of the valve. Increasing the bimorph to feedback wire flexural stiffness ratio increased the steady state gain, but the bandwidth of the valve was reduced. To improve the valve performance both these ratios need to be increased. Increasing the deflector guide to feedback wire length ratio improved the bandwidth of the valve, however, reduced the steady state gain.

Increasing the bimorph length to improve the bandwidth of the valve is limited by the flow force at the deflector. At long bimorph free lengths (>25mm) the flow force influence becomes significant due to drop in force generated by the bimorph. In addition a long bimorph may introduce bimorph-feedback wire assembly resonance issues.

A Mark-2 prototype valve was developed and tested to validate the design trade-off predictions. The free length of the bimorph, in the Mark-2 model, was increased from 12mm to 20mm. The -3dB bandwidth of the Mark-2 valve spool at 140bar supply pressure and 22.5V applied voltage amplitude was measured at approximately 60Hz. This is within 2% of the nonlinear simulation results and the design trade-off predictions. The trend of the experiment bode plots are also in good agreement with the simulations. The -3dB bandwidth of the valve was consistent with varying applied voltage.

The measured spool stroke was 4% greater than the simulation predictions. At 22.5V applied voltage amplitude the spool stroke was approximately 0.24mm. The hysteresis of the valve was approximately ±2%.

The experiment results and the nonlinear simulation results of the Mark-2 valve are in close agreement with the design trade-off predictions. Therefore the design trade-off plots can be used to optimise the performance of the PHSV. The dimensions of the bimorph, deflector and the feedback wire can be sized to meet a specified valve performance.

The optimum PHSV performance is lower than the donor valve performance. This is due to lack of deflector displacement at the first stage. The deflector displacement is

limited by the blocking force of the bimorph actuator. If a bimorph with greater force capability is used then the deflector displacement will increase. This will improve the first stage flows and thus the bandwidth of the valve. The greater deflector travel will also increase the spool displacement. Alternatively, the feedback wire can be replaced by electronic feedback. This would require the bimorph to overcome only the first stage flow forces. Since these forces are small a greater deflector displacement can be achieved.

6.2 Future work

The main areas for consideration are

i. Performing further tests with the prototypes to characterise the performance for vibration sensitivity, temperature sensitivity and life.

ii. Performing structure/fluid interaction simulations to assess first stage damping.

iii. Revising the coupling of the bimorph to the feedback wire assembly to reduce stress concentrations.

iv. Consider developing the bimorph and deflector as a single unit.

v. Introducing adjustability in the first stage design to compensate for assembly misalignments.

vi. Revising the clamping technique of the bimorph so that it can be replaced or serviced if desired.

vii. Optimising valve performance using genetic algorithm to generate a Pareto front.

References

1. **Norvelle, F.D.** 1995. Fluid Power Technology. s.l. : West Publishing, ISBN: 0314012184.

2. **Reichert, M.** 2006. Development of a Piezo-Driven Pilot Stage for Highly Dynamic Hydraulic Valves. 5th International Fluid Power Conference. Vol. 2, pp. 127-137.

3. **Karunanidhi, S and Singaperumal, M.** 2010. Mathematical Modelling and Experimental Characterization of a High Dynamic Servovalve Integrated with Piezoelectric Actuators. Proceedings of the Institution of Mechanical Engineers, Part1: Journal of Systems and Control Engineering. pp. 419-435.

4. **Li, S. and Song, Y.** 2007. Dynamic Response of a Hydraulic Servovalve Torque Motor with Magnetic Fluids. Mechatronics, pp. 442-447.

5. **Uchino, K. and Giniewicz, J. R.** 2003. Micromechatronics. New York : Marcel Dekker, pp. 242-254.

6. **Gordic, D., et al.** 2008. Effects of the Variation of Torque Motor Paramters on Servovalve Performance. Journal of Mechanical Engineering, Vol. 54, pp. 866-873.

7. **John, Shaju, et al.** 2007. Comparison of Piezoelectric, Magnetostricitve and Electrostricitve Hybrid Hydraulic Actuators. Journal of Intelligent Material Systems and Structures, Vols. 0-2007.

8. **Prechtl, E. and Hall, S.** 1999. Design of a High Efficiency, Large Stroke Electromechanical Actuator. Smart Material and Structures, Vol. 8, pp. 13-30.

9. **Yi, T., Cornwell, M. and Gutmark, E. J.** 2005. Mean Flow Regulation of a High Frequency Combustion Control Valve Based on Pulse Width Modulation and System Identification. American Control Conference. pp. 1132-1137.

10. **Lam, A. H. and Liao, W.** 2003. Semi-Active Control of Automotive Suspension Systems with Magneto-Rheological Dampers. International Journal of Vehicle Design, Vol. 33, pp. 50-75.

11. **Shoji, S. and Esashi, M.** 1994. Microflow Devices and Systems. Journal of Micromechanics and Microengineering, Vol. 4, pp. 157-171.

12. **McCloy, D. and Martin, H. R.** 1980. Control of Fluid Power. 2nd Edition. s.l. : Ellis Horwood Limited, pp. 111-112.

13. **Claeyssen, F., et al.** 2010. New Actuators for Aircraft, Space and Military Applications. Bremen, Germany : s.n., Actuator 2010, 12th International Conference on New Actuators.

14. **Niezrecki, C., et al.** 2001. Piezoelectric Actuation : State of the Art. The Sock and Vibration Digest, Vol. 33, pp. 269-280.

15. **Park, S. E and Shrout, T. R.** 1997. Ultrahigh Strain and Piezoelectric Behaviour in Relaxor Based Ferroelectric Single Crystals. Journal of Applied Physics, Vol. 82, pp. 1804-1811.

16. **Prechtl, E. F. and Hall, S. R.** 1997. Design of a High Efficiency Discrete Servo Flap Actuator for Helicopter Rotor Control. Proceedings of the SPIE- The International Society for Optical Engineering. Vol. 3041, pp. 158-182.

17. **Yang, G., et al. 2001.** Temperature Dependance of Electrostrictive Properties of PMN-PT-LA ceramics. Ferroelectrics, Vol. 262, pp. 201-206.

18. **Straub, F. K. 1996.** A Feasibilty Study of Using Smart Materials for Rotor Control. Smart Material and Structures, Vol. 5, pp. 1-10.

19. **Bank, H. T., Smith, R. C. and Wang, Y.** 1996. Smart Material Structures - Modeling Estimation and Control. s.l. : John Wliey and Sons Ltd.

20. **Dickinson, C. A., Hughes, D. and Wen, J. T.** 1996. Hysteresis in Shape Memory Alloy Actuators: The control Issues. The Smart Structures and Materials 1996: Mathematics and Control in Smart Structures. pp. 494-506.

21. **Zhang, Q. M., Bharti, V. and Zhao, X.** 1998. Giant electrostriction and relaxor ferroelectric behaviour in electron-irradiated poly(vinylidene Flouridetrifluorethylene) copolymer. Science, Vol. 280, pp. 2101-2104.

22. **Bar-Cohen, Y. 2001.** Electroactive Polymers as Artificial Muscle-Reality and Challenges. Proceedings of the 42nd AIAA Structures, Structural dynamics and Materials Conference. pp. 16-19.

23. **Instrumente, Physik**. Piezoelectric in Positioning - Tutorial on Piezotechnology in Nanopositioning Applications. [Online] [Cited: 27 01 2010.] http://www.physikinstrumente.com/tutorial/4.

24. **Steinhaus, E. and Lipson, S. G.** 1979. Bimorph Piezoelectric Felxible Mirror. Journal of the Optical Society of America, Vol. 69, pp. 478-481.

25. **Bang, Y., et al.** 2003. Development of a Two Stage High Speed Electrohydraulic Servovalve Systems Using Stack Type Piezoelectric Actuators. Proceedings of the 2003 IEEE/ASME International Conference on Advanced Intelligent Mechatronics. pp. 131-136.

26. **Lindler, J. E. and Anderson, E. H.** 2002. Piezoelectric Direct Drive Servovalve. Industrial and Commercial Applications of Smart Structure Technologies. pp. 1-9.

27. **Hayes, E. and Corp, Siemens Automotive**. Piezoelectric Controlled Common Rail Injector with Hydraulic Amplification of Piezoelectric Stroke. U.S. Patent 5,779,149.

28. **Rueger, J. and GmbH, Robert Bosch**. Fuel Injection Systems. U.S. Patent 6,498,418.

29. **Lambert, M. and Delphi Technologies, Inc.** Fuel Injector. U.S. Patent 6,422,210.

30. **MacLachlan, B. J., et al.** 2004. Piezoelectic Valve Actuator for Flexible Diesel Operation. Industrial and Commercial Applications of Smart Structures Technologies, Vol. 5388, pp. 167-178.

31. **Reichert, M.** 2006. High Response Hydraulic Servovalve with Piezo-Actuators in the Pilot Stage. Olhydraulik and Pnuematik. pp. 1-17.

32. **Zhou, M., et al.** 2005. Fuzzy Control of a New Type of Piezoelectric Direct Drive Electro-Hydraulic Servo Valve. Proceeding of the Fourth International Conference on Machine Learning and Cybernetics. pp. 819-824.

33. **Brader, J. S. and Rocheleau, D. N.** 2004. Development of a Piezoelectrically-Controlled Hydraulic Actuator for a Camless Engine. Proc. Instn Mech. Engrs. Vol. 218 Part D. Automobile Engineering, pp. 817-822.

34. **Milecki, A.** 2006. Modelling and Investigation of Electrohydraulic Servovalve with Piezo Element. (Institute of Mechanical Technology, Poznan University of Technology), Vol. 26, pp. 181-188.

35. **Sedziak, D.** Investigation of Electrohydraulic Servo Valves with Piezo Bender as Control Element. 2010. 7th International Fluid Power Conference. pp. 1-12.

36. **Murrenhoff, H.** 2003. Trends in Valve Development. Oil hydraulics and Pneumatics. pp. 1-36.

37. **Yokota, S. and Akutu, K.** 1991. A Fast Acting Electro-Hydraulic Digital Transducer (A Poppet-Type On-Off Valve Using a Multilayered Piezoelectric Device. JSME International Journal, Vols. 34, No.4, pp. 489-495.

38. **Ouyang, X., et al.** 2008. Piezoelectric Actuators for Screw-in Cartridge Valves. Proceedings of the 2008 IEEE/ASME International Conference on Advanced Intelligent Mechatronics. pp. 49-55.

39. **Wong, A. P., et al.** 2006. Performance of the Piezo-Poppet Valve. Proc.IMechE J. Systems and Control Engineering, Vol. 220, pp. 439-451.

40. **Roberts, D. C., et al.** 2003. A Piezoelectriv Microvalve for Compact High-Frequency, High-Differential Pressure Hydraulic Micropumping Systems. Journal of Microelectromechanical Systems, Vols. 12, No.1, pp. 81-92.

41. **Lee, D. G., Or, S. W. and Gregory, C.** 2004. Design of a Piezoelectric-Hydraulic pump with Active Valves. Journal of Intelligent Material Systems and Structures, Vol. 15, pp. 107-115.

42. **Smits, J. G.** 1990. Piezoelectric Micropump with Three Valves Working Peristaltically. Sensor and Actuators, Vol. 21, pp. 203-206.

43. **Van Lintel, H. T.G., Van De Pol, F. C.M. and Bouwstra, S.** 1988. A Piezoelectric Micropump Based on Micromachining of Silicon. Sensors and Actuators, Vol. 15, pp. 153-167.

44. **Schiller, N. H., et al.** 2006. Development of a Piezoelectric-Actuated Fuel Modulation System for Active Combustion Control. Journal of Intelligent Material Systems and Structures, Vol. 17, pp. 403-410.

45. **Hermann, J., Gleis, S. and Vortmeyer, D.** 1996. Active Instability control (AIC) of Spray Combustors by Modulation of the Liquid Flow Rate. Combustion Science and Technology, Vol. 118, pp. 1-25.

46. **Lui, H., et al.** 2009. Vibration Active Control of Fluid Pulsation Based Piezoelectric Valve. World Congress on Computer Science and Information Engineering. Vol. 5, pp. 738-743.

47. **Hunt, T. M., Hunt, T. and Vaughan, N. D.** 1996. The Hydraulic Handbook. s.l. : Elsevier Science Ltd, ISBN 1856172503.

48. **Somashekhar, S. H., Singaperumal, M. and Kumar, R. K.** 2007. Mathematical Modelling and Simulation of a Jet Pipe Electrohydraulic Flow Control

Servo Valve. Proc. IMechE J. Systems and Control Engineering, Vol. 221, pp. 365-382.

49. **Wang, T., et al.** 2005. Modelling of a Nozzle-Flapper Type Pnuematic Servo Valve Including the Influence of Flow Force. International Journal of Fluid Power, Vol. 6 No. 3, pp. 33-34.

50. **Joshi, M. and Priya, S.** 2006. "Piezo-Bow" - High Displacement and High Blocking Force. Integrated Ferroelectronics, Vol. 82, pp. 25-43.

51. **McCloy, D. and Stevenson, I. J.** 1972. Some experiments with oil hydraulic vortex valves. Proc. Fifth Cranfield Fluidics Conference.

52. **Rivard, J. G. and Walberer, J. C.** 1965. A fluid state vortex hydraulic servovalve. Proceeding on the National Conference on Fluid Power. pp. 183-192.

53. **Iverson, B. D. and Garimella, S. V.** 2008. Recent advances in microscale pumping technologies: A review and evaluation. Microfluidics and Nanofluidics, Vol. 5, pp. 145-174.

54. **Ullman, D. G.** 2003. The mechanical design process. s.l. : McGraw Hill Third edition.

55. **Near, C. D. 1996**. Piezoelectric Actuator Technology. Proc. SPIE Symp. on Smart Structures and Materials.

56. **Straub, F. K., et al.** 1999. Development of a Piezoelectric Actuator for Trailing Edge Flap Control of Full Scale Rotor Blades. SPIE Symposium on Smart Material and Structures. pp. 25-34.

57. **Ballas, R. G.** 2007. Piezoelectric Multilayer Beam Bending Actuators. s.l. : Microtechnology and MEMS, Springer.

58. **Letty, R., et al.** 2003. Amplified piezoelectric actuators for aerospace applications. AMAS workshop on Smart Materials and Actuators, pp. 51-62.

59. **Noliac.** www.noliac.com/piezo_actuators-7764.aspx. [Online] Noliac.

60. **Ha, S. K. and Kim, Y. H.** 2001. Analysis of a Piezoelectric Multimorph in Extensional and Flexural Motions. Journal of Sound and Vibrations, Vol. 253, pp. 1001-1014.

61. **Instrumente, PhysiK**. PL 112. PL140 PICMA Bender Actuators. [Online] [Cited: 21 06 2011.] http://www.physikinstrumente.com/en/pdf/PL112_PL140_Datasheet.pdf.

62. **Cross, L. E.** 1995. Ferroelectric Materials for Electromechanical Transducer Applications. Jpn. J. Appl. Phys., Vol. 34, pp. 2525-2532.

63. **Biao, W.** 1992. Three-Dimensional Analysis of an Ellipsoidal Inclusion in a Piezoelectric Material. International Journal of Solids and Structures, Vol. 29, pp. 293-308.

64. **Praveenkumar, B., Kumar, H. H. and Kharat, D. K**. 2006. Study on Microstructure, Piezoelectric and Dielectric of 3-3 Porous PZT Composites. J. Mater Sci: Mater Electron, Vol. 17, pp. 515-518.

65. **Ling, H. C. and Jackson, A. M**. 1989. Correlation of silver migration with temperature-humidity-bias (THB) failures in multilayer ceramic capacitors. IEEE Transactions on Components, Hybrids, and Manufacturing Technology, Vol. 12, pp. 130-137.

66. **Pertsch, P., et al.** 2010. Development of highly reliable piezo multilayer actuators and lifetime tests under DC and AC operating conditions. PI ceramic.

67. **Systems, Piezo**. 1990. Piezoelectric Motor/Actuator Kit Manaul.

68. **Band, Y. B.** 2007. Light and Matter: Electromagnetism, optics, spectroscopy and lasers. s.l. : Wiley, ISBN-10: 0-471-89930-5 (HB).

69. **Moog**. Type 26 Single Inlet Flow Control Servovalves Catalogue. s.l. : Moog Inc. pp. 1-24.

70**. Gruning, T**. 2008. DJ Analysis Report. s.l. : Moog (Internal Report).

71. **Sherrit, S.** 2005. Smart Material/Actuator Needs in Extreme Environments in Space. Vol. 5761.

72. **Instrumente, Physik.** 2003. Piezoelectric ceramic products. s.l. : Physik Instrumente,

73. **Ge, P. and Jouaneh, M.** 1995. Modelling Hysteresis in Piezoceramic Actuators. Precis Eng, Vol. 17, pp. 211-221.

74. **Stepanenko, Y. and Su, C. Y.** 1998. Intelligent Control of Piezoelectric Actuators. Proc. IEEE Conf Deci Control. pp. 4234-4239.

75. **Ge, P. and Jouaneh, M.** 1997. Generalized Preisach Model for Hysteresis Nonlinearity of Piezoceramic Actuator. Precis Eng, Vol. 20, pp. 99-111.

76. **Sireteanu, T., Giuclea, M. and Mitu, M.** 2009. An Analytical Approach for Approximation of Experimental Hysteretic loops by Bouc-Wen Model. Proceedings of the Romanian Academy, Series A. Vol. 10, pp. 1-12.

77. **Lin, C. and Yang, S.** 2006. Precise positioning of Piezo-Actuated Stages Using Hysteresis-Observer Based Control. Mechatronics, Vol. 16, pp. 417-426.

78. **Whiting, I.** 2004. DJ Valve Dynamic Modelling Using Matlab/Simulink Based on Existing (SDP1265) Nozzle Flapper Valve Model. s.l. : Moog Controls Ltd (Internal Report), pp. 1-13. BR50038.

79. **Moog.** Electrohydraulic valves... A Technical Look. CDL6566 Rev D 500-170 302.

80. **Plummer, A. R.** 2008. A Detailed Model of a Six-Axis Shaking Table. Journal of Earthquake Engineering. Vol. 12, Issue 4, pp. 631-662

81. **The Centre for Power Transmission and Motion Control**. 2008. Introduction to Control for Hydraulic Systems. CPD course (FP-4).

Appendix A – Published Paper

Sangiah, D.K., Plummer, A.R., Bowen, C.R. and Guerrier, P. 2011. *A vortex valve for flow control in fluid systems*. Proceedings of the 12th Scandinavian Conference on Fluid Power (*SCFP'11*). Tampere Finland., Vol 1, pp. 241-253.

A vortex valve for flow control in fluid systems

Dhinesh K. Sangiah[1], Andrew R. Plummer[1], Christopher R. Bowen[1], Paul Guerrier[2]

[1]University of Bath, Bath, BA2 7AY, UK

[2]Moog Controls Ltd, Ashchurch, Tewkesbury, GL20 8NA, UK

Abstract

Power fluidics is the engineering of "all-fluid" systems in which fluid dynamic effects are used to control flow. The vortex amplifier is an example of such a device that has been applied to a number of fluid control problems over the past few decades. In the research described here, Computational Fluid Dynamics (CFD) was used to design and determine the performance of a vortex valve intended for fuel metering in aero engines. The final valve design was capable of delivering the maximum flow of 280l/min with a 6bar pressure drop.

The initial conventional design of the vortex valve was revised to remove the need for a control flow. The rotary vortex valve design uses a rotating chamber to generate the vortex instead of control flows. CFD results predict the valve can be successfully controlled in this way.

KEYWORDS: Vortex valve, Fuel metering, Computational Fluid Dynamics

Introduction

Power fluidics is the engineering of "all-fluid" systems in which fluid dynamic effects are used to control flow. With the absence of any moving parts the

effectiveness of fluidics depends on the fluid energy. A range of fluid dynamic phenomena can be used to utilise this energy; the vortex amplifier, the directed jet, the Coanda effect and flow diffusion being common examples. This paper is concerned with the vortex amplifier and its application in valve technology.

The vortex valve has been used as an alternative to the power stage spool in servovalves [1]. The use of a vortex amplifier in valve applications has the advantage of not being susceptible to fluid contamination and erosion. In addition the fabrication of the amplifier does not require close tolerances thus substantially reducing manufacturing cost.

This paper is concerned with using Computational Fluid Dynamics (CFD) to determine the performance of vortex valves. The vortex valve design discussed in the paper is intended for fuel metering in aero-engines. However the principle can also be applied for thrust vectoring, on-off control valves and for a servovalve pilot stage.

Background

Figure-1 shows the basic design of a vortex amplifier. For condition ‘a’, with no control flow, the supply flow enters the periphery of the vortex chamber and exits the chamber axially through the output with negligible pressure drop. For condition ‘b’, as the control flow gets introduced into the chamber the momentum of the control flow imparts a rotational flow component to the supply flow. The resulting flow spirals towards the centre of the chamber in a free vortex. The vortex flow field generates a radial pressure gradient in the chamber which increases the resistance to the supply flow. Thus the supply flow can be modulated by the control flow.

The basic vortex amplifier shown in Figure-1 has a limited flow modulation range. This is due to the considerable amount of control flow that is required to throttle the supply flow. In such a condition the control flow leaving the outlet contributes to valve leakage. To reduce the leakage, the control flow pressure can be raised. However, the control flow pressure needs to be significantly higher than the supply pressure to achieve a reasonable flow gain (the ratio of supply flow to control flow).

Even with raised control flow pressure there will always be a leakage flow associated with the basic vortex amplifier design.

Rivard, et al., [1] developed a vortex valve with a flow pick off downstream to the vortex chamber outlet. This is shown in Figure-2.

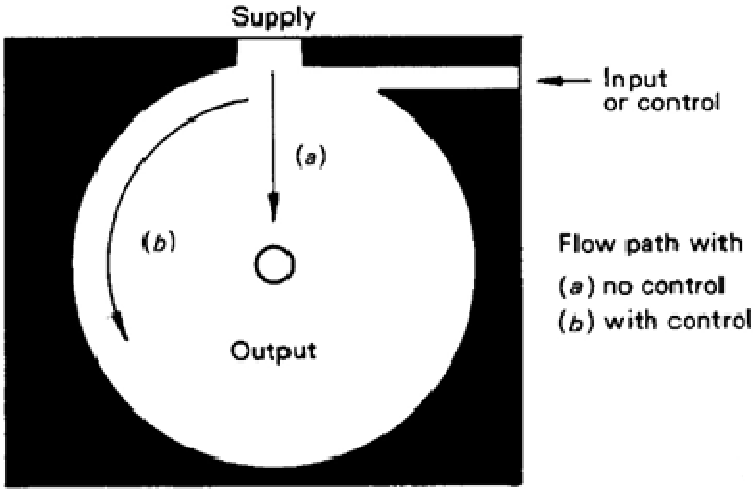

Figure-1: Basic vortex amplifier design [2]

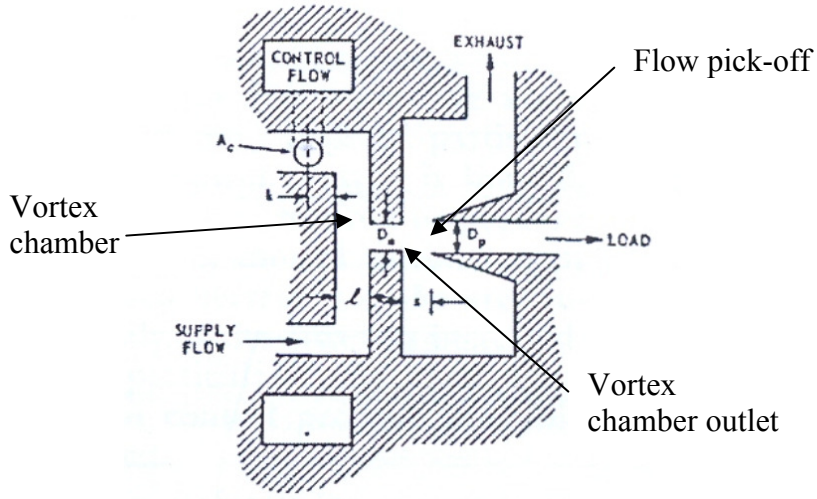

Figure-2: Vortex valve with flow pick-off [1]

The flow pick-off shown in Figure-2 is a tubular receiver located at a set distance concentrically to the vortex chamber outlet. With the no control flow, the flow exiting the vortex chamber is a well defined jet. This flow is recovered at the flow pick-off. When a control flow is introduced, the resulting vortex flow field assumes a hollow conical shape at the outlet due to its tangential flow momentum. This cone of fluid impinges on the flow pick-off and some is diverted to the exhaust. Increasing the control flow will result in all of the exiting flow missing the flow pick-off. This produces a valving action with complete flow modulation.

The vortex valve developed by Rivard, et al., [1] is a four-way operated two stage valve. The pilot stage uses a flapper nozzle arrangement to modulate the control flow. The second stage comprises a pair of vortex amplifiers. The flow recovered at the flow pick-offs, downstream to the vortex chamber outlet, drives an actuator. With no control flow, the flow recovery characteristic at the flow pick-off was claimed to be similar to a conventional jet pipe valve.

Rivard, et al., [1] claimed that the pressure-flow characteristics of the vortex valve was similar to a four-way spool valve with a 10 to 1 flow modulation range with a quiescent leakage of 20% of the supply. The dynamic response of the valve was reported to be similar to a spool valve.

Mayer, et al., [3] derived analytical techniques to predict the performance of vortex valves. These techniques were evaluated experimentally. The results show reasonable agreement for flow gains. The flow relationship trend and the cut-off control pressure show better agreement. Cut-off control pressure is the control flow pressure at which all of the supply flow is throttled.

Brodersen, et al., [4] presented a design of a fluidic hot gas system and discussed the feasibility of demonstrating vortex valves for thrust/jet interaction control of a missile. As part of a conceptual study subscale vortex valves were developed and tested with high pressure cold gases as supply and control fluids. The valve configuration was optimised for response time, weight and maximum flow gains. The final valve design had two supply ports and one control port with a chamber to

nozzle radius of 3:1. A maximum flow gain of four was reported for the valve at 0.45 kg/s and 17.5MN/m^2 supply flow and pressures, respectively.

The work done by Brodersen, et al., [4] was extended to full scale vortex valve designs. For identical test conditions the flow gains of the scaled valves were reported to be similar to the subscale models. For hot supply gases, a maximum flow gain of nine was reported for the scaled valves when using cold gas or liquid control flows.

This paper aims to develop a vortex valve for fuel metering in aero-engines by using CFD simulation technique. CFD will be used to determine and optimise the performance of the valve. The valve design will be optimised to achieve maximum flow gains with minimum increase in control pressure ratio. The control pressure ratio is the ratio of control flow pressure to supply flow pressure.

CFD modelling and validation

Based on the available published literature, there has been no attempt to date to use CFD modelling to determine the performance of vortex valves. Therefore it was considered a prerequisite to establish the accuracy of the CFD technique by reproducing a known set of published test results. A set of experimental data for a gas valve published by Brodersen, et al., [4] was used to develop the CFD model shown in Figure-3.

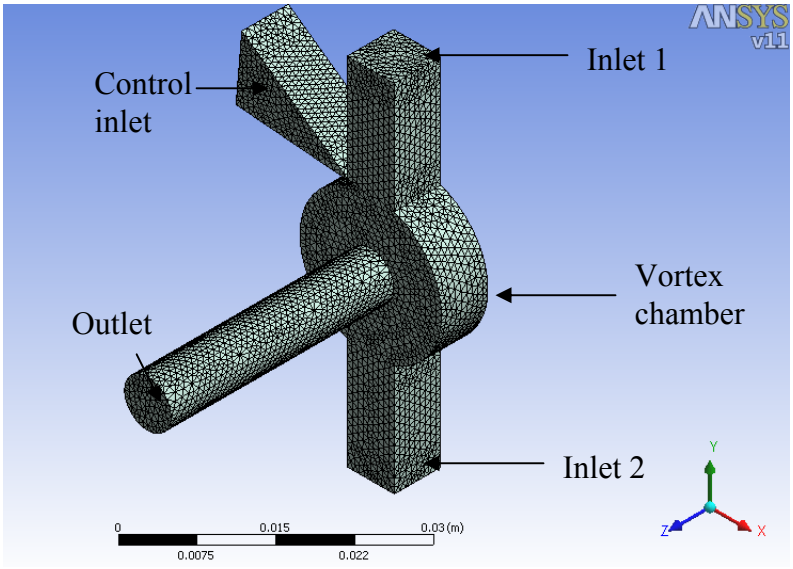

Figure-3: Validation model

The port configuration of the vortex valve can be observed in Figure-3. The ports were made longer to ensure the vortex dynamics do not influence the boundary conditions and the pressure and flow measurements. The tapered control port profile was approximated from the published data [4] as this was not stated explicitly. Considerable differences in valve flow gains were realised between tapered and parallel control port configuration.

Simulations were performed at identical operating conditions to the experiments [4]. Information on gas temperature was unavailable, therefore the temperature of the high pressure gaseous Nitrogen was set at room temperature. This assumption is expected to influence the results as the density of the gas will be higher at lower temperatures.

From initial simulations it was realised that the complexity of the flow at the vortex was too high for the solutions to converge. Thus the advection scheme of the solver was relaxed to make the solution more robust. However, this process influences the accuracy of the results. Figure-4 shows the comparison of supply flow as a function of control flow between simulated and experimental data.

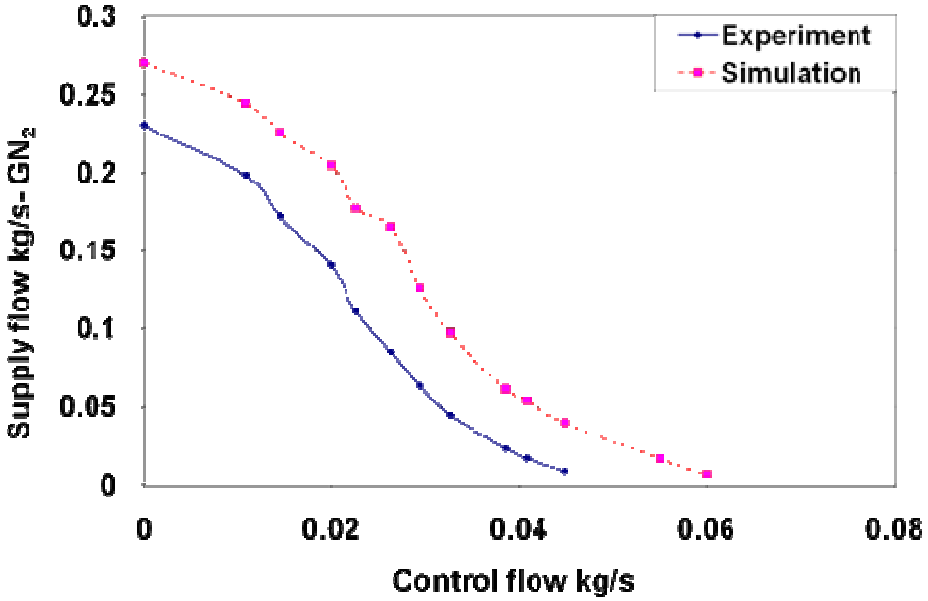

Figure-4: Comparison of experimental and simulated data

As expected, discrepancies between the experimental and simulation results can be observed in Figure-4. Nevertheless the experiment trend is well reproduced by the CFD simulation. Reducing the temperature of the operating gas is expected to move the simulation results closer to the experimental data. The results are acceptable despite the inaccuracies in the discretisation technique and the geometry as the flow relationship trend is reproduced closely. Based on the validation of the CFD approach, the next section will design a vortex valve for aerospace application.

Vortex Valve Design

The initial valve design was intended to modulate fuel flow in aero-engines. The valve has to be compact and lightweight and be able to handle fuel flows up to 280l/min with minimum pressure drop across the valve. It is also important to keep the control port pressure close to the supply pressure, otherwise a boost pump will be required to generate the additional control flow pressure.

Previous work undertaken on vortex devices [5], [6], [7], [8], [9] has derived a choice of parameters to optimise the performance of vortex amplifiers. For

incompressible flow, the transfer characteristic of vortex amplifiers can be described by four geometrical ratios if the effects of surface tension and heat transfer are neglected [5]. These four geometrical ratios are:

Exit to chamber outlet ratio: $\frac{r_e}{r_o}$

Chamber aspect ratio: $\frac{h}{r_o}$

Supply to exit area ratio: $\frac{A_s}{A_e}$

Control port to exit port ratio: $\frac{A_c}{A_e}$

In the absence of a control flow, the valve delivers its nominal maximum flow which is determined by the supply and exit port characteristics [3]. Considering that the supply port is relatively large compared to the exit port, almost all of the flow restriction at the condition of no control flow will be at the outlet. Therefore the outlet can be designed as an orifice restriction at maximum supply flow [3].

$$Q_e = A_e C_{de} \sqrt{\frac{2}{\rho}(P_s - P_b)}$$

171

The exit to chamber outlet ratio ratio r_e/r_o influences the shape of the vortex amplifier characteristic and determines if the response is proportional or bistable [6], [9]. Lawley et al., [6] found that the response is proportional for r_e/r_o=0.089 and bistable for r_e/r_o>0.12. The response becomes bistable at higher ratios due to the decrease in viscous dissipation [10]. King [11] suggests the optimum ratio for r_e/r_o is dependent on the control port to exit ratio A_c/A_e. In order to keep the design compact a value of 1/3 was chosen for r_e/r_o based on available information.

Brodersen et al., [4] predict that the frequency response of vortex amplifiers increase with decreasing chamber height. The response time of a vortex amplifier is approximately the time taken to replace the flow field in the vortex chamber. Therefore small aspect ratios will have better response time. The performance gain with decreasing aspect ratio is limited by the 'curtain area'. This is the minimum cylindrical surface area through which flow passes radially before making its turn to the exit in the vortex chamber. At low aspect ratios (>0.2) the curtain area begins to dominate flow restrictions. At these chamber aspect ratios the flow instabilities and noise become significant [11], [12]. King [11] suggests an optimum value of approximately 0.3.

Syred [12] and Wormley et al., [5] indicate that the supply area 'A_s' has a negligible effect on device performance for $A_s/A_e>3$. If the A_s/A_e ratio is lower, the required control flow and pressure will increase for a given supply flow, leading to a decrease in the overall performance of the device. At ratios $A_s/A_e>4$ a deterioration in performance was reported by Syred [12]. This was due to the degree to which the vortex chamber walls were cut away. Thus an optimum supply to exit ratio is $3<A_s/A_e<4$.

The control port area also influences the flow gain of the valve. A smaller control port area improves the flow gain, however this also leads to an increase in control flow pressures. It has been found [10] that the performance of the valve becomes insensitive to control port area for ratios $A_c/A_e<0.1$ due to mixing losses in the port. Therefore the sizing of the control port area is a trade off between performance and control port pressures.

The influence of control port configurations on valve performance have not been considered in the past. The entrance angle of the control jet in the vortex chamber influences the point of attachment of the flow to the chamber wall. This in turn influences the restriction of the flow from the supply ports and thus the flow gain. Various tapers and control port angles will be simulated in this work to obtain the optimum performance for the valve.

A flow pick-off is required downstream of the vortex chamber outlet to generate a valving action. There are no published geometrical relationships for flow pick-offs, therefore optimum geometries were obtained iteratively from simulations.

Various different port configurations were generated and their results were compared to optimise the design. Figure-5 shows the optimum control volume for a vortex valve designed for maximum flow of 280l/min of fuel.

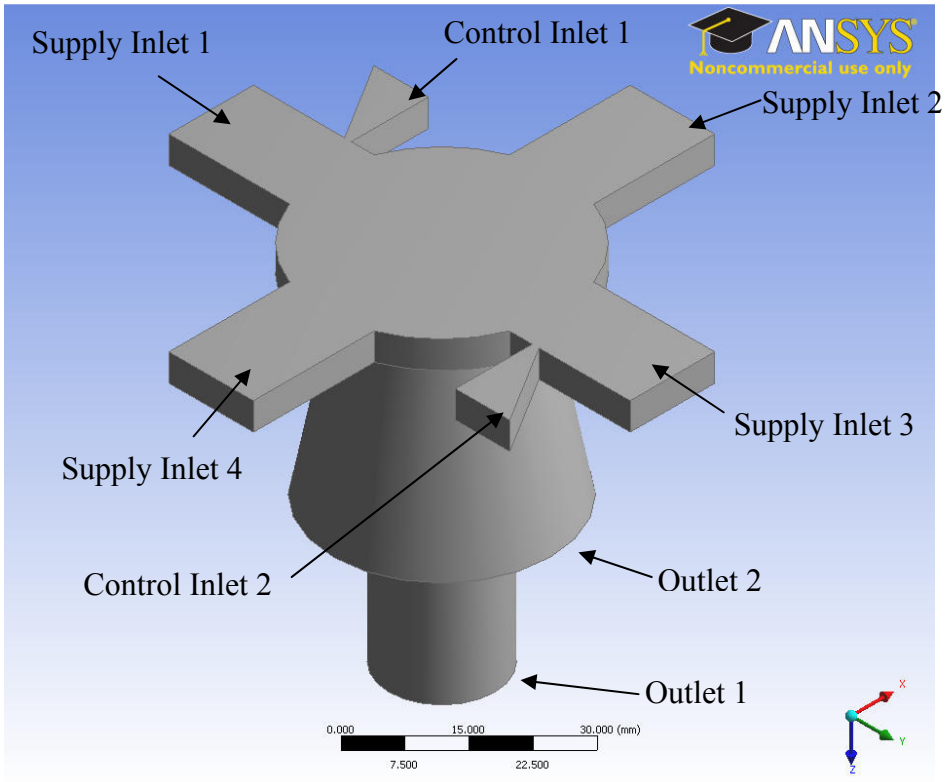

Figure-5: Vortex valve model

The objective was to design a compact high performance valve. The optimum valve, shown in Figure-5, comprises four supply ports and two control ports. Four supply ports were required to maintain the optimum supply to exit ratio given the small aspect ratio of the valve. The supply port configuration will limit the degree of material cut-away and provide a uniform flow distribution in the chamber. Higher

flow gains were obtained with the configuration shown in Figure-5 compared to having two supply ports and one control port.

The positioning of the control ports and its taper was controlled to provide the best performance gain with limited rise in control port pressures. The entrance of the control port flow influences the vortex formation in the chamber and thus the flow gain. Improved performance was realised by placing the control port in the supply port and aligning the control jet as a tangent to the opposite lip of the supply port.

The flow pick-off, shown in Figure-5 was placed as close as possible to the vortex chamber outlet. The flow recovered by the pick-off is transmitted to the engine and the flow through outlet 2 is transmitted back to tank. Thus the valve is designed to transmit maximum flow when no control flow is present.

King [11] investigated the influence of a diffuser at the vortex chamber outlet. The diffuser controls the flow separation at the chamber wall when the supply flow changes direction to exit the chamber. The investigation concluded that the diffuser increases maximum supply flow. The optimum diffuser geometry suggested by King [11] was used in the valve design.

Vortex valve simulation results

The operating conditions for the valve for the fuel metering application are 280l/min maximum supply flow at 140bar supply pressure. The pressure drop across the valve at maximum flow is specified as 6bar. These pressure values were set as boundary conditions at the inlet and outlet, respectively. Figure-6 shows the maximum flow operating condition with no control flow. The figure shows that all of the supply flow is recovered at the flow pick-off. In this condition, maximum flow is supplied to the engine. As a control flow is introduced the flow through outlet1 decreases. Consequently the flow through outlet 2 increases. Therefore at maximum control flow, all of the supply flow will be transmitted into outlet 2. This can be observed in Figure-7.

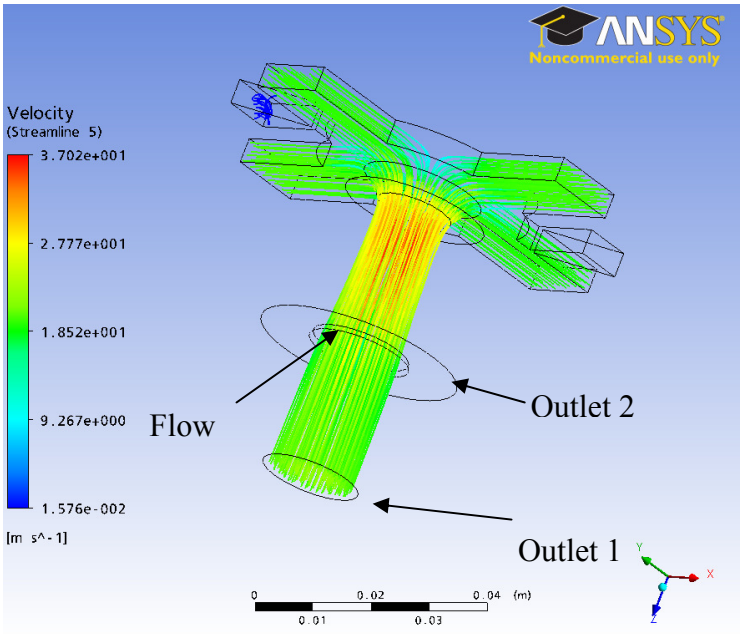

Figure-6: Vortex valve with no control flow

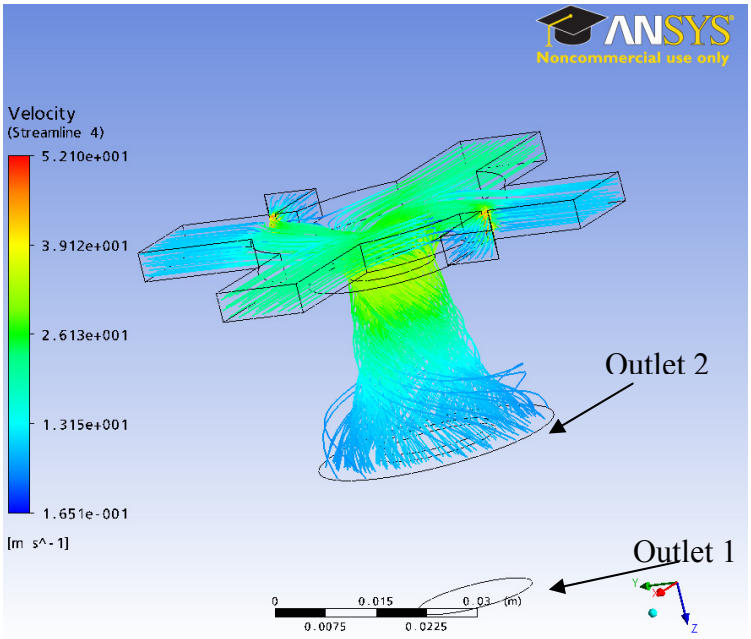

Figure-7: Vortex valve with maximum control flow

The simulation results show that the maximum flow through the valve is approximately 300l/min of fuel at 140bar supply pressure and 134bar back pressure. The maximum control port flow required to shut the flow to the engine was approximately 33l/min. Therefore the valve demonstrates a flow gain of nine. The

control port pressure required to produce the maximum control flow is 151bar and the maximum control pressure is 7% higher than the supply pressure. Compared to previous vortex valve designs [4], [3], [12] the flow gain achieved for the valve is significantly higher in relation to the control port pressure ratio. It is common to achieve high flow gains with control port pressures typically over twice the supply pressure. Hence the results suggest that the valve performance would be considerably better than other values reported in the literature.

Although the performance of the valve is superior to previous valve designs the maximum control port flow was considered too high for the fuel metering application. The control flow can be considerably decreased by increasing the control pressure. However this is not a feasible solution due to the requirement of a boost pump to generate pressures higher than the supply. Hence an alternative design which mitigates these problems was investigated.

Rotary vortex valve (RVV)

The rotary vortex valve (RVV) uses a rotating vortex chamber to generate the vortex instead of control ports. The flow control is achieved by changing chamber angle. The flow gain for this concept will be determined by the angle of rotation required to modulate the flow to the engine from maximum to no flow. A schematic of the top view of the RVV is shown in Figure-8. The supply port connections are flexible to allow rotation of the chamber. Figure-9 shows the valve with minimum rotation and maximum flow to the engine. As the vortex chamber is rotated the flow swirl is increased. In this condition not all the flow is recovered to the engine, some of the flow is diverted towards the return. Hence at a maximum rotational angle no flow will be picked off and all of the flow will be diverted to the return. This can be observed in Figure-10.

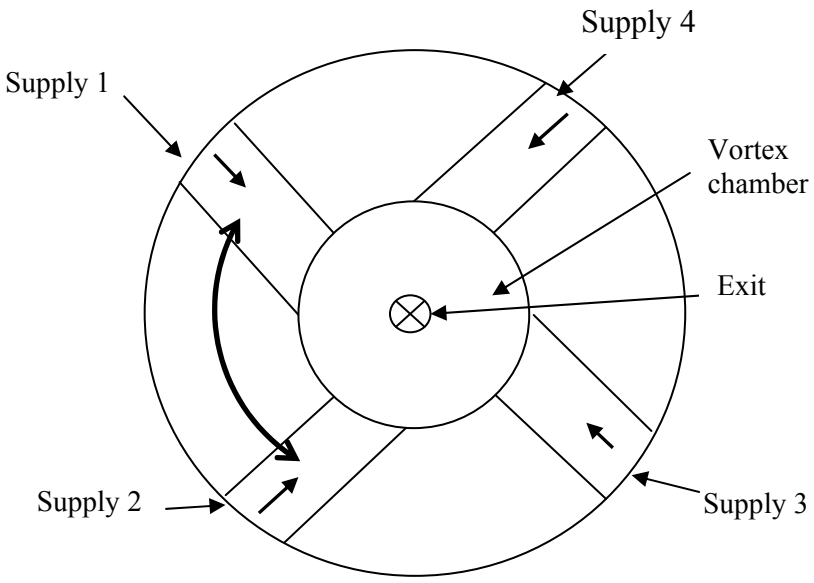

Figure-8: Schematic of the top view of RVV

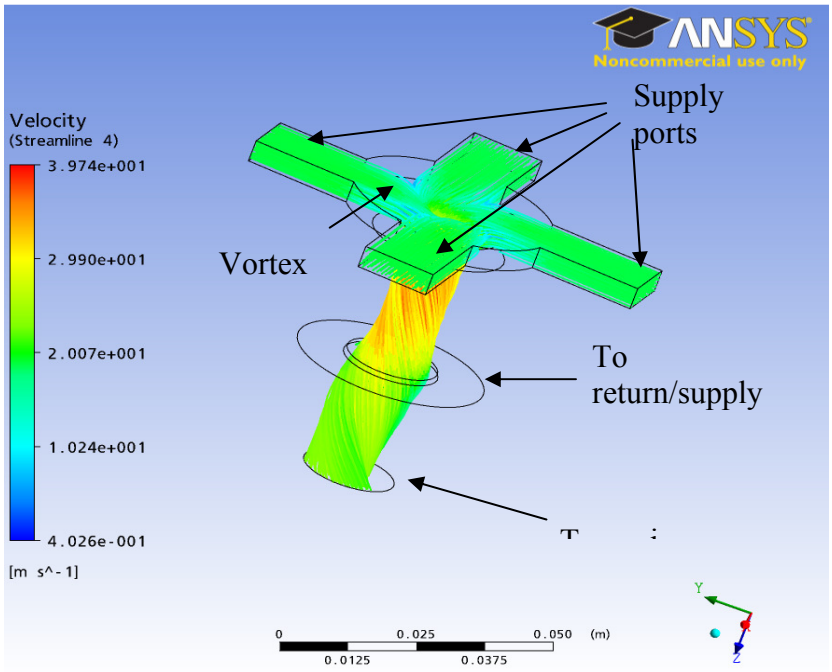

Figure-9: Maximum flow to the engine with minimum chamber angle

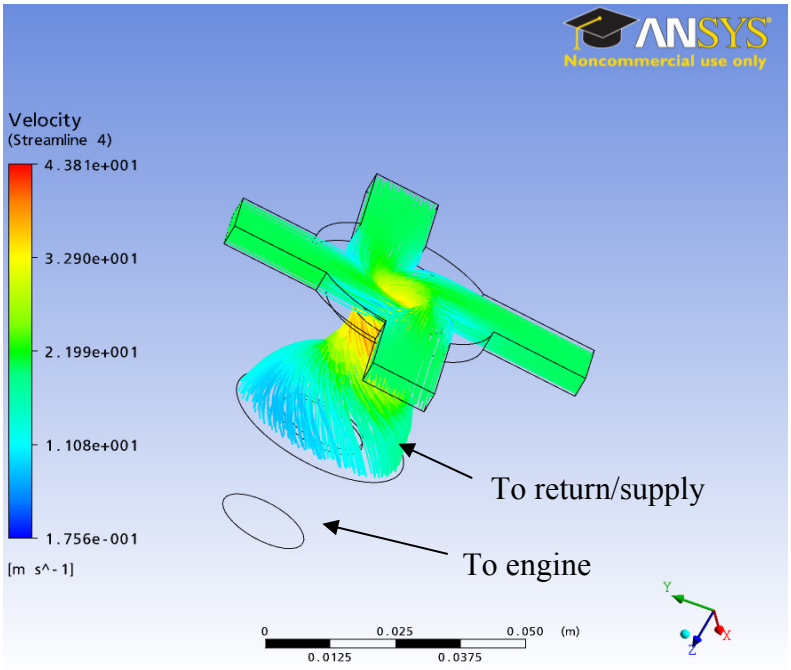

Figure-10: No flow to the engine with maximum chamber angle

RVV simulation results

Simulations were performed at identical operating conditions as the previous design. Flow gains were investigated at different pressure drops across the valve. The results are shown in Figure-11. From Figure-11 it can be observed that the response of the valve is different to that of a conventional vortex valve, shown in Figure-4. The response is nonlinear. At low control angles the flow is not very sensitive to angle. At higher angles the flow is much more sensitive to the control angle.

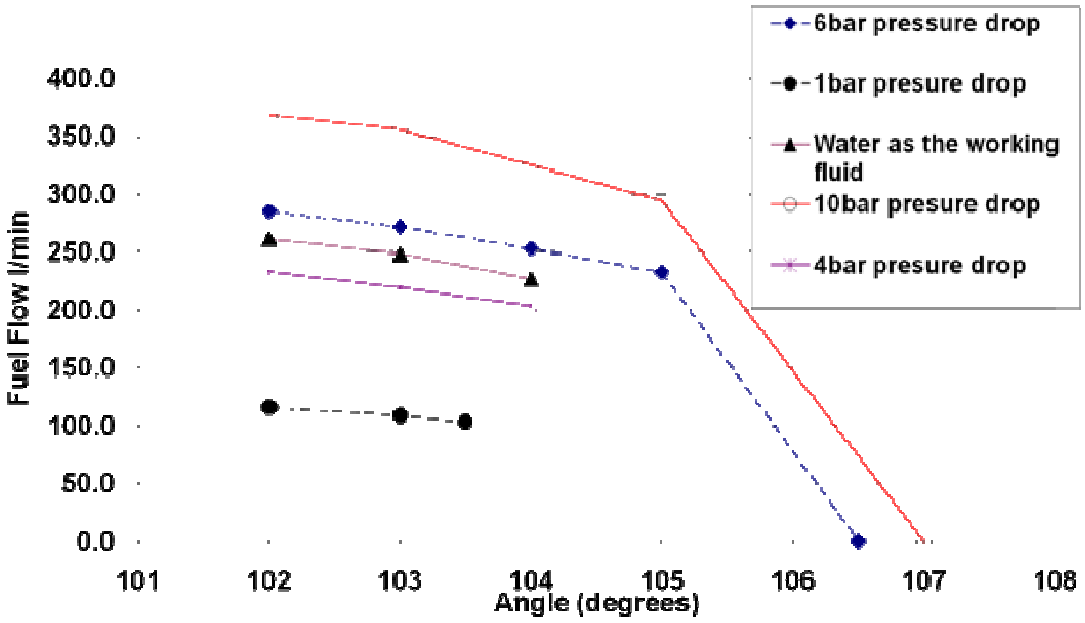

Figure-11: Simulation results

The maximum flow is dependent on the pressure drop across the valve. The trend in response at different pressure drops can be observed to be consistent from Figure-11.

The performance of the valve for different fluids can also be observed in Figure-11. Water was used as the working fluid at the 6bar pressure drop operating condition. The flow through the valve can be observed to be lower than that of fuel at the same pressure drop. This is expected as the density of water is higher.

The performance of the valve was investigated for different pressures between the two outlets. It was found that for pressure differences greater than 1bar the valve ceases to function correctly. At these conditions the flow is transmitted to the lower pressure outlet irrespective of the demand.

The sensitive nature of the valve to pressure difference between the outlet ports potentially makes the valve impractical for the fuel metering application. The valve is only useful for applications in which there is a small difference between the outlet port pressures. One such application could be the first stage of a two stage spool

valve. Thrust vectoring or on-off control valves are other potential applications to which the novel RVV valve design could be successfully applied.

Conclusions

CFD modelling of vortex amplifiers is a viable technique to design optimum geometries to enhance performance. The technique was validated using published experimental data. The trend in the simulated flow agrees well with the experimental data.

The vortex valve was designed for optimum performance using published information. In addition CFD was used to determine optimum geometrical configurations. The optimum control port configuration was iteratively obtained for maximum flow gains with minimum increase in control pressure.

The designed valve was capable of delivering the maximum flow of 280l/min of fuel with a 6bar pressure drop at maximum flow. The flow gain of the valve was found to be approximately nine. This flow gain corresponds to a negligible pressure increase in the control port. The flow gain achieved for the valve, for the same control pressure ratio, is very high compared to published literature.

The rotary vortex valve (RVV) was also examined which is a novel concept developed to avoid the need for control flows required in conventional vortex valve designs. The valve uses a rotating vortex chamber to generate the vortex. A Flow gain of approximately 70 Kg/s/^{o} was obtained for the valve. However the characteristic is non-linear. At higher control angles the flow is very sensitive to the angle.

The vortex valve and the rotary vortex valve designs were sensitive to pressure drop between the outlet ports. This characteristic makes the design impractical for the fuel metering application.

References

[1] Rivard, Jerome G. and Walberer, John C. 1965. A fluid state vortex hydraulic valve. Proceedings of the National Fluid Power Conference. pp.183-192.

[2] McCloy, D. and Martin, H.R. 1980. Control of fluid power: Analysis and design. Ellis Horwood series in Mechanical Engineering.

[3] Mayer, Endre A. and Maker, Paul. 1964 Control characteristics of vortex valves. Proceedings of the Fluid Amplification. pp.61-83

[4] Brodersen, Rolf K. and Papadopoulos, James G. 1981. Hot gas control system design and vortex valve tests. IEEE Transactions on Automatic Control. Vol. AC-26.NO. 3.pp. 625-637

[5] Wormley, D.N. and Richardson, H.H. 1970. A design basis for vortex-type amplifiers operating in the incompressible flow regime. Trans. ASME, Journal of Basic Engineering. Vol. 92.

[6] Lawley, T.J. and Price, D.S. 1972. Design of vortex fluid amplifier with asymmetric flow fields. Trans. ASME Journal of Dynamic Systems, Measurements and Control. Vol. 94.

[7] McCloy, D. and Stevenson, I.J. 1972. Some experiments with oil hydraulic vortex valve. Proceedings of the Fifth Cranfield Fluidics Conference.

[8] Skoog, A.I. 1972. Oil hydraulic fluidic amplifiers. Proceedings of the Fifth Cranfield Fluidics Conference.

[9] Biachara, R.T and Orner, P.A. 1969. Analysis and modelling of the vortex amplifier. Trans. ASME, Journal of Basic Engineering.Vol. 91

[10] Wormley, D.N. 1974. A review of vortex diode and triode static and dynamic design techniques. Proceedings of the Fluid State-of-the-Art Symposium. pp. 1-43

[11] King, C.F. 1985. Vortex amplifier internal geometry and its effect on performance. International Journal of Heat and Fluid Flow. Vol. 6. pp. 160-170

[12] Syred, N. 1969. An investigation of high performance vortex valves and amplifiers. Dept. of Mech. Eng. University of Sheffield.

[13] Vaughan, N.D., Johnston, D.N., and Edge, K.A. 1992. Numerical simulation of fluid flow in poppet valves. Proceedings of the Institution of Mechanical Engineers. pp. 119-127